Towards Miniaturized Strontium Optical Lattice Clock

by

Wei He

A thesis submitted to
The University of Birmingham
for the degree of
DOCTOR OF PHILOSOPHY

Ultracold Atoms Group
School of Physics and Astronomy
College of Engineering and Physical Sciences
The University of Birmingham

September 2016

UNIVERSITY OF BIRMINGHAM

Abstract

College of Engineering and Physical Sciences
School of Physics and Astronomy

Doctor of Philosophy

by Wei He

Optical atomic clocks with precisions and accuracies in the 10^{-18} level are now the most advanced man-made timekeeping devices. They outperform the microwave cesium atomic clocks that realize the SI definition of the second. Scaling down the size of optical atomic clocks may open the door to a range of industrial and space applications.

In this thesis, the design and preliminary results of a compact strontium cooling system are presented. In the first cooling stage, the high power 461 nm laser with 300 mW output features a modular design, while smaller laser sources for demonstrating a strontium magneto-optical trap have also been investigated. An innovative design that couples a spectroscopy cell directly into the scientific chamber reduces the overall size and power consumption of the system. Additionally, using strontium oxide as a source of strontium atoms suitable for optical clocks has achieved initial success. For the first time, a single-beam MOT configuration is applied to strontium. In this novel apparatus, the blue MOT and red MOT broadband cooling phases are able to trap 5×10^6 and 1000 atoms, respectively. This work shows promising progress towards developing a functional miniaturized strontium optical lattice clock.

Acknowledgements

Contents

List of Figures

List of Tables

Introduction

The strontium optical lattice clock was first proposed and demonstrated by Professor Hidetoshi Katori in 2003 [1]. After 12 years development, this "magic wavelength" optical lattice atomic clock had already beaten the record of the cesium clocks [2,3], reaching a fractional uncertainty of 10^{-18} [4]. With two orders of magnitude improvement, the strontium optical clock is one of the promising candidates for the International System of Unites(SI) second re-definition [5]. These laboratory based strontium clocks could serve as the national or international frequency standards [6]. They are also helpful for other precision measurement experiment [7]. However, for application such as communication network synchronization [8], absolute gravitational potential measurements [9], high precision clock comparisons, gravitational wave detection [10], the clock community needs to improve the transportability of the optical clocks. In the cold atoms group at the University of Birmingham, two generations of transportable strontium clocks had been developed, one of which had measured the clock transition with a linewidth of 9 Hz [11]. To further reduce the dimensions of the system, the clock team in Birmingham started the miniaturized strontium clock project whose long term objective is to build a strontium lattice clock with 10^{-16} accuracy and precision, meanwhile limiting the system volume to 30 liters.

I had involved in all the three clock projects. For the first generation transportable strontium lattice, I had tested different 461 nm lasers for the experiment. The idea

using strontium oxide(SrO) as a strontium source started from this project. I had joined in all the SrO experiment and verified that the SrO could be easily controlled to generate strontium atoms. This work resulted in one patent "Kock, O., Singh, Y., Bongs, K., & He, W. (2016). CONTROLLED ATOM SOURCE. WO 2015145136 A3." and a paper "Kock, O., Wei, H., Świerad, D., Smith, L., Hughes, J., Kai, B., & Yeshpal, S.. (2016). Laser controlled atom source for optical clocks. Sci. Rep., 6, 37321." For the second generation, a working strontium optical lattice clock which is now in Germany, I had taken part in constructing and testing the vacuum system. I had also built the laser distribution module for the system. There were two papers published on this project: "Kai B., Singh Y., Smith L., et al. Development of a strontium optical lattice clock for the SOC mission on the ISS. Comptes Rendus Physique, 2015, 16(5):990003." and a conference paper with the same name. For the miniaturized strontium optical lattice project, I had designed and built the vacuum system and the 461 nm diode laser. The preliminary results were quite promising. This thesis is a summary of my work during the last four years, focusing on the design and preliminary results of the miniaturized strontium clock project.

To reduce the power consumption and the size of the vacuum apparatus, I replaced the 200 liters vacuum chamber and the water cooled anti-Helmholtz coils with a 2 liters vacuum chamber and a pair of air cooled coils, respectively. To increase the robustness of the laser system, homemade lockable optics mounts took the place of the conventional optomechanics. After those changes, I measured the trapped atom number in the first stage cooling [12] to be 5×10^6 which is half of the number from the operating strontium clock that had been built in our lab [13]. The result showed that the new hardware design applied on the experiment setup are highly promising for the clock operation. An external cavity diode laser(ECDL) [14] based on newly developed 30 mW 461 nm diode were tested to substitute the energy-

intensive frequency doubling blue laser. Although the limited laser power could not fulfill the requirement of the experiment, the laser design could be applied to the system once a higher power diode were developed. A new approach using strontium oxide as a strontium source has been demonstrated and characterized. By focusing a 405 nm low power laser on to a strontium oxide sample, the strontium atom would be released for the experiment. As an alternative to a high temperature strontium oven, laser desorbed strontium oxide can improve one source of the clock transition frequency shift due to blackbody radiation (BBR) [15], as well as reduce the energy requirements of a portable system. As an ongoing project, many opportunities remain for future improvements. The main scientific results in this thesis are the first strontium magneto-optical trap (MOT) [16, 17] from strontium oxide and achieving the second stage cooling in the miniaturized vacuum system.

There are seven chapters in the thesis and they are organized as follows: Chapter 1 gives an overview of the clock development. Chapter 2 summarizes the theory and technology related to strontium optical lattice clocks. Chapter 3 presents the efforts to minimize the laser system of the strontium clock. Chapter 4 gives details of the single beam mirror MOT design and construction, comparing the difference of the traditional six beam MOT and the compact single beam mirror MOT. Chapter 5 exhibits the primary results of the miniaturized strontium clock experiment, from the blue mirror MOT to the red mirror MOT. Chapter 6 introduces the first steps towards the new strontium oxide source for the strontium clocks, from sample preparation to velocity distribution measurements. Chapter 7 looks into the future of strontium optical clock projects in University of Birmingham.

Chapter 1

From Sundial to Optical Atomic Clocks

From sowing seeds to growing artificial crystals, mankind's increasingly sophisticated activities need to be synchronized to more precise and accurate timekeepers. From wristwatches to satellite based clocks, miniaturized and user friendly timepieces enable a wide variety of applications.

In this chapter, the history of timekeeping will be introduced.

1.1 The history of clocks before the quantum era

When we look into history, society has evolved alongside the development of time-keeping devices. The rotation and revolution of the Earth are natural clocks for all who live on it. For thousands of years, activities synchronized to years, months and days were sufficient for early societies. However, smaller time intervals for more complicated tasks were not directly accessible until man-made timing instruments were invented.

The sundial is the earliest piece of man-made time-measuring equipment. The daytime is divided into smaller divisions. As civilization progressed, our forebears subconsciously used gravity for time-keeping. Sand and water flowing from a higher potential to a lower one was used to measure one time interval. These simple clocks

4

dominated timing tools for hundreds of years. As for the disadvantages of these elementary timepieces, the craftsmanship would affect the accuracy immensely. Around 1602, Galileo Galilei found that the length of period is only dependent on the pendulum length. The harmonic oscillation of pendulums enormously increased the accuracy of the well adjusted clock to 15 seconds per day in the 1660s [18]. By the end of the 1920s, pendulum clocks reached accuracies of 1 ms per day [19]. With the assistance of mechanical clocks, human activity could be easily organized in one factory, one town or even one small country.

The next boost to clock accuracy came from quartz clocks. Quartz was found to be a piezoelectric material and would resonate when formed into plates. An electronic oscillator circuit with a high-frequency quartz resonator can be used as a frequency standard. Tuning, amplifying and converting the oscillation signal allows it to serve as an precise clock. Another advantage of quartz is the low temperature sensitivity which guarantees a more precise frequency source compared to the pendulum. Before the atomic clock, it was quartz clocks that provided the time standard for the United States between the 1930s and 1960s. After the invention of cheap and small-sized semiconductor digital logic in the 1960s, quartz clocks saw broader application. Since then, quartz frequency standards are used in almost every piece of electronics. In the 21st century, well designed and manufactured quartz clocks can lose or gain just 1 second in more than 100 years of free running time [20].

1.2 Timekeepers competition before the laser

Using quantum theory to describe the structure of atomic energy levels, an atom's energy can change due to the absorption or emission of discreet amounts of electromagnetic radiation, where the change in energy is determined by the frequency of

the radiation. The quantum mechanical model of atoms paves the way for making clocks using atomic energy transitions.

For atoms of the same species in the absence of external perturbations, the radiation from a specific energy transition has the same frequency. This phenomenon theoretically enables the absolute measurement of time. Frequency differences between clocks based on the same atomic species will only depend on environmental effects and the frequency measurement device.

In 1949 an ammonia maser [21] using an atomic transition as the frequency reference was made at the U.S. National Bureau of Standards (now the National Institute of Standards and Technology, NIST). Then Louis Essen and Jack Parry in the U.K. National Physical Laboratory (NPL) made the first cesium atomic clock [22] in 1955. The first cesium clock used a microwave cavity to probe a cesium beam and a detector to measure the energy level transitions. Its accuracy reached one second in about 300 years, which beaten the existing quartz clocks. After the development of cesium clocks in the early 1960s, their unprecedented accuracy led to the definition of the S.I. (International System of Units) second of atomic time as: "the duration of 9192,631,770 periods of the radiation corresponding to the transition between the two hyperfine levels of the ground state of the cesium-133 atom." [23] The definition holds to the present day, and Cs clocks are still widely used in laboratories and industry.

As seen in Figure 1.1, there are two hyperfine states $F = 3$, $m_F = 0$ and $F = 4$, $m_F = 0$ in the Cs ground state $6^2 S_{1/2}$, resulting from the magnetic interaction between the nucleus and electron. F is the total angular momentum, m_F is the magnetic quantum number and $6^2 S_{1/2}$ is the term for the ground state Cs atoms. The frequency of the transition between these two states is in the 10^{10} Hz level while the linewidth is in the Hz level. Setting a microwave's frequency to the energy

difference of the two hyperfine states, atoms passing the field may be excited. As a result, the population distribution in the two hyperfine states is changed. By changing the microwave frequency and detecting the resulting radiation intensity, the frequency with the maximum excitation fraction can be determined and locked. Then, the externally generated microwave field is identical to the cesium transition frequency and can be used as a frequency standard. According to the definition, the frequency is 9.19263177 GHz.
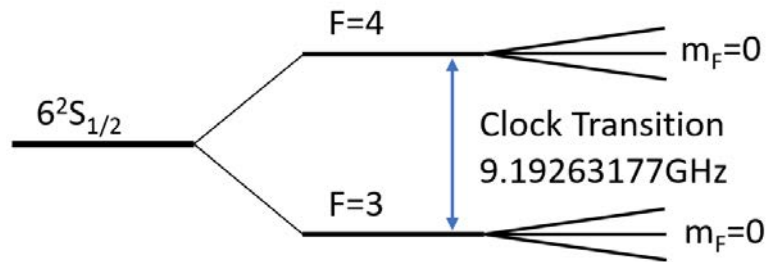
Figure 1.1: The interaction of the electron's spin with its angular momentum(spin-orbit interaction) results in the fine structure of the cesium ground state. The hyperfine structure results from the magnetic interaction between the nucleus and electron. With a constant magnetic field, the hyperfine levels are split into sub-levels. The clock transition is the $6^2S_{1/2}$ $F = 3$, $m_F = 0$ to the $6^2S_{1/2}$ $F = 4$, $m_F = 0$, which has a frequency of 9.19263177 GHz

One advantage of the transition between these two states of the cesium atoms is the low sensitivity to external perturbations [22]. However, this transition is not completely immune to environmental effects, such as Doppler effect [24], recoil effect [25] and collision broadening [26]. During the 60 year development of microwave atomic clocks, the improvement of the precision of the microwave clocks were about one order of magnitude per decade [19]. The fountain standard [27] of Cs atoms, using the cold atoms technologies [28], reaches uncertainties around 10^{-16} [3]. Some other elements, such as Rubidium [29] for its low cost size and Hydrogen [30] for its short-term stability, are also used to make microwave clocks. Wide applications of the microwave clocks with different precision had been built. For example, clock

based on hot rubidium cells [31] with precision of 10^{-12} and volume of 0.05 L had been commercially available.

1.3 Optical clocks

To evaluate the atomic clock, there are two critical characters: accuracy and precision. The accuracy of an atomic clock refers to how close the readout frequency matches the natural frequency of the reference atoms. The unperturbed frequency of the clock transition f_{atom} could be shifted by the external environmental effects, mainly magnetic and electric fields [32, 33]. The relativistic shifts [9], arising from the different frames of reference of the atoms and the probing lasers, would also introduce errors to the clock transitions. A lot of the effort for making atomic clocks is to evaluate and reduce those frequency-shifting factors. The precision is determined by the repeatability of the measured frequency over multiple clock cycles. The noise from the measurement protocol would limit the precision performance. One typical method to characterize the precision is the Allan deviation [34] which can be expressed as

$$\sigma(\tau) = \frac{1}{2\pi f_{atom}\sqrt{NT_m\tau}}, \tag{1.1}$$

where $\sigma(\tau)$ is the Allan deviation, τ is a certain averaging time, N is the interrogated atom number and T_m is the free-precession time in the Ramsey method [35]. Equation 1.1 shows that clock transition working in a higher frequency regime would lead to improvement of the clock precision.

After the invention of laser, an optical-range electromagnetic wave with narrow linewidth, researchers considered exploring its ability to probe atomic transitions for making optical clocks. Comparing to the atomic clocks working in the microwave range, the ones working in the optical range could theoretically increase the insta-

bility by 4 to 5 orders of magnitude. However, the accurate, precise and convenient measurement of the optical frequencies were beyond the capabilities of normal electronics. To obtain the high precision optical clock signals, the complicated frequency chain [36] were needed to convert the optical frequencies to microwave signals. The unreliable and large apparatus limits the application of the optical clocks. Fortunately, the development of the optical frequency comb, which consists of a series of equally spaced elements in the frequency domain and covers the frequencies from microwave range to the optical range, enabled the direct measurement of optical frequencies at the turn of the century [37–39]. With the realization of optical frequency atomic clocks, the clock community entered a new era, pushing clock accuracy and precision to unprecedented limits.

1.3.1 Principle of the optical lattice clocks

There are two kinds of optical clocks leading the time-keeping development: the ion optical clocks and the neutral atoms optical lattice clocks. The ion clocks using the transitions in ions as the clock laser reference [40]. The advantage of the ion optical clocks are the unperturbed environment for spectroscopy and long trapping times. However, the interrogation of multiple ions simultaneously is still a challenge [41]. Using atoms tightly confined in optical lattice is an alternative methods which has the advantage of a large atom number as indicated in Equation 1.1. A typical optical lattice clock consists of three functional modules – a pre-stabilized clock laser whose frequency is on resonance with the atomic reference, neutral atoms trapped in an optical lattice and a frequency comb which output the electrically usable signal, as seen in Figure 1.2.

For the clock laser, in free-running mode, its linewidth is wider than the atomic
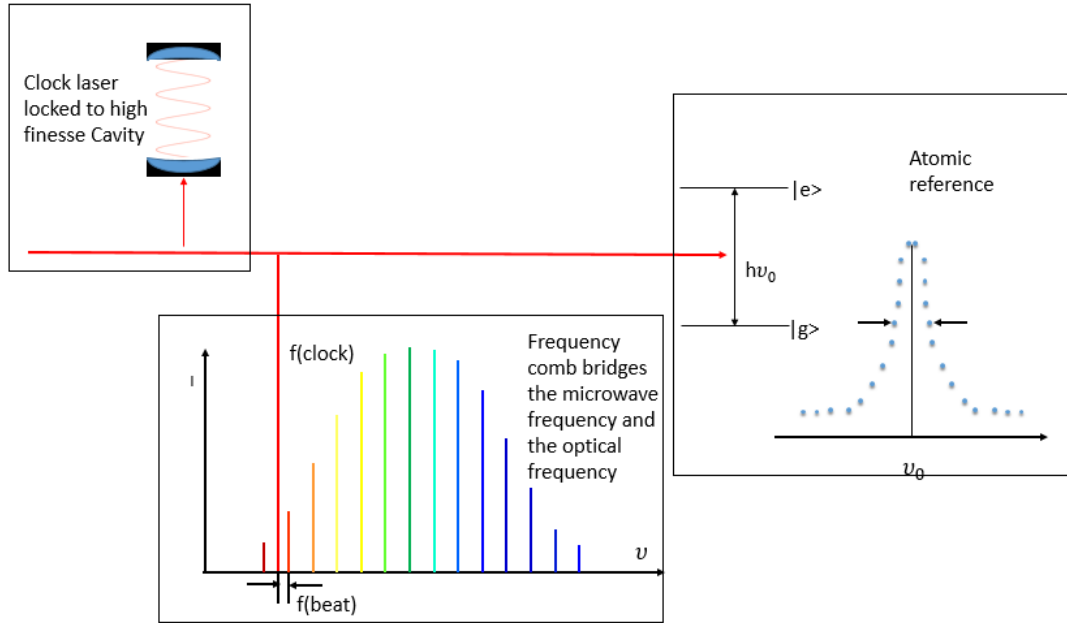
Figure 1.2: Basic structure of an optical atomic clock: The cavity with ultra high finesse transfers its stability to the clock laser for short term stability. The clock laser interrogates the atoms, holding its frequency on resonance with the atomic transition. Beating the clock laser and one tooth of the frequency comb, the resulting microwave signal which inherits the precision of the extremely narrow atomic transition is the clock signal.

transition linewidth. For example, a typical external-cavity diode laser (ECDL) have a linewidth in the MHz level while the linewidth of the chosen atomic transition is the the Hz level. Using the laser to probe the atoms, one could not get needed high resolution spectroscopy. Another drawback of the lasers without pre-stabilization is that their frequency would drift between the continuous measurements which introduces extra noise to decrease the precision. To compress the linewidth and prevent the drift, the clock lasers are designed locked to high finesse cavities. These cavities are generally made by ultra low expansion(ULE) glass and placed inside high vacuum environments [42] which thermally stabilize the cavity length.

With the narrow linewidth clock lasers, performing spectroscopy on hot neutral atoms which have velocities and velocity distributions would still be limited by the Doppler frequency shift and Doppler broadening. The absorption of the one clock laser photon would lead to kHz level frequency shift. Using laser cooling [43] to

reduce the temperature of the atoms, μK or nK temperature could be achieved for the atoms. However, in such low temperature, the Doppler broadened linewidth is also at the kHz level. Since the probing would always transfer momentum to the atoms which leads to the frequency shift, the Doppler free spectroscopy is not achievable. One solution is to load these cooled atoms into a off resonance optical lattice whose depth of the potential is larger than the thermal energy of the atoms [44]. In such case, the photon recoil momentum of the clock laser being taken by the lattice, the Doppler free spectroscopy is enabled. The existence of the lattice would cause Stark shift of the two energy levels of the clock transition which is another error source of the system. The magic wavelength optical lattice was proposed to solve this problem by Katori [45] in 2003. Since the frequency shifts are inevitable, making the two energy levels moving to the same direction with the same quantity would cancel the frequency shift. This magic wavelength optical lattice scheme paves the way to the rapid development of the neutral atomic optical clocks.

In the time domain, the frequency comb is a regularly spaced pulse train generated by a mode locked laser. The separation time of those ultra short pulses is τ_{rep}. In the frequency domain, the frequency comb is a spectrum with a series of equally spaced frequency peaks. The distance between the neighboring peaks is the pulse repetition rate $f_{rep} = 1/\tau_{rep}$ which can be measured by a fast photodiode. The components in the comb-like spectrum are not perfectly an integer number times the repetition rate as nf_{rep}, they would have a offset. It could be explained, in the time domain, as the different velocity of the envelope and carrier of the pulse. To determine the carrier-envelope offset (CEO) frequency f_{CEO}. A technique called self-referencing scheme [39] is applied to fix the offset value. Doubling the frequency of the ith mode $f_i = f_{CEO} + if_{rep}$ to $2f_i = 2f_{CEO} + 2if_{rep}$ and then beating the signal with the $2ith$ mode $f_{2i} = f_{CEO} + 2if_{rep}$, the result signal is the offset frequency f_{CEO}.

11

With the two microwave range signal f_{rep} and f_{CEO}, any mode in the frequency comb could be indicate as $f_i = f_{CEO} + i \cdot f_{rep}$. Locking the frequency comb to any frequency standards, combined with the beat-note measurement with one tooth of the comb and the unknown clock laser's frequency, the exact optical frequency could be measured.

1.3.2   Application of the optical lattice clocks

With the accuracy and precision of the laboratory based optical clocks outperform their microwave counterparts, the optical clocks has the potential to take the place of microwave ones. For example, the definition of the SI unit second is on Cesium and possibly the next definition would be based on Strontium [46]. Those ultra stable optical clock in the laboratories would also carry out some fundamental physics measurements, such as the fine structure constant α measurement since the clock transition's dependence on this constant [41]. Einstein's theory of general relativity predicts that in a gravitational potential, the clocks would tick slower. Typically, 1cm change of the height near the surface of the earth would leads to a change of the clock frequency in the 10^{-18} level. Artificially adding a height change of the tens of centimeter level to the optical clock with accuracy in the 10^{-18} level. The output clock frequency would have a change in the 10^{-17} level.

Another approach for expanding the optical clocks' application is to make the clock system mobile or even miniaturized. One application of the mobile optical clocks would be the precision geodesy that maps the gravitational fields [47]. Comparing the optical frequency standards in different laboratories with mobile optical clocks is competing with the comparison scheme using the fiber network [48]. The miniaturized optical lattice clock could replace the microwave ones on the global navigation

satellite system(GNSS). There long term stability and ultra-low drift would bene-fits the navigation system for extended operation between re-synchronization. The optical clocks in space could also serve as the master clock in space to synchronize other microwave clocks in space [49].

Chapter 2

Useful Concepts for Strontium Optical Lattice Clock

As mentioned in Chapter 1, we are looking for atomic transitions with narrow linewidths to use as the clock reference. The uncertainty principle tells us that longer lifetimes result in narrower linewidths.

$$\gamma \sim \frac{\Delta E}{h} \sim \frac{1}{2\pi\Delta t},$$

(2.1)

where γ is the natural linewidth of the transition, ΔE is the energy difference between the two energy levels, h is Planck's constant and Δt is the lifetime of the excited state. For allowed transitions with short lifetimes in the 10^{-8} s level, their natural linewidths will be in the MHz range. Since the transition probability for metastable states is much smaller than the allowed transitions, the metastable states usually have longer lifetimes on the order of seconds. Therefore these transitions with narrower linewidths are suitable candidates for a clock reference. The challenge is to isolate the atoms or ions from the environment, which can shift or broaden those naturally narrow transition frequencies. In the case of room temperature atoms, their speed will be in the range of hundreds of meters per second for dilute gases. Due to the Doppler effect, the resonant frequency $f_{Doppler}$ of a moving atom is different from the resonant frequency f_{still} of an atom at rest. Another drawback caused

by the Doppler effect is the transition linewidth broadening due to the velocity distribution of the atoms. The Doppler broadened transition linewidths may be orders of magnitude wider than the natural linewidths. For example, the strontium atom has a transition $5s^2\ {}^3S_0 \rightarrow 5s5p\ {}^3P_0$ whose frequency is around 4.29×10^{14}Hz while the natural linewidth is in the sub-Hz level. At the room temperature around 25^oC would introduce a Doppler broadening around 700 MHz. Once the reference atom species have been selected, the first step will focus on reducing the Doppler shift, and therefore the shift and broadening of the transition. This corresponds to reducing the velocity of the atoms, in other words lowering the temperature of the atoms.

This chapter will introduce the essential cold atoms theory and technology for cooling neutral atoms in the optical lattice clocks. Then the characteristics of the strontium atoms used in our experiment will be presented.

2.1   Cold atoms

The theory and technology behind making "cold atoms", using the techniques developed in the 1980s for laser cooling and trapping of neutral atoms, quickly became one of the most powerful tools in atomic physics [50–52]. These techniques enable atoms to be cooled to temperatures approaching absolute zero. As a result, the transition broadening and energy level shifts due to the Doppler effect in fast moving atoms can be dramatically reduced, and the quantum nature of the small particles can be exposed.

2.1.1 Laser cooling

Photon absorption and emission is a quantum process. However the key ideas behind laser cooling can be described classically. When an atom absorbs a photon, the total energy and momentum of the atom-photon system remains the same due to energy and momentum conservation. The momentum change of the atom is equal to the momentum of the photon $\vec{p}_{ab} = \hbar\vec{k}$, where $|\vec{k}| = 2\pi/\lambda$ is the wave vector relating to the wavelength λ of the light. An atom in the excited state will decay to the ground state and emit a photon with momentum $\vec{p}_{em}$ by spontaneous emission when the laser intensity is low. If the absorption-emission process repeats, after a large number of cycles, the total momentum change of the atom is

$$\Delta\vec{p} = \sum_N \vec{p}_{ab} + \sum_N \vec{p}_{em}. \qquad (2.2)$$

As the photons are emitted in random directions, the second term on the right-hand side of Equation 2.2 averages to zero. Therefore the net momentum change is simplified to $\Delta p_{net} = N\hbar\vec{k}$, and the resulting force is given by

$$\vec{F} = d\vec{p}_{net}/dt = \Gamma\hbar\vec{k}, \qquad (2.3)$$

where Γ is the atom excitation rate which depends on the difference between the laser's angular frequency ω_{la} and the atomic resonance frequency ω_{at}. In the atom's reference frame, the excitation rate Γ is expressed as

$$\Gamma = \frac{\Gamma_{na}}{2} \frac{s_0}{1 + s_0 + (2(\Delta + \omega_D)/\Gamma_{na})^2}, \qquad (2.4)$$

where Γ_{na} is the decay rate of the excited state as well as the linewidth of the transition, $s_0 = I/I_{sat}$ is the ratio of the laser intensity I to the saturation intensity I_{sat}, $\Delta = \omega_{la} - \omega_{at}$ is the frequency detuning of the laser and $\omega_D = -\vec{k} \cdot \vec{v}$ is the Doppler shifted frequency.
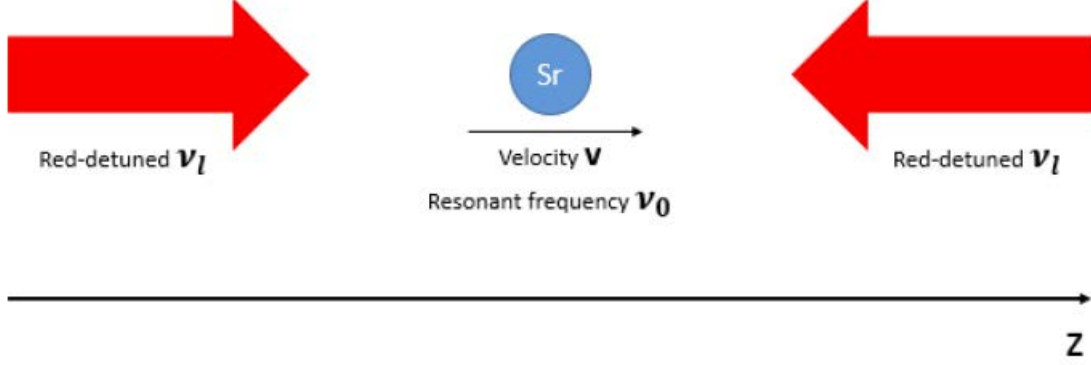
Figure 2.1: One pairs of opposing red-detuned laser beams are applied to the atoms. It generates a velocity dependent force which viscously damps the atomic motion in the Z axis. As the similarity with a viscous fluid, the light field is called "optical molasses"

Considering a simple one dimension situation as in Figure 2.1, the atom is moving along the z axis and there are two counter-propagating low intensity laser beams on the same axis. The frequency of the laser ν_l is lower than the atomic transition frequency ν_0. In the atom's reference frame, the laser beam in the opposite direction is equivalently blue shifted and the other one is red shifted. The force from the two beams can be added together as

$$F_{OM} = \vec{F}_+ + \vec{F}_- = \left(\frac{\hbar \vec{k} s_0 \frac{\Gamma_{na}}{2}}{1 + s_0 + \left(\frac{2(\Delta - k\nu)}{\Gamma_{na}} \right)^2} \right) + \left(\frac{\hbar \vec{k} s_0 \frac{\Gamma_{na}}{2}}{1 + s_0 + \left(\frac{2(\Delta + k\nu)}{\Gamma_{na}} \right)^2} \right), \quad (2.5)$$

where $\vec{F}_+$ is the beam propagating along the same direction as the atoms' direction of motion, while $\vec{F}_-$ is the beam propagating along the opposite direction. For $\Delta < 0$, atoms in the light field experience a viscous force which reduces the velocity. The cooling mechanism described above is called Doppler cooling because the sci-

entific principle uses the Doppler effect, which shifts the resonant frequency of the transition. However, the velocity of the atoms cannot reach zero as the momentum and energy exchange between the light field and the atoms is not continuous. As the temperature corresponds to the velocity of an atomic sample, the temperature of the atoms cannot reach absolute zero. There are two characteristic temperatures important in laser cooling techniques – the Doppler limit and the recoil limit. For simplified two level atoms, the Doppler limit is the lowest achievable temperature in Doppler cooling processes. The temperature relates to the natural linewidth of the atomic transition:

$$T_D = \frac{\hbar \Gamma_{na}}{2 k_B}.$$
(2.6)

where k_B is the Boltzmann constant. The other relevant temperature limit is the recoil limit, which arises because any emitted photon transfers a non-zero amount of momentum to the atom. The recoil velocity for atoms with mass m is $v_r = \hbar |\vec{k}| / m$. The temperature corresponding to the recoil limit is

$$T_r = \frac{\hbar^2 |\vec{k}|^2}{m k_B}.$$
(2.7)

In certain specific situations, it may be possible to surpass these limits. For atoms with degenerate energy levels, Sisyphus cooling [53] can cool beyond the Doppler limit. This cooling mechanism is achieved by shining two counter-propagating laser beams with orthogonal polarization on to the atoms. The atoms moving in the standing wave with a polarization gradient lose the kinetic energy to reach the potential maximum. When the atoms reach the maximum, the optical pumping would move them to the lower potential state.

For ^{88}Sr atoms, two transitions are used to pre-cool the atoms. The $^1S_0 - ^1P_1$

transition has a linewidth of 32 MHz. From Equation 2.5, this broad transition enables a large cooling force for efficient cooling of a large number of hot atoms. From Equation 2.6, this transition, with a relatively large linewidth, suffers from a high Doppler temperature in the low mK range. The $^1S_0 - ^3P_1$ cooling transition is an intercombination transition with a narrow 7.6 kHz linewidth. This narrow transition cools the atoms to a lower temperature. The calculated two limit temperatures are listed in Table 2.1.

Transition	Wavelength	I_{sat}	T_D	T_r
$^1S_0 - ^1P_1$	461 nm	43 mW/cm^2	770 μK	1.03 μK
$^1S_0 - ^3P_1$	689 nm	3 μW/cm^2	180 nK	460 nK

Table 2.1: Doppler limit and recoil limit of the two ^{88}Sr cooling transitions

Calculations show the recoil limit is higher than the Doppler limit for the second stage cooling. Typically, after the second stage cooling the atoms' temperature reaches the low μK level in experiments.

2.1.2 Magneto optical trap

The slowing force in an optical molasses is not a restoring force, so the atoms will not remain spatially trapped. Ultimately, the slowed atoms will leave the centre of the light field by collisions. The atoms will only be trapped in a region of space in the presence of a position dependent force. An external magnetic field induces the Zeeman effect shifting the energy levels. In the presence of an external magnetic field, ω_{at} varies with the position, which means that Δ in Equation 2.5 is position dependent. An apparatus employing both an optical molasses and a quadrupole field generated by anti-Helmholtz coils is called a magneto-optical trap (MOT). At the center of the quadrupole field the magnetic filed is zero and the gradient near the center is almost constant.
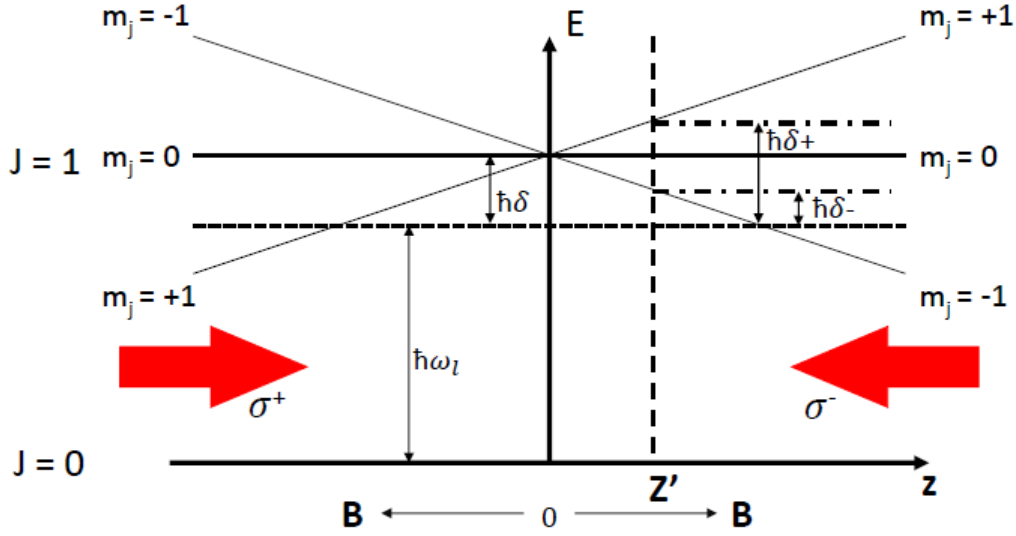
Figure 2.2: Diagram of the 1D MOT consisting of optical and magnetic field. The $J_{=1}$ state is shifted by the quadrupole magnetic filed. The red color of the light beams indicates that the laser is red detuned.

Figure 2.2 shows an arrangement for a MOT in 1D. One pair of red detuned ($\Delta < 0$) counter-propagating laser beams have the same intensity and opposite circular polarizations (the σ^- laser points from z > 0 to z < 0, the σ^+ laser points from z > 0 to z < 0). Along the z axis is a linear magnetic field $B(z) = Az$, where A is the magnetic field gradient. In the $J = 0 \rightarrow J = 1$ transition, the excited state is split into three sub-states $m_j = 0, \pm 1$ which have different shifts along the z axis. $m_j = +1$ is shifted up for $B > 0$ and down for $B < 0$, $m_j = -1$ is the opposite and $m_j = 0$ has no shift. Because the opposite circular polarizations, the effective detuning for the atoms are different. Atoms on the positive side of the z axis absorb more photons from the σ^- laser beam because of the absorption law of photons due to spin. On the negative z axis, atoms absorb more photons from the σ^+ laser. All the atoms experience a force pointing towards the center of the trap. The Zeeman

detuning leads to a modification of Equation 2.5:

$$\vec{F}_{1DMOT} = \frac{\hbar s_0 \vec{k}\frac{\Gamma_{na}}{2}}{1 + s_0 + (2(\Delta - \omega_D + \mu'B/\hbar)/\Gamma_{na})^2} - \frac{\hbar s_0 \vec{k}\frac{\Gamma_{na}}{2}}{1 + s_0 + (2(\Delta + \omega_D - \mu'B/\hbar)/\Gamma_{na})^2}.$$
(2.8)

where $\mu' = (g_e M_e - g_g M_g)\mu_B/\hbar$ is the transition's magnetic moment, g_e and g_g are the Landé g-factors of the excited and ground states, respectively, M_e and M_g are the magnetic quantum numbers and μ_B is the Bohr magneton. When the detuning Δ is larger than the Doppler and Zeeman shifts, ignoring $(\vec{k}\vec{v}/\Gamma_{nat})^4$ and higher order terms, Equation 2.8 can be simplified to

$$\vec{F}_{1DMOT} \cong -\beta\vec{v} - \kappa\vec{r} \equiv -\frac{8\hbar|\vec{k}|^2\Delta s_0}{\Gamma_{nat}(1 + s_0 + (2\Delta/\Gamma_{nat}))^2}\vec{v} - \frac{\mu'A\beta}{\hbar|\vec{k}|}\vec{r}$$
(2.9)

where β is the damping coefficient due to the light-atom interaction and κ is the spring constant. The one dimensional case can be easily extended to 3D. A pair of anti-Helmholtz coils can generate the required magnetic field gradient. Shown in Figure 2.3, the basic configuration of the 3D MOT consists of an anti-Helmholtz coil and 6 circularly polarized beams.

There are two other popular pre-cooling methods using the Zeeman effect: 2D MOT [12, 54, 55] and Zeeman slower [56, 57]. For a 2D MOT apparatus, it expands the 1D MOT scheme described in Figure 2.2 to a two dimensional one. The atoms are cooled and trapped in the two dimensions with cooling laser. A pushing beam would push the pre-cooled atoms in the 2D MOT to a 3D MOT to increase the loading rate of the 3D MOT. One advantage of the 2D MOT is that the atomic source does not necessarily need to be mounted with direct line of sight with the 3D MOT. The Zeeman slower is widely used for cooling strontium. The basic idea is to change the Zeeman shift along the atomic propagation path by a changing magnetic field.
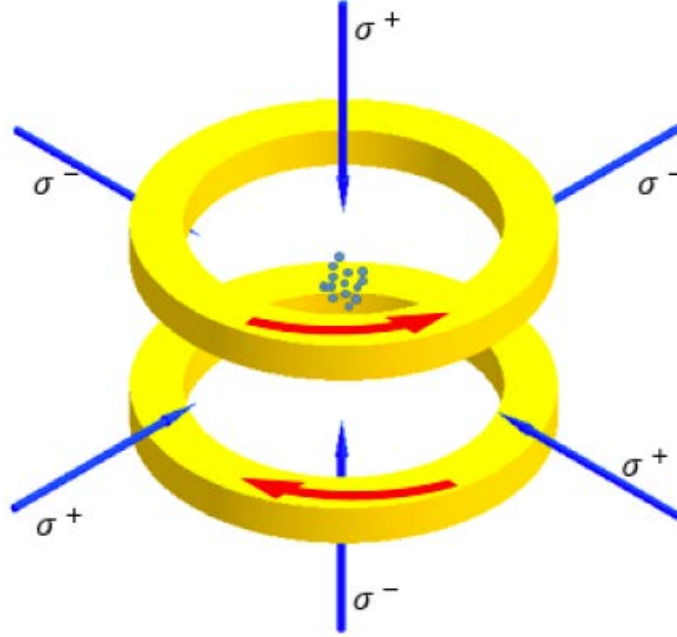
Figure 2.3: A schematic diagram of a 3D MOT. The red arrows on the coils indicate the current directions. For anti-Helmholtz coil, the current direction are antiparallel.

The changed Zeeman shift keeps compensating the detuning of the interested atoms whose velocities are changed by the cooling.

2.1.3 Optical lattice and magic wavelength

Under ideal conditions, the temperature of ^{88}Sr atoms after the second Doppler cooling stage can reach 180 nK (see Table 2.1). At this temperature, Doppler broadening of the clock transition linewidth is still at the kHz level, which is too broad for use in a precise clock. Interrogation of the atoms with the clock laser can also shift the transition frequency due to momentum exchange. Loading the atoms into a optical lattice with large potential depth can solve this problem. In an appropriate harmonic potential, atoms occupy the lowest available vibrational energy states, and their positions are confined in a region much smaller than the lattice wavelength.

The optical lattice is made by reflecting the diople trap [43] beam to generate a

standing wave light field. For a 1D optical lattice orientated along the z axis, a linearly polarized laser beam with intensity I_l is retroreflected by a mirror. The distance between two intensity nodes is $\lambda_l/2$. The optical potential experienced by the atoms is

$$U(r,z) = U_0 exp\{-2[r/\omega(z)]^2\}cos^2(2\pi z/\lambda_l) = -\frac{8\pi}{c}\alpha(\omega_l)I_l exp\{-2[r/\omega(z)]^2\}cos^2(2\pi z/\lambda_l),$$
(2.10)

where r is the radial coordinate in the transverse direction, U_0 is the potential depth, $\omega(z)$ is the beam waist of the laser and $\alpha(\omega_l)$ is the polarizability determined by the lattice laser frequency ω_l. Along the z axis, this potential is periodic, and the wells are well approximated by harmonic potentials. The energy difference between the discrete harmonic energy levels is

$$\omega(h) = \frac{2\pi}{\lambda_l}(\frac{2|U_0|}{m})^{1/2},$$
(2.11)

where m is the mass of an atom. When a clock laser interrogates the $^1S_0 - ^3P_0$ transition, the momentum change on one atom is p_{ab}. If the recoil energy $E_r = p_{ab}^2/2m$ is smaller than the spacing of the harmonic potential energy levels $\hbar\omega_h$, the motional state of the atoms will not change. This quantum regime is called the Lamb-Dicke regime [45].

The existence of a light field independently shifts the two energy levels of the clock transition due to the AC-Stark effect. The shift δE_i^{Stark} on each energy level i is expressed as

$$\delta E_i^{Stark} = -\alpha_i(\omega_l)(\frac{\varepsilon_l}{2})^2 - \alpha_i'(\omega_l)(\frac{\varepsilon_l}{2})^4 + O(\varepsilon_l^6)$$
(2.12)

where ε_l is the amplitude of the lattice laser, $\alpha_i(\omega_l)$ and $\alpha_i'(\omega_l)$ are the dynamic polarizability and hyperpolarizability, respectively. Since both states $^1S_0$ and $^3P_0$

are shifted, the effective change on the clock frequency is

$$h\Delta\nu^{Stark} = -\Delta\alpha(\omega_l)(\frac{\varepsilon_l}{2})^2 - \Delta\alpha'(\omega_l)(\frac{\varepsilon_l}{2})^4 + O(\varepsilon_l^6) \tag{2.13}$$

where $\Delta\alpha(\omega_l) = \alpha_e(\omega_l) - \alpha_g(\omega_l)$ is the differential polarizability, which is dependent on the lattice laser frequency. Neglecting higher orders, a so-called magic wavelength λ_m is one which cancels the difference between the dynamic polarizabilities of the two interested atomic states. Typically, 813 nm is chosen as the optical lattice wavelength [44]. With a "magic wavelength" optical lattice, the AC-Stark shifts from the lattice which strongly effect the accuracy of strontium clocks are largely reduced. During the strontium optical lattice clock operation, the lattice laser in constantly on. The loading to the lattice happens after the second stage Doppler cooling.

2.2   Strontium atoms

Neutral strontium atoms, as well as other alkaline earth atoms, have two valence electrons in the outermost occupied shell. Consisting of many energy levels, the valence shell determines many of the physical and chemical properties of atoms. Based on the total spin angular momentum, these energy levels can be separated into two classes: singlet states (parallel, total spin angular momentum $S = 1$) and triplet states (anti-parallel, total spin angular momentum $S = 0$). According to the selection rule $\Delta S = 0$, electric dipole transitions between the singlet states and the triplet states are forbidden. However, due to spin-orbit coupling, these transitions are not completely forbidden. The semi-forbidden transitions (intercombination lines) have long lifetimes, therefore the radiation linewidths are very narrow, a favorable prop-

erty for metrology.

Strontium has four naturally occurring isotopes: ^{88}Sr, ^{87}Sr,^{86}Sr,^{84}Sr with relative abundances of 82.6%, 7%, 9.9% and 0.56%, respectively [58]. As frequency standards, ^{88}Sr and ^{87}Sr have historically attracted the most interest. The fermionic isotope, ^{87}Sr, has a nonzero nuclear spin (9/2) and a corresponding hyperfine mixing in the $^3P_0$ state, which enables a weakly allowed clock transition. The bosonic isotope, ^{88}Sr, which has no nuclear spin, can still be used for clocks by inducing dipole coupling between states with an external field [59, 60]. Both ^{88}Sr and ^{87}Sr have benefits and disadvantages for serving as an atomic reference. For example, high precision spectroscopy from the ^{88}Sr has a better signal to noise ratio, which stems from the higher natural abundance and simpler cooling process, while ^{87}Sr experiences smaller collisional shifts and will not experience an extra field, which are required by the ^{88}Sr atoms to mix the two clock transition, induced Stark shift or Zeeman shift. ^{88}Sr and ^{87}Sr clocks have been built and explored in clock laboratories around the world [4,44,61–63]. At the University of Birmingham, we currently focus on ^{88}Sr because the miniaturized clock will benefit from the uncomplicated cooling and trapping procedure.

As stated before, the two valence electrons generate the long lifetime intercombination lines. Atoms with similar structure are widely investigated as possible frequency reference candidates. For example, neutral atom optical clocks based on Mg [64], Ca [65], Sr [4,44], Yb [66,67] and Hg [68,69] have been constructed in the laboratory. Among the most promising elements, strontium clocks perhaps benefit most from existing laser technologies. All the necessary lasers, from those which prepare the atoms to those that detect the clock transition, are in a range achievable by laser diodes. These low power consuming, user friendly diode lasers provide a promising start for the miniaturization of strontium optical clocks.

A large number of atoms trapped in an optical lattice are required to reduce the uncertainty of lattice clocks. By taking advantage of strontium's convenient atomic energy level structure, we can efficiently transfer atoms from a hot atomic vapor into a cloud of tightly trapped cold atoms. Experimentally, strontium requires two cooling stages, making use of two different energy transitions. The first cooling transition, at 461 nm, has a broad linewidth of $\Gamma/2\pi = 32$ MHz and serves to pre-cool the hot (≈ 700 K) atoms down to ≈ 1 mK. The second cooling transition, at 689 nm, has a narrower linewidth of $\Gamma/2\pi = 7$ kHz and cools the atoms even further down to $\approx 1\mu$K before they are loaded into the lattice. In addition, two repumping transitions at 679 nm and 707 nm are used to close the first stage cooling cycle. The relevant energy levels in strontium can be seen in Fig 2.1, which uses the Russel-Saunders notation of $^{2S+1}L_J$. S, L and J represent the total spin momentum, orbital angular momentum and total angular momentum of the state, respectively.

1. 461 nm 1st stage cooling: A blue laser resonant with the $5s^2\ ^1S_0 \rightarrow 5s5p\ ^1P_1$ transition is applied to the strontium atoms for the first stage cooling. This broad transition has a natural linewidth of 32 MHz and a wavelength of 460.8618 nm in vacuum. Most of the atoms in the excited state will decay directly back to the ground state, but a small percentage will branch into the $5s5p\ ^1P_1 \rightarrow 5s4d\ ^1D_2$ decay path with a probability of 10^{-5}. Of the atoms that decayed into the $^1D_2$ state, 34% will then decay into the metastable $5s5p\ ^3P_2$ state with the other 66% decaying into the $5s5p\ ^3P_1$ state. Atoms in the metastable $^3P_2$ state are effectively left to the cooling cycle, while the atoms in the $^3P_1$ state may continue to decay back down to the ground state.

2. 707 nm & 679 nm repumpers: Atoms in the $5s5p\ ^3P_1$ state, which have a lifetime of 21 μs, will decay directly back to the ground state, but the long lifetime of the metastable $5s5p\ ^3P_2$ state means these atoms are no longer a part of the cooling cycle.
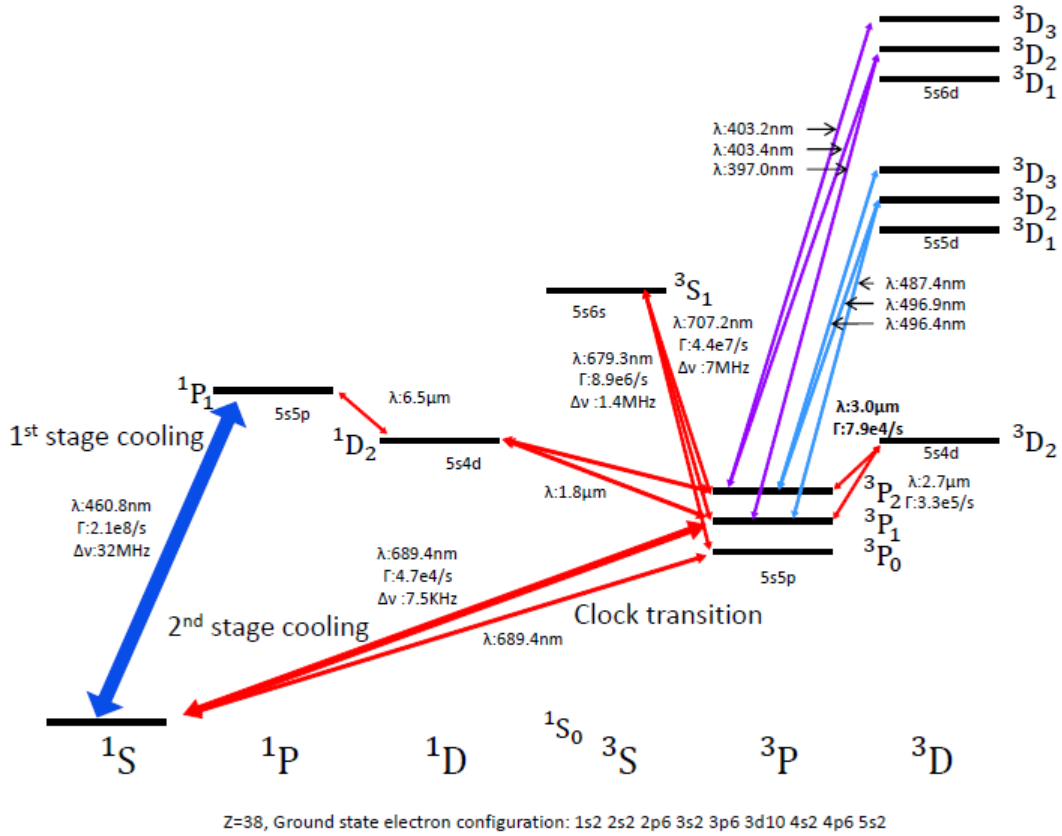
Figure 2.4: Relevant transitions of strontium atoms. All reported wavelengths are measured in vacuum. The $5s^2$ $^1S_0 \rightarrow 5s5p$ $^1P_1$ transition is used for the first stage cooling, the $5s^2$ $^3S_0 \rightarrow 5s5p$ $^3P_1$ transition is used for the second stage cooling and the $5s^2$ $^3S_0 \rightarrow 5s5p$ $^3P_0$ transition is the clock transition.

Due to the commercial availability of laser diodes at the necessary wavelengths, most strontium clock experiments [70] use a 707.2019 nm laser to repump atoms using the $5s5p$ $^3P_2 \rightarrow 5s6s$ $^3S_1$ transition. Once in the $^3S_1$ state, atoms may decay into any state in the ^3P_J manifold. Atoms that decay into the $^3P_0$ state, which also happens to be the excited state of the clock transition, are also lost to the cooling cycle and must be repumped again into the $^3S_1$ state using a laser with a wavelength of 679.2890 nm.

3. 3.0 μm repumper: Unlike the widely used 707 nm and 679 nm combined repumper setup, there are repumping configurations which only require one laser. The $5s4d$ $^3D_2$ can be used to bridge the $5s5p$ $^3P_1$ and $5s5p$ $^3P_2$ states [71]. A laser with a

wavelength of 3.0 μm can drive the atoms from $^3P_2$ to $^3D_2$, from which the atoms can decay back to the 5s5p $^3P_1$ state. The single laser repumper setup would benefit the portable strontium clock since it only needs one laser system.

4. 497 nm repumper: A 497 nm laser is another option for a single laser repumping configuration. The 497 nm laser addresses the 5s5p $^3P_2 \rightarrow$ 5s5d $^3D_2$ states [72]. Compared to the 3.0 μm repumper, the advantage of the 497 nm laser is that the vacuum viewport and coating material already coincides with the requirements of the other lasers used in the experiment. However, 497 nm laser diodes are not currently commercially available.

5. 689 nm 2nd stage cooling: After the first stage cooling cycle, the temperature of the atoms will be at the mK level. Then the 5s^2 $^3S_0 \rightarrow$ 5s5p $^3P_1$ transition is used to cool the atoms further. The linewidth of the transition is 7.5 kHz. With such a narrow linewidth, loading directly from the first cooling stage to the second cooling stage is inefficient, resulting in a small number of trapped atoms. To improve the transfer efficiency, the linewidth of the 689 nm cooling laser is initially artificially broadened to trap more atoms. The linewidth is then narrowed to the kHz level to cool the atoms to the μK level.

6. 698 nm clock transition: For fermionic ^{87}Sr, the 5s^2 $^3S_0 \rightarrow$ 5s5p $^3P_0$ transition is doubly forbidden, but due to hyperfine state mixing it has a natural linewidth of less than 10 mHz, with a frequency of 429,228,004,229,874.0(1.1) Hz. For bosonic ^{88}Sr, the transition is strictly forbidden. However, with the addition of an external magnetic field to mix the two states of the clock transition [73], a similarly narrow linewidth can be generated for the transition.

Chapter 3

Effort to Reduce the Laser System Size

The neutral strontium optical clock experiments involve lasers which range from ultraviolet to infrared. Fortunately, all these wavelengths can be reached by semiconductor material. Comparing to other lasing mediums, the diode laser have the advantages of easy adjustability, low power consumption and compact size. Compact diode laser systems are one of the technologies enabling mobile strontium clocks. A big part of the work for building miniaturized clocks is to shrink the laser systems. We have built three generations of first stage 461 nm cooling laser in our laboratory. From system dimensions to the power output, each system has its own advantages and drawbacks. The first part of the chapter will introduce the effort to reduce the 461 nm laser size. The lasers need to be delivered to the atoms, we also built robust laser distribution setups to meet the mobility requirement. For the delivery of the lasers, I have built robust laser distribution modules for different experiments.

3.1   461 nm laser system

To reduce the size of the blue laser system which takes a large part of the clock volume, we had tested many cutting edge technologies, from periodically poled potassium titanly phosphate (PPKTP) crystal based frequency doubling [74] to the 461

nm diode laser. In all the presented setups here, either the lasers themselves or their seed lasers are an external cavity diode laser (ECDL) in Littrow configuration. This configuration allows for single-frequency operation as well as frequency adjustment. A schematic of the Littrow configuration can be seen in Figure 3.1. The divergent laser beam from a diode is collimated by a collimation lens. There is a grating mounted on a piezoelectric transducer(PZT) diffracting the incident laser beam. The voltage change on the PZT changes the length of the PZT which leads to the rotation of the grating. For the incident laser beam, a different incident angle θ_i results in a different diffracted wavelength λ. Equation 3.1 gives the grating equation in Littrow configuration:

$$n\lambda = 2d(sin\theta_i + sin\theta_d) = 2dsin\theta_i, \tag{3.1}$$

where n is the order of diffraction, d is the distance between grooves, θ_d is the diffracted angle. In the Littrow configuration, the incident angle is equal to the diffracted angle. Apart from selecting the wavelength, the grating and the back facet of the diode form an Fabry-Pérot(FP) cavity which narrows the linewidth of the output laser.

3.1.1   High power double amplifiers blue laser

Because the lack of commercially available 461 nm laser diodes with a high power output in the range of $>$ 100 mW was available for the 2D MOT experiment (the system is shown in Figure 4.1 for the setup, see [12] for the detailed design), the first generation blue laser system was designed with a frequency doubling scheme – a nonlinear phenomenon which converts the 922 nm infrared laser to 461 nm blue laser with the help of PPKTP crystal. A 922 nm homemade ECDL's output power

30
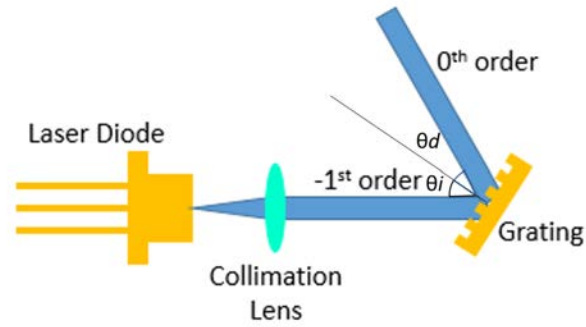
Figure 3.1: The Littrow external cavity laser. The collimation lens determines the size of the output laser beam. To gather the light from the diode, the numerical aperture(NA) of the collimation lens is determined by the divergence of the beam from the diode. The -1st order diffraction is retroreflected back to the diode and the 0th order is the output.

is 50 mW which is then amplified twice to 1.5 W. The high power infrared laser is frequency doubled in the PPKTP crystal in a cavity to generate the 461 nm cooling laser. This design keeps the balance between high power output, high mobility and limited budget. In practice, the system is divided into three functional modules(see Figure 3.2). These three modules are connected with single mode polarization maintaining (PM) fibers. One advantage of the modular design is that components can be easily replaced if better options become available or if a module is damaged.
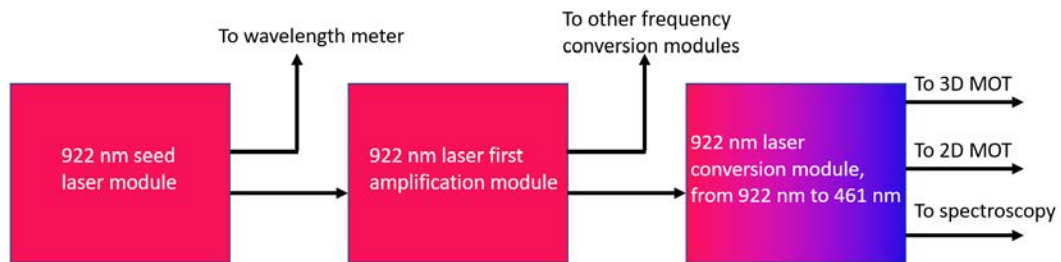
Figure 3.2: Schematic diagram of the first generation 461 nm laser modules. The lines with arrow ends are the fiber connections. The amplification is realized with the semiconductor tapered amplifier(TA).

922 nm seed laser module (Figure 3.3): The 922 nm infrared laser is generated by an ECDL in Littrow configuration. The core components of the seed laser are an anti-reflective(AR) coated laser diode and a grating. The groove density and

31

reflectivity of the grating are 1200 lines/mm and 20% - 30%, respectively. Two low power optical isolators with total isolation of 76 dB are used to suppress instabilities caused by unwanted feedback. The threshold current of the diode is 19 mA. Because of the power loss on the optics, the typical laser power before the fibre coupler is around 30 mW . The imperfection beam profile limits the coupling efficiency to ≈ 50% , the power being sent to the next module is ≈ 18 mW.
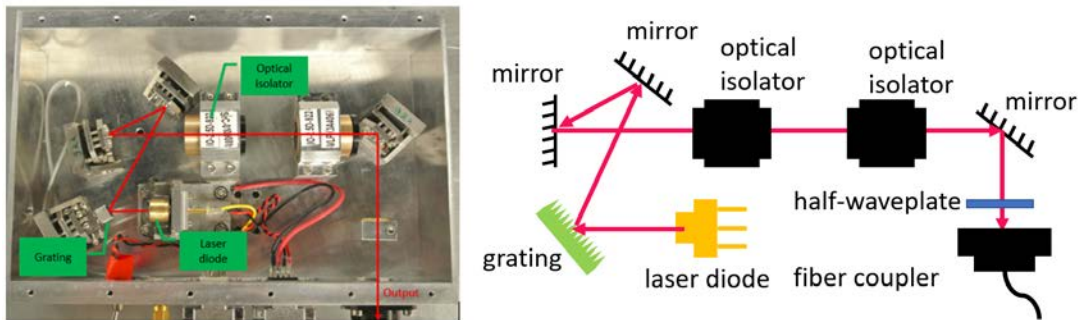
Figure 3.3: The ECDL structure for 922nm diode laser and the following optics are placed in an aluminium box to isolate the temperature drift and the acoustic vibration.

Pre-TA(tapered amplifier) module (Figure 3.4): The recommended seeding power for the 922 nm tapered amplifier(TA) is 50 mW and the corresponding output is 1.5 W. However the output of the seed laser is lower than the recommended value which would limit the output of the TA as well as the final blue laser power. To overcome the power shortage, a pre-TA module was built to pre-amplify the seed laser. After coupling into the pre-TA module through a 922 nm fiber, the divergent laser beam is firstly collimated. The diameter of the beam is 0.9 mm. Then a lens whose focal length is 3.5 mm focuses and couples the beam into the TA. The beam profile after the pre-TA is different from the perfect Gaussian profile. In vertical and horizontal planes, the laser beam has divergence angles of 14° and 28°, respectively. A $f = 2.75$ mm aspherical lens and a $f = 40$ mm cylindrical lens are successively used to shape the beam to a $d = 3$ mm collimated one. The reflections from the 500

mW high power laser may damage the TA chip. To prevent this an optical isolator with 35dB isolation has been installed. Typically, the TA chip amplifies the 18 mW input laser to 500 mW with a current of 2.75 A. 50 mW 922 nm laser is delivered to the next module and 2 mW is sent to the wavelength meter for monitoring the laser frequency. When the single pass wavelength conversion module(from see Section 3.1.2) is coupled to the system, the pre-amplified module is operating at full load – 50 mW out of the 500 mW to the next TA and the rest to single pass frequency doubling module.
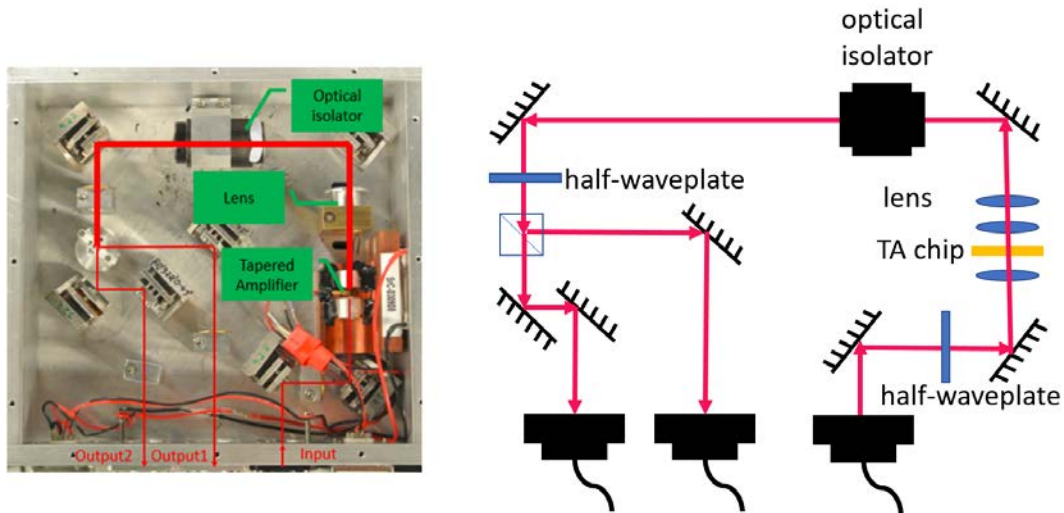
Figure 3.4: The Pre-TA module has two outputs, the power distribution of the output is controlled by a half-wave plate and a polarizing beam splitter (PBS).

TA and frequency doubling module (Figure 3.5): From the pre-TA module, 50 mW laser is transmitted to the TA and frequency doubling module. Similar to the pre-TA module, the same lens are used to collimate the beam and couple the power to the TA chip. The same aspherical and cylindrical lens as used in the pre-TA module are placed after the amplifier to collimate the beam. The possible damage on the TA chip from reflections is again eliminated by a high power optical isolator. For high conversion efficiency, the laser beam size in the PPKTP crystal is adjusted by a telescope before the optical isolate and a focusing lens after the optical isolator.
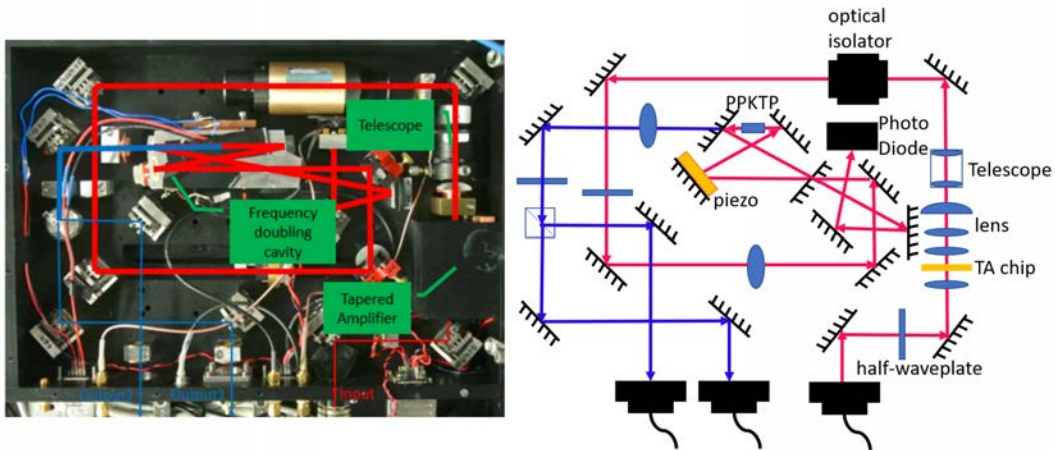
Figure 3.5: The components in the TA and frequency doubling module can be grouped into three function modules – the TA chip for amplifying the power, the telescope and the focusing lens for coupling the power to the cavity, the PPKTP crystal in the monolithic cavity for converting the laser

The distance from the focusing lens to the cavity is variable for fine adjustment.

For a single-pass in the anti-reflection(AR) coated PPKTP crystal, the conversion efficiency is less than 5% which means less than 75 mW 461 nm laser could be generated. The bow-tie monolithic cavity is built to contain the crystal and enable multi-pass of the 1.5 W 922 nm laser. The multi-pass is realized by stabilizing the cavity length to the laser. After locking the cavity to the laser, the output blue laser power is 300 mW and the conversion efficiency reaches 25%.

The detailed second harmonic generation(SHG) theory can be found in Reference [12, 75].

3.1.2 Wavelength conversion module

The 300 mW 461 nm output from the frequency doubling module is divided into three parts – 10 mW for spectroscopy locking, 50 mW for the six beam 3D MOT and the rest for pre-cooling in the 2D MOT. Even with high-reflection(HR) coating for 461 nm, there is tremendous power loss along the light path – 35% - 40% power loss in each fiber coupler, 15% - 20% power loss in each single pass acousto-optic

34

modulator(AOM), 40% power loss in each double pass AOM and 3% - 5% in other optics. The power loss limits the intensity of the cooling laser which affect the atom number trapped in the MOT. Only $(4 \pm 0.4) \times 10^5$ atoms can be trapped by the first stage cooling. To obtain more 461 nm laser power, a commercial fibre integrated wavelength conversion module from NTT(WH-0461-000-A-B-C) was added to the system(see Figure 3.6). The wavelength conversion module contains a fibre integrated 2cm long Periodically Poled Lithium Niobate(PPLN) crystal which doubles the frequency of the seed laser in a single pass. 922 nm laser is coupled to the waveguide fiber by connecting it to a 922 nm fiber via a PM fiber mating sleeve. As introduced in the pre-TA module, only 50 mW out of the 500 mW is delivered to the TA and frequency doubling module, the rest of power now can be coupled to the new single pass frequency doubling waveguide.

Figure 3.6: The wavelength conversion module is mounted on a customized aluminium base.

A customized aluminum base which the waveguide mounts on has the function of heat sink. The temperature phase-matching property [76] is measured by offering 120 mW 922 nm laser into the module while changing the temperature(see Figure

3.7).
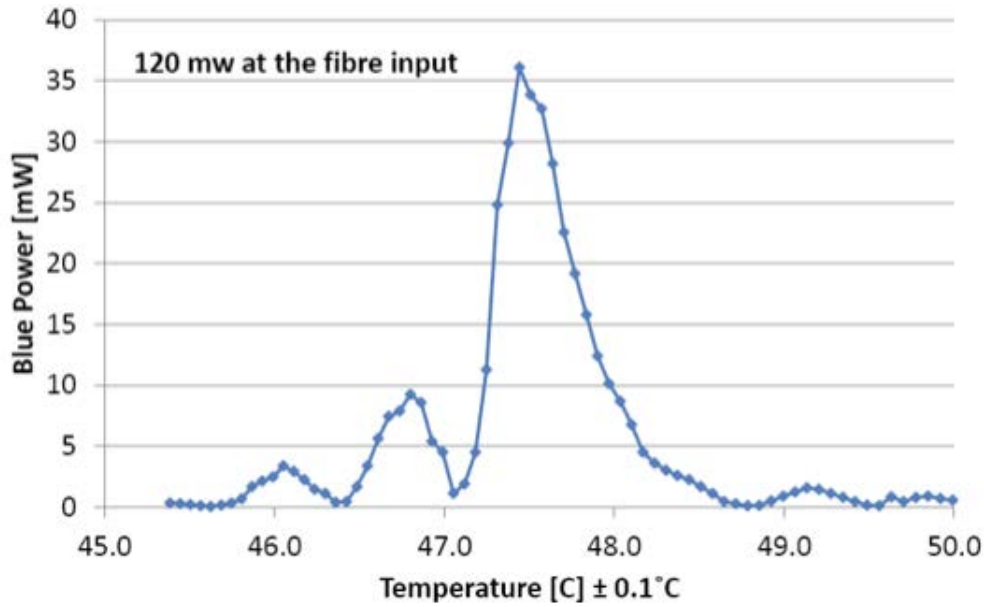
Figure 3.7: Temperature dependence of the wavelength conversion module. Those peaks reveals that it is quasi phase matching in the PPLN crystal.

The suggested input power is 200 mW at 922 nm and the output expectation is 60 mW at 461 nm. However, the coupling efficiency for the 922 nm laser from the pre-TA module is lower than 50%, we have never reached the 200 mW input from the available 500 mW in the pre-TA module. The measured power dependence and the efficiency of the module is in Figure 3.8.

The output light from the waveguide is in free space. The CCD camera beam profiler(Thorlabs BC106-VIS) is used to carry out the profile measurements of the light coming out of the waveguide. In Figure 3.9a, there is a near circular beam with high power density and a lot of side bands with low power density. These side bands are actually the leak 922 nm laser from the output facet of the waveguide. In Figure 3.9b, the device shows a near Gaussian beam profile.

The fiber integrated waveguide has a drawback that the actual power coupled into the PPLN crystal is unmeasurable to properly characterise the waveguide. The power value in the x-axis of Figure 3.8 is measured from the fiber which is connected
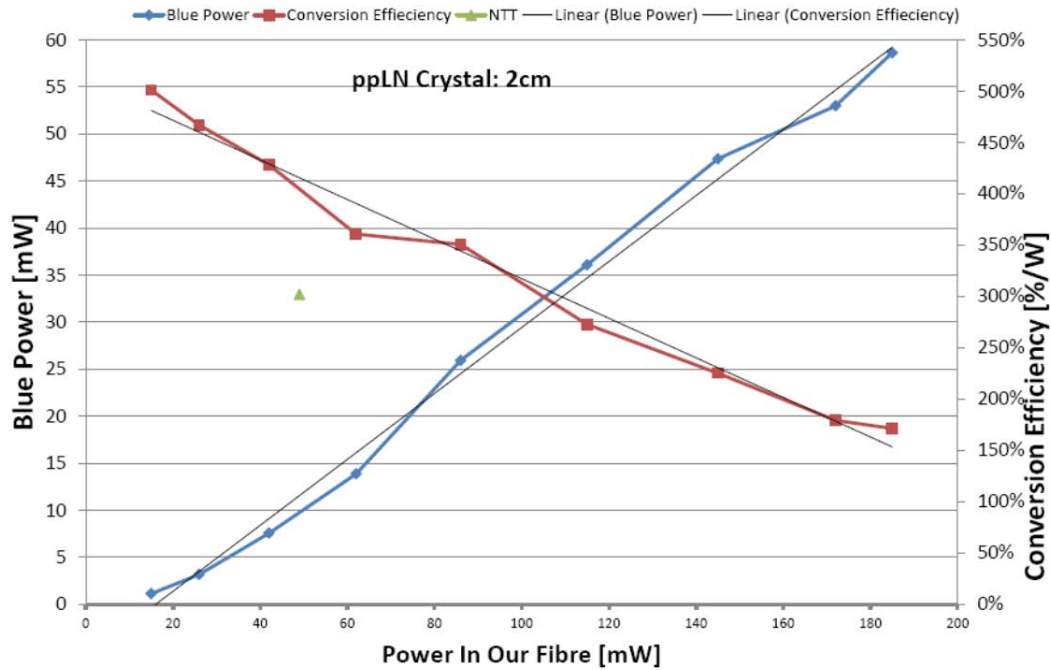
Figure 3.8: The output power and efficiency of the wavelength conversion module: As the input power increases, the conversion efficiency decreases. For the maximum input of 183 mW, the output 461 nm laser is 57 mW. The dropping conversion efficiency conflicts with the theory that the power of the blue power is supposed to change quadratically with the input power. One possible reason is the power loss in the fiber mating sleeve.

to the pre-TA module, but not the fiber to the waveguide. The coupling efficiency of the PM fiber mating sleeve is unknown. Another problem is the aging of the crystal, after one year operation, the output power dropped down to 40 mW with 180 mW 922 nm laser input.

3.1.3 461 nm diode laser

After testing the commercial 461nm diode laser from Newport in 2013, we started to look for 461nm diode on the market. Fortunately, Japanese company Nichia has made some diodes(NDBA116T) whose operating wavelength range covers the interested 461 nm. The output power of the diode reaches 30 mW with 237.6 mA current in our designed system which will be further described in this chapter. The laser beam profile of the diode is elliptical with full angle parallel and perpendicular

37
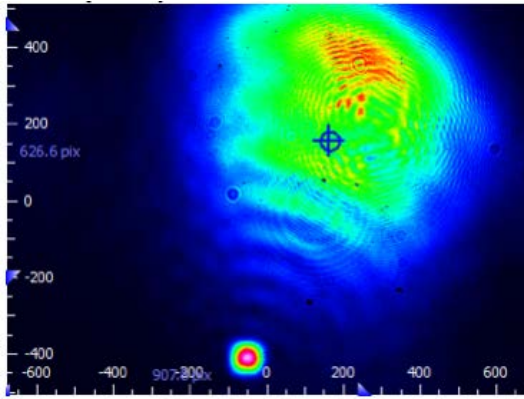
(a) 33 mm way from the output facet. At the bottom: profile of the 461 nm beam. At the top: Profile of the leaked 922 nm seed laser.
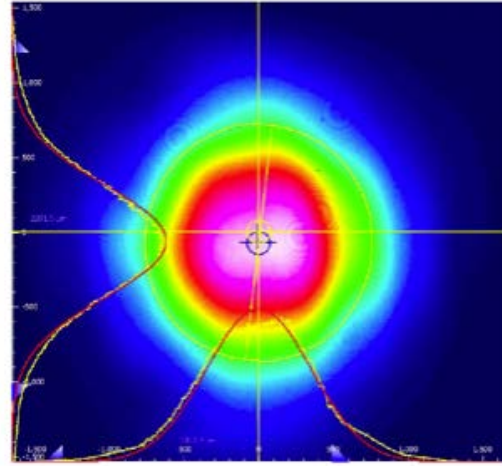
(b) 80 mm away from the output facet. The yellow line is the actual intensity, the red line is the fit to a Gaussian distribution.

Figure 3.9: Beam profile of the wavelength conversion module output.

divergence of 7.9° and 23.9°, respectively. As seen in Figure 3.10, the beam profile is not perfect. We can see some defects in the beam profile. The beam profile measurement was to determine whether we could use the free space laser from the ECDL directly to save some power or we need to generate a Gaussian beam with a fiber at the cost of 35% power loss.
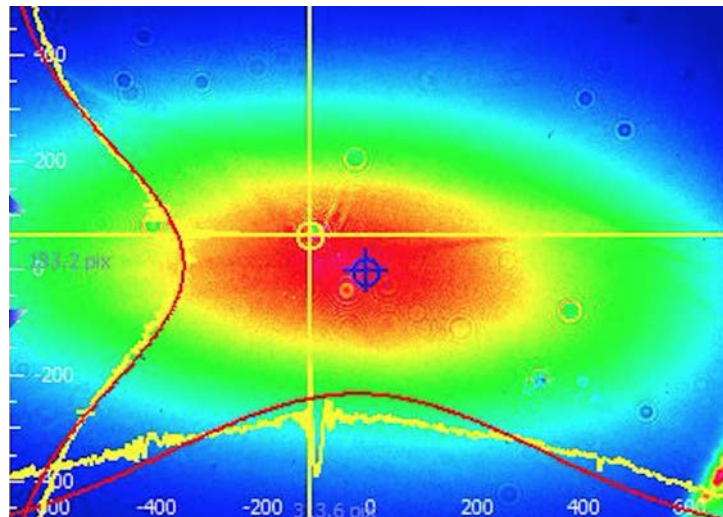
Figure 3.10: The beam profiler is 20 mm away from the output facet. The red Gaussian fitting is close to the actual intensity. However, along the x-axis, there are a few defects.

Base on the Littrow configuration, the compact 461 nm diode laser design is shown in Figure 3.11.
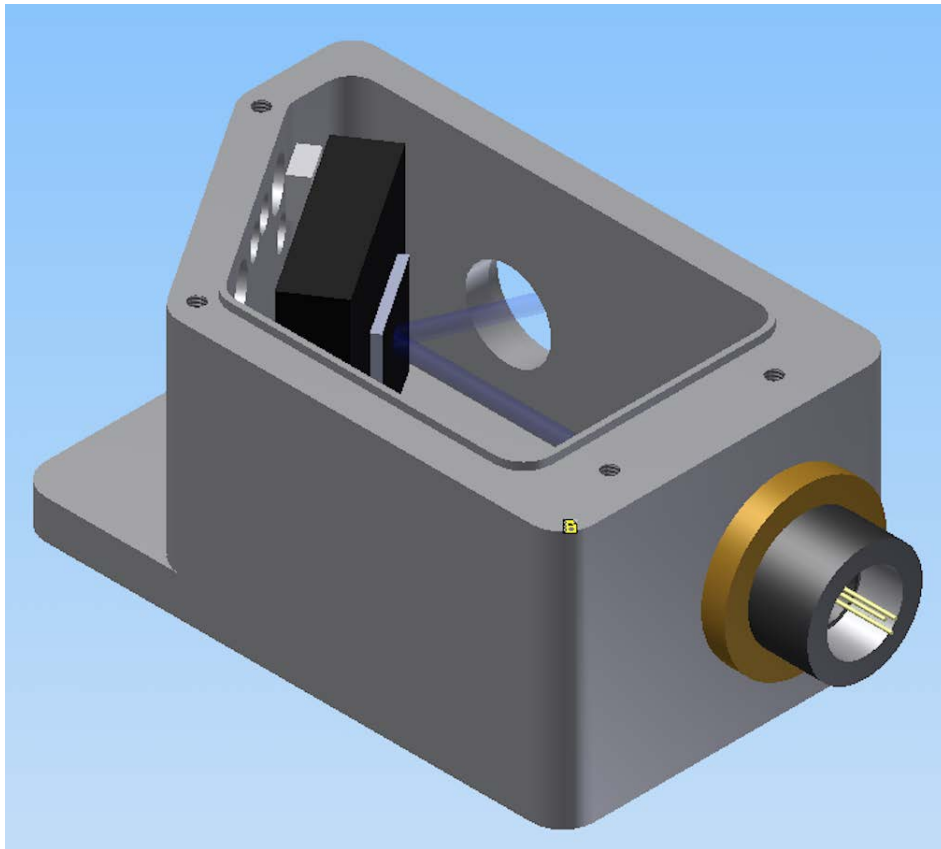
Figure 3.11: 461 nm diode laser structure: The centers of the diode, the grating and the output hold are in the same plane which is 16 mm above the housing bottom. The dimensions of the housing is 70 mm × 43 mm × 35 mm.

A blue laser diode high voltage controller connects the diode through an electrostatic discharge (ESD) protection and strain relief cable. A $f = 4.00$mm aspheric lens collimates the divergent beam from the diode. After the collimation, the length of the major axis and minor axis of the elliptical beam is 1.7 mm and 0.56 mm, respectively. Both the lens and diode are fitted in a modified laser diode collimation tube. The external surface of the tube is machined with a screw thread which matches the one in the laser housing. There is a 12.8 mm×12.8 mm×5 mm indentation on the plate for mounting the visible reflective holographic grating. The indentation saves the space and set the grating position. Its groove density is 2400 line/mm. Using
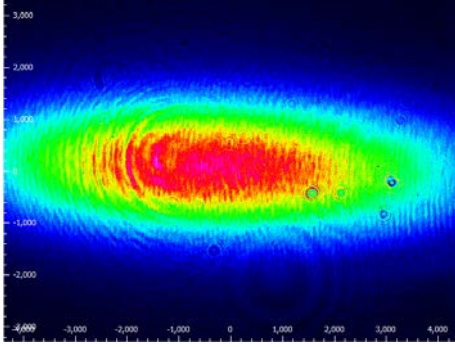
(a) The cross section is elliptical with some fringes on it.
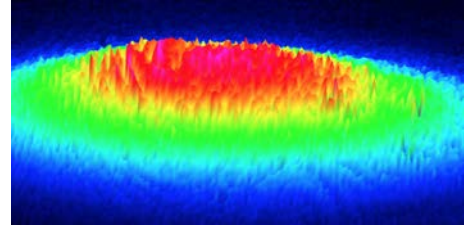
(b) The intensity image shows a lot of peaks.

Figure 3.12: Beam profile of the light from the 461 nm Diode

Equation 3.1, the incident angle is calculated as 33.6°. Two fine thread screws(150 μm/turn) from Radient Dyes(Model 2, 170 TPI) adjust the tilting and rotation of the grating. Between the grating plate and the rotation screw head is a PZT for fine frequency fine tuning. A 10 kOhm thermistor is embedded into the laser housing, 5 mm away from the diode. The peltier elements controlling the temperature is mounted under the bottom of the laser housing. The housing made by aluminum is designed as the center of the laser beam is 20 mm above the baseplate. The housing has a cover to isolate the temperature and avoid air fluctuation.

The 0th order of the diffraction is the output of the diode laser. The beam profile is checked by the CCD camera beam profiler. The imperfection is amplified after the grating. The laser output is clearly not an ideal gaussian beam and show many additional side features(Figure 3.12). The reason might be the 461 nm wavelength is just on the edge of the laser diode operation wavelength.

3.2 Laser distribution module

In the mobile clock projects, the optomechanical components for lab based experiments do not fulfill the requirements of miniaturization and robustness. A range of customized optics and optical component mounts are used to transmit the laser. Fig-

ure 3.13 shows a selection of the homemade components design. These components was designed for the drop tower experiment at ZARM, Bremen, Germany [77] and their function and robustness for mobile setups had been verified in the experiment.
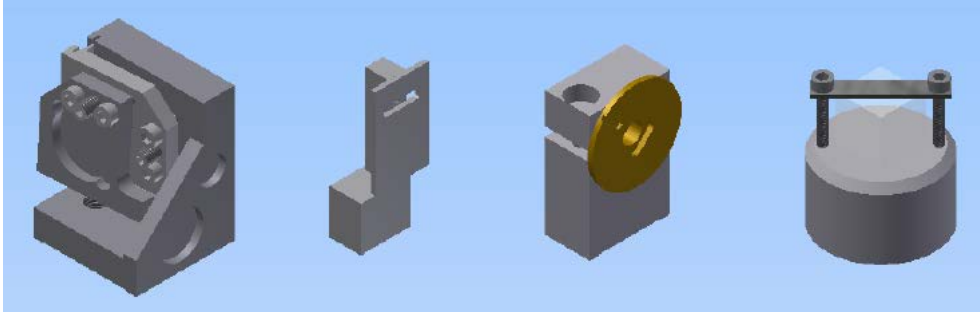
Figure 3.13: From left to right, they are mirror mount, beam block, wave plate mount, and PBS mount.All these optics mount have locking mechanism to reduce the vibration-caused misalignment.

The mounts are designed to make the optics center to be the same 20 mm. It saves the adjustment on the horizontal level when the components for one function module are screwed to the same baseplate.

In the clock laboratory, we had performed three strontium optical lattice clock project. The first one is named as transportable strontium lattice clock. The second one is an Europe project call Space Optical Clock II(SOC II). The third one is the miniaturized strontium lattice clock. In each experiment, there is one essential module is the laser distribution module used to deliver the laser power. I had operated four mobile laser distribution modules and three of them are designed and built by me. These laser distribution modules will be introduced in this section.

3.2.1 Laser distribution module in transportable strontium clock

In the transportable setup(Figure 4.1), the six beam MOT configuration is used. One beam from the frequency doubling module is split into six beams and coupled

into six single mode PM fibers. For detuning the laser, an AOM is also included in the module to shift the laser frequency. Figure 3.14 is the top view of the laser distribution module.
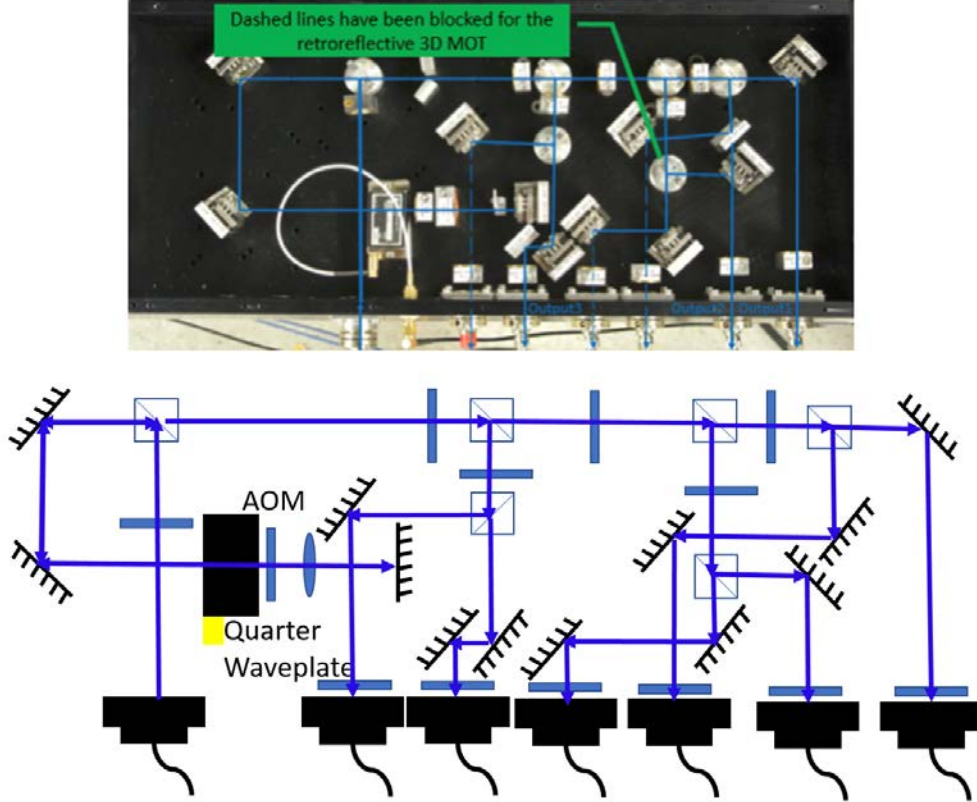
Figure 3.14: Laser distribution module in the transportable strontium clock: Shifting 461 nm laser frequency, splitting one beam to three/six beam and coupling the laser to the fibers are finished in this module.

The input laser firstly goes through a double-pass AOM setup which is made of a polarized beam splitter(PBS) with AR coating covering 461 nm, an 80 MHz AOM, a quarter waveplate, a $f = 40$ mm lens, a beam block and a mirror. The focus of the lens is on the mirror eliminating the shift of the beam while tuning the AOM. The double-pass AOM cause 40% power loss of the blue laser and distort the beam profile. However the frequency change on the AOM will not change the direction of the laser beam which benefit the detuning optimization. The frequency shifted laser then is split into six beams which are coupled into the fibers. Before each fiber coupler, there is a half-wave plate to adjust the polarization of the laser to match

the polarization axis of the SMPM fiber. Due to the distortion from the AOM and the optics surfaces, the coupling efficiency of the fiber couplers is 55% - 65%. The total power efficiency of the distribution module is ≈36%. With a total input power of 50 mW, ≈4 mW is distributed to each beam.

3.2.2 Laser distribution module in SOCII

For the space optical clock II(SOC II) project, I built a distribution module dealing with blue laser used in each step of the whole clock experiment. Figure 3.15 shows the CAD(computer-aided design) of the module.
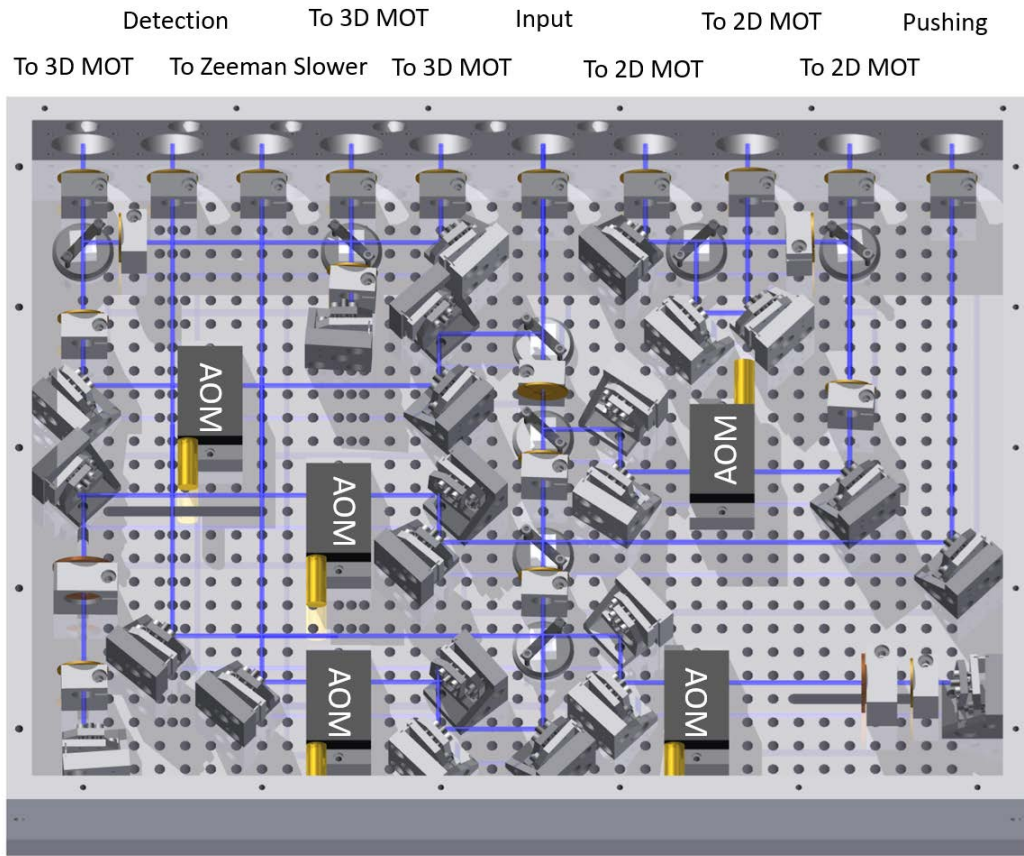
Figure 3.15: The power getting into the module is split into five branches for different purposes. From the top to bottom, they are MOT laser, 2D MOT laser, 2D MOT pushing laser, Probe laser, Zeeman slower laser.

The 200 mW input blue laser is split into five branches with half-wave plates and PBS. The first branch goes through a single pass 110MHz AOM with 85% efficiency.

Then it splits into three beams to the fiber couplers. The second branch has the same splitting scheme. For the first two branches, the efficiency of the six couplers are slightly different, varying between 58% to 65%. With half-wave plates and PBSs, the difference of the laser power out of the six fibers are controlled to less than 2%. In the actual experiment, the second branch was cancelled to save power and the retro-reflected 3D MOT with three fibers was used. A double-pass 200 MHz AOM shifts the frequency of the third branch which is going to be in the permanent magnet Zeeman slower [78] for pre-cooling the hot atoms. The fourth branch is the probe laser for detecting the atoms. Its frequency is shifted by a double-pass 80 MHz AOM. The fifth branch is sent to the frequency stabilization system (FSS) [79] and used to lock the 461 nm laser.

3.2.3   Single board blue MOT

As described in the experiment chapter, we started the modified pyramid MOT vacuum chamber with a MOT demonstrator which exhibits the new technologies applied to the miniaturized strontium clock project. The diode laser, the frequency shift, locking and power delivery are integrated into one baseplate. The top view of the plate with the vacuum chamber is shown in Figure 3.16.

The 30 mW elliptical beam(see Figure 3.12) from the diode laser is transformed to a nearly circular beam by a anamorphic prism pairs. The customized isolator after the prism pair has an efficiency of ≈85% and suppress the instability on the diode laser by isolating the reflection. Then the beam splits into two beam by a PBS – one beam with 6 mW to the 40 MHz AOM for shifting the laser frequency 45 MHz higher than the atomic transition, the other one with 20 mW to a fiber which delivers the power as well as shapes the beam to a perfect Gaussian beam.
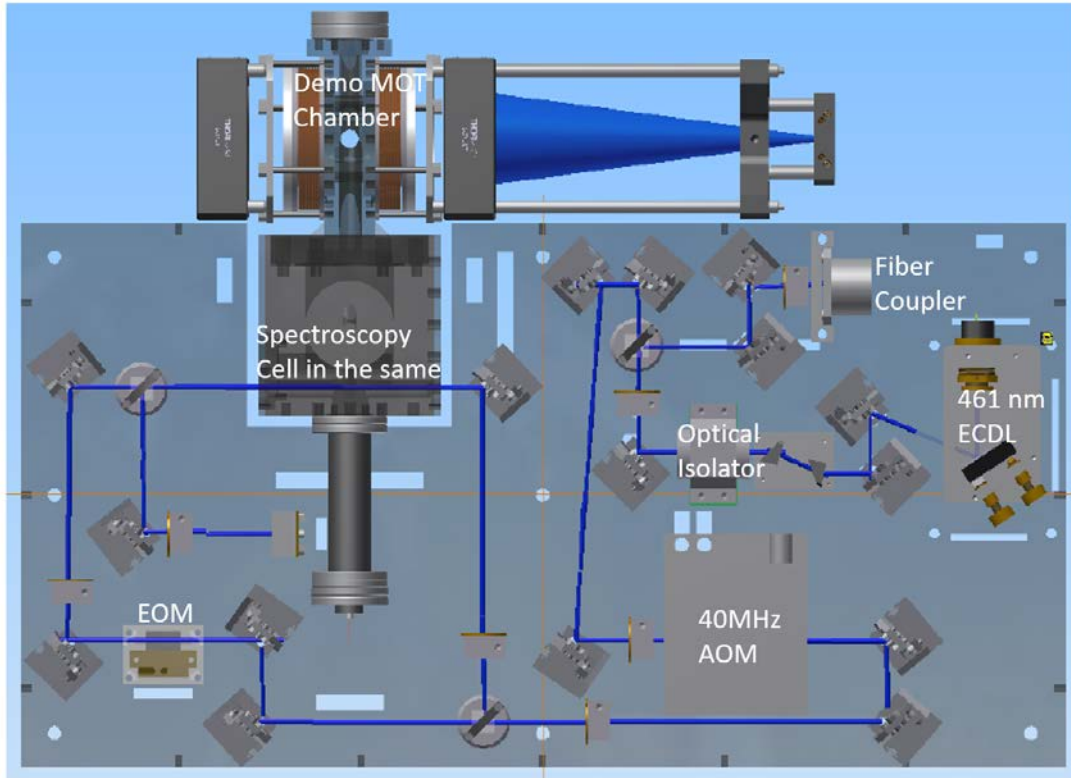
Figure 3.16: The plate integrates all the necessary components for making a blue MOT.

The $+1^{st}$ of the diffraction taking 5.6 mW is used to lock the laser with the inbuilt spectroscopy (see Figure 4.15). The modulation transfer (MT) spectroscopy locking scheme [80] is used to lock the laser. With 60% efficiency of the fiber coupling, 12 mW is delivered as the cooling laser.

3.2.4 One fiber for blue and red MOT

After the realization of the first stage cooling - blue MOT as the 461 nm cooling laser is blue, we pushed the experiment to the second stage cooing - red MOT since the cooling laser's color is red. The 461 nm laser and the 689 nm laser needs to be overlapped to transfer the atoms from the blue MOT to the red MOT. One solution is a dichroic mirror combining the blue and red laser beam after the two fibers and before the light going into the chamber. This method has been verified in the SOC

II project(see Figure 4.3). Another way that simplifies the mechanical structure is to transmit the two lasers in one fiber. This tactic requires a laser combination setup on a baseplate. Figure 3.17 is the design of the light path for overlapping the blue and red laser. For the red MOT, the 461 nm laser is from SOLSTIS ECD-X made by M Squared Lasers. Its output power reaches 400 mW at 461 nm.
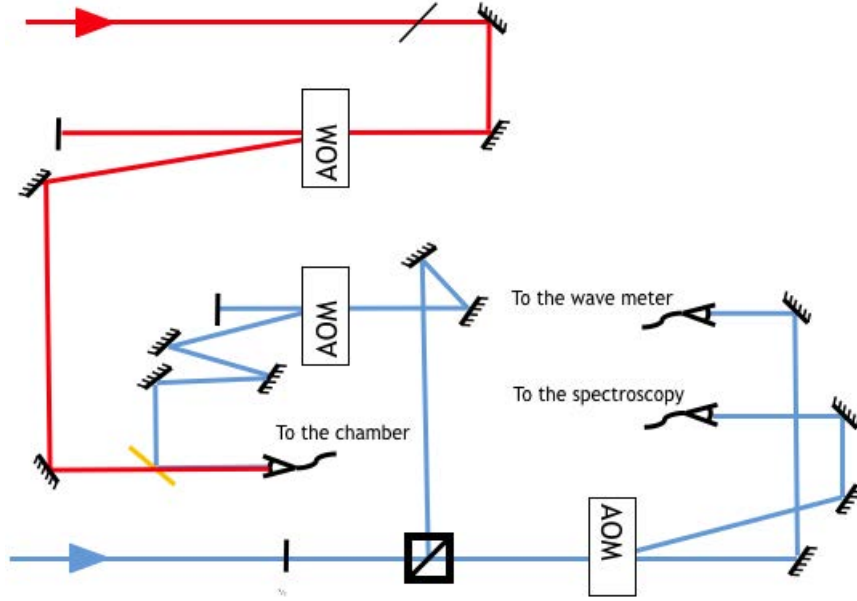
Figure 3.17: The light path for overlapping the blue and red cooling laser

A PBS splits the total ≈400 mW blue laser into two branches. The 370 mW branch goes through a single pass 80 MHz AOM with 314 mW in the 1st diffraction order. Apart from shifting the frequency, this AOM has another function as switching off the light by applying a off-resonance frequency. The switching off time is less than 1 μs. Through a fiber coupler with 50% efficiency for blue light, 160 mW blue laser is coupled to the fiber as the cooling laser. The 50 mW branch is split to two beams by a 110 MHz AOM. The 0th order with 5 mW is coupled to a fiber for monitor the frequency. The 1st order carrying 20 mW is for locking the 461 nm laser.

On the red laser part, 80 mW 689 nm light is sent to a 80 MHz AOM. The 1st order is coupled to the fiber for cooling. As the cooling laser fiber coupler has a working spectral range of 400 - 600 nm, there is only 13 mW coupled into the fiber. However,

for the single beam telescope configuration, this power is high enough for the red MOT. All the three AOMs are from, two with operation frequency of 80 MHz and the last at 110 MHz) and their operating wavelength of 415 - 900 nm and 440 - 850 nm covers the lasers for the two cooling stages.

Chapter 4

From Six-beam MOT to Single-beam MOT

As a standard laser cooling and trapping technique, the traditional six-beam MOT configuration is now used in most cold atoms laboratories that require large numbers of cold, trapped atoms [72, 81–83]. In this design, each circularly polarized laser beam requires multiple optical and optomechanical components. This inherently restricts the minimum volume of the atomics package, and the large number of components can lead to a fragility that is undesirable for systems that are expected to be transported from one place to another on a regular basis. As an alternative to the six-beam MOT design for compact experiments, different configurations of single-beam MOTs have been proposed and tested in many cold atoms groups. For example, pyramidal and conical hollow mirror MOTs [84], surface-patterned chips [85] and modified pyramidal funnel type MOTs [86] have been used in rubidium experiments. At the University of Birmingham, the first generation of the transportable strontium clock project used the standard six-beam MOT configuration. However, despite successes in shrinking the vacuum chamber, the overall volume was limited by the long MOT beam telescopes. In the current version of the transportable clock, the bulky six-beam MOT configuration has been replaced with a compact single-beam modified pyramidal funnel MOT.

In this chapter, I will present details regarding the development of transportable strontium clocks at the University of Birmingham and the latest results from our portable system.

4.1 Conventional six-beam MOT in Birmingham

The transportable strontium clock project at the University of Birmingham began in 2008, aiming to build a mobile neutral strontium lattice clock. The system features a 2D-MOT pre-cooling chamber connected to a 3D-MOT scientific chamber via a differential pumping stage [12]. A dispenser emits a high flux(10^{13} atoms/s level) of hot strontium atoms directly into the 2D-MOT chamber. The atoms in the 2D-MOT chamber are then pre-cooled by a 461 nm blue laser which is 2.5 MHz red-detuned from the $^1S_0 \rightarrow {}^1P_1$ transition. Instead of using the coils, permanent magnets generate the cylindrical quadrupole field with the gradient of tens of G/cm. To achieve the zero magnetic field along the symmetry axis, spacing of the magnets are adjustable. The pre-cooled atomic flux from the 2D-MOT to the 3D-MOT is higher than 10^8 atoms/s. Once in the 3D MOT chamber, the atoms are cooled and trapped by the 25 MHz red-detuned 461 nm laser with the help of a pair of water-cooled anti-Helmholtz coils which generates a magnetic field gradient of 50 G/cm. In this setup, 4×10^5 atoms are captured with a long lifetime of 5.5 s. Figure 4.1 shows the 750 mm long vacuum chamber and peripheral components mounted on a 1500 mm $\times$ 900 mm $\times$ 58 mm optical breadboard.

As introduced in Chapter 3, the 461 nm cooling laser are delivered to the vacuum chamber by fibers. There are six telescopes for expanding the beam to the designed intensity of 5 mW/cm^2. Three of those 20 cm long telescopes mounted around the chamber can be seen in Figure 4.1. The six-beam MOT configuration enables the
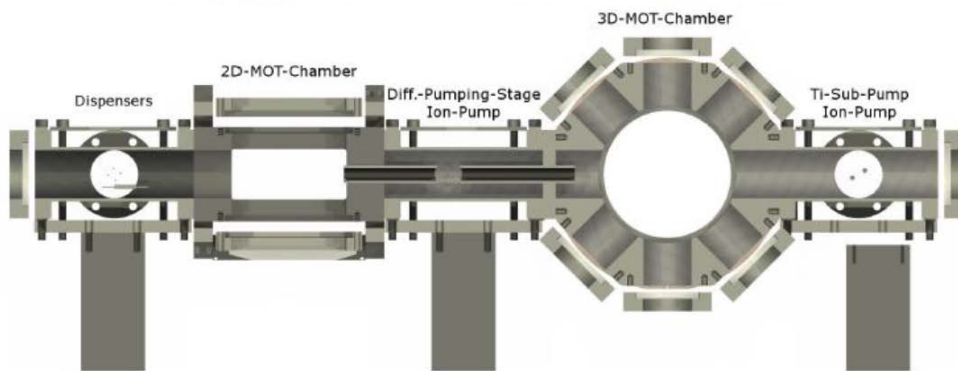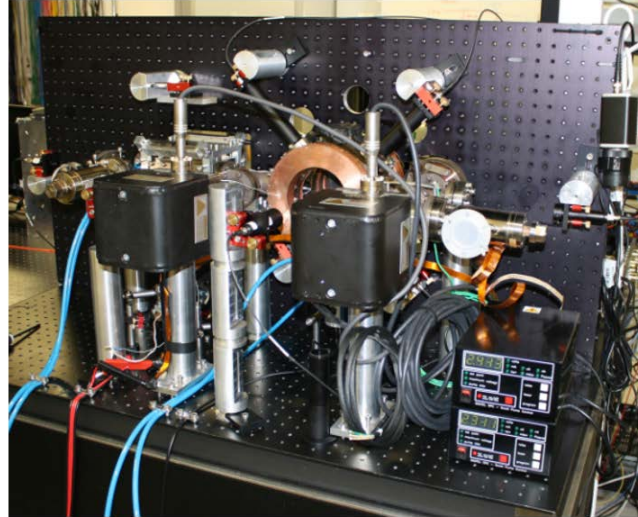
Figure 4.1: Transportable strontium lattice clock: The picture above is the vacuum system with optical fibers around it. There are three fibers observable in the picture. The CAD design shows the basic structure of the vacuum system. Aiming at a transportable clock, the whole setup are mounted on a optical table.

simple alignment of the incident MOT beams. However, the single mode PM fibers as well as the optics mounts are sensitive to vibration, humidity, temperature change and other environmental effects. Realignment and re-optimization procedures must be carried out weekly. To be a real mobile strontium clock, the apparatus must be more robust and immune to the instabilities.

Another small experiment chamber for testing SrO which could be made as a laser induced strontium source was built in 2014. Beam expansion telescopes were mounted onto the small chamber and the design was changed to incorporate a three beam retro-reflected 3D MOT (Figure 4.2). By switching to a three beam MOT configuration, three fibers were eliminated from the setup, and the unibody design matches

the requirements for mobility. Progression towards a portable design is also demonstrated by using an experiment chamber with similar dimensions to the telescopes. However, the enclosed lens tubes used in the telescopes limit the ability to align the MOT beams.
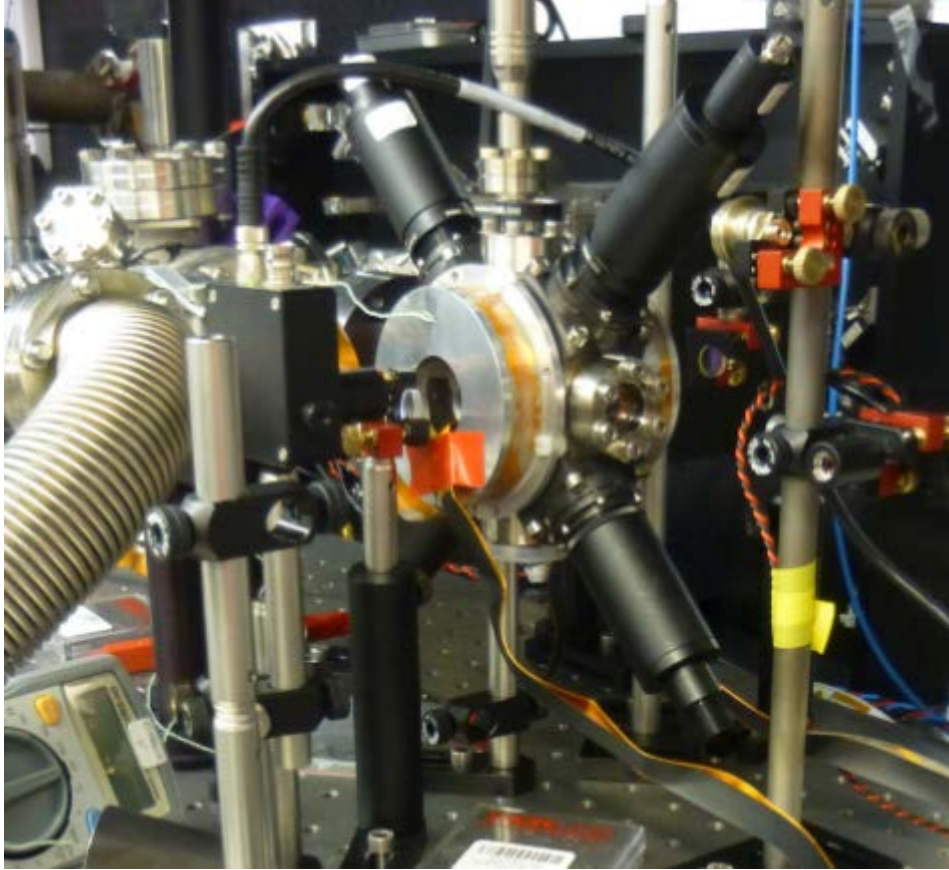
Figure 4.2: Unibody design of a retro-reflected 3D MOT. All the telescopes are attached to the chamber. This compact design has two advantages: for generating the same magnetic field gradient, the water-cooled anti-Helmholtz coil is replaced by the air-cooled one; the telescope mounts which may introduce misalignment in the transportable clock project are eliminated.

The disadvantage of the six-beam MOT can also be found in the beginning of the SOC II project (Figure 4.3). To build a strontium optical lattice clock which meets the requirements for space readiness, the vacuum apparatus as well as the optomechanics are supposed to be compact and robust. As a result, the scientific chamber is made by titanium with a diameter of 5 cm. Fibers for delivering the lasers are connected to the cage systems which are mounted on the chamber. However, when

all the fibers are connected, each arm of the cage system is more than 10 cm long. Any adjustment to the cage systems or the fibers requires significant care and effort to avoid misalignment. Too many components attached to the chamber would also increase the stress on the connections of the vacuum chamber. To simplify the operation and maintaining, SOC II abandoned the six-beam MOT configuration and applied the retro-reflected MOT design.
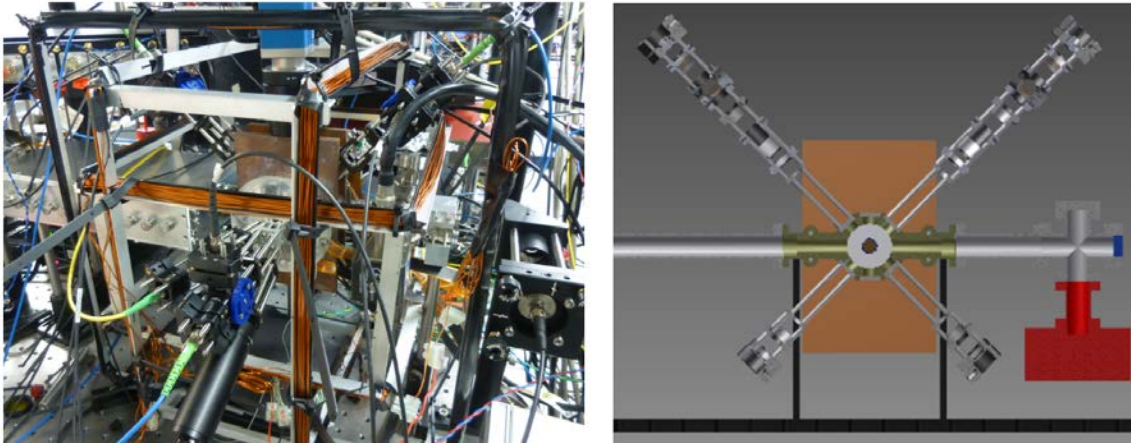
Figure 4.3: Space Optical Clock II setup near the scientific chamber end: The peripheral components completely cover the MOT chamber in the left picture. The right CAD design shows the relative length of the telescopes and the small chamber. The vacuum system does not take too much volume and the telescopes are mounted on the chamber to increase the robustness, but the six-beam/three-beam structure limits the simplicity of the system.

4.2   Single beam MOT

Just like a laboratory-based strontium optical lattice clock, the miniaturized version will utilize the same experimental procedure – cooling and trapping hot strontium atoms, loading the cold atoms into an optical lattice, and finally interrogating the atoms with an ultra stable clock laser. However, each component of the experimental apparatus, such as the laser systems, electronics and vacuum system, must shrink compared to their counterparts in typical laboratory-based experiments. This

section will present the newly developed techniques for a miniaturized single-beam strontium MOT.

The idea for using a single-beam MOT to trap strontium atoms was inspired by K. I. Lee's work on single-beam atom traps for rubidium [84]. A schematic diagram of the modified single-beam pyramid MOT is shown in Figure 4.4. A PM fiber provides a linearly polarized cooling light, which passes through a quarter-wave plate to convert it into the circularly polarized light required for the MOT. A telescope enlarge the laser beam to cover the four metal coated right angle prism mirrors mounted inside the experiment chamber. The central part of the beam which is called the central beam, passes all the way through the experiment chamber, then through a quarter-wave plate and is retro-reflected back by a mirror, passing through the quarter-wave plate a second time on the return path to reverse the orientation of the circular polarization. A part of the outer edges of the laser beam which are called side beams, are reflected by the 45° metallic mirrors, simultaneously reversing their polarizations. This results in three pairs of counter-propagating laser beams pointing to the center of the chamber. The atoms in the center of the chamber "see" a conventional six-beam MOT.

For loading MOTs, larger diameter trapping beams mean larger capture volumes and therefore a larger number of atoms loaded into the MOT. This requirement is in direct contrast with the goal of clock miniaturization, so a balance must be achieved between MOT capture volume and clock setup volume.

4.2.1 Vacuum Chamber

Four primary factors affect the chamber design – the in-chamber mirrors, vacuum sealing, heating due to the anti-Helmholtz coils and vacuum pressure maintenance.
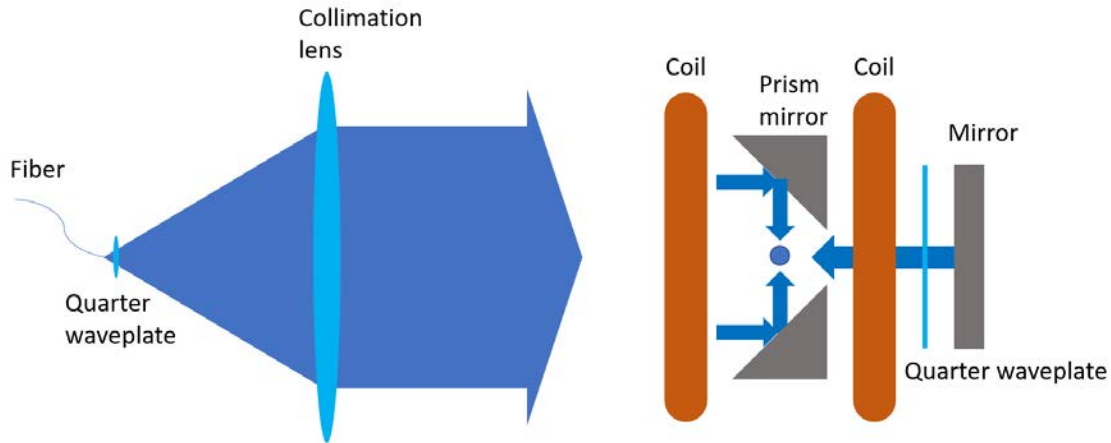
Figure 4.4: The basic structure of the single-beam MOT. There is only one expanded laser beam outside the vacuum chamber. The metallic mirrors are placed inside the vacuum.

After choosing the proper mirrors, the minimum diameter and thickness of the chamber can be set. Commercial viewports welded into ConFlat(CF) flanges can increase the thickness of the chamber by up to 50%. To keep the same magnetic field gradient, the increased thickness will result in a larger current which would either degrade the vacuum or introduce extra frequency shift to the clock transitions. The small chamber would limit the pumping speed of the pumps which would increase the collision between the hot and cold atoms.

Metallic Mirror: Indicated in [84], aluminum coated mirrors reversed the circular polarization of the incident laser with less than 1% contamination of the polarization. 461 nm and 689 nm are the two cooling transition wavelengths used in strontium MOTs. For this reason, due to their higher reflectance at the wavelengths of interest, silver coated mirrors are more suitable than their aluminum or gold counterparts.

In rubidium experiments, it is possible to load large MOTs directly without pre-cooling mechanism. Strontium's vapor pressure at room temperature, however, is below 10^{-14} mbar, prohibiting the direct loading of a large strontium MOT from the background vapor. The strontium atom source must be heated to provide a

high flux of atoms directing towards the trapping region. As a result, the typical pyramid MOT [87] design used in rubidium experiments must be modified to allow atoms access to enter of the experiment chamber. In addition to this constraint, the repumping laser, the lattice laser and clock laser also require sufficient optical access. To accommodate these requirements, the mirror layout chosen for the design can be seen in Figure 4.5. The inclined silver-coated planes of the four right angle prism mirrors face the center of the chamber, while the uncoated bottom surfaces of the prism mirrors lie in the same plane. The square hole in the center of the four mirrors allows access for the third pair of orthogonal MOT beams (the central beam). Two of the gaps along the strontium atoms' propagation direction allow the atoms to enter the chamber, and the other two gaps provide optical access for either a camera or the lattice and clock lasers.
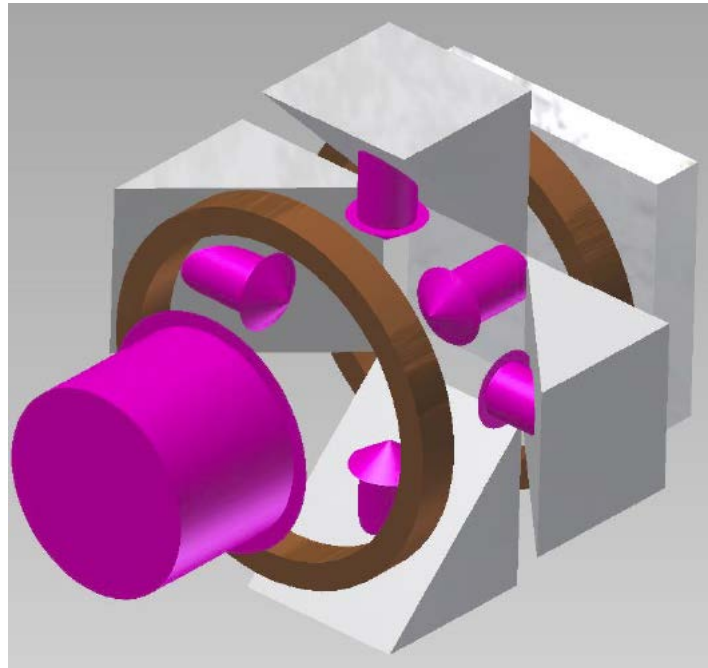
Figure 4.5: The four mirrors sit in the same plane to keep the power balance of the four side laser beams. The red arrows represent the overlap of lasers for the first and second cooling stages. In experiment, the inner diameter of the coil is larger than the prism mirrors. The four side metallic mirrors revert the polarization, so the quarter waveplate for the four side beams are not necessary.

As preliminary research towards a miniature strontium lattice clock, we developed

a strontium MOT technology demonstrator with the aim of realizing a blue MOT with a 30 mW 461 nm diode laser. Based on previous research conducted within our lab on transportable strontium clocks [12], with 1 cm MOT beam diameters and a total beam intensity of 1.05 mW/cm^2, a small blue MOT with $\sim$2500 atoms is visible in the chamber, even without pre-cooling and no repumping lasers present. Knowing that a blue MOT is possible with these MOT beam diameters, we use commercial right angle prism mirrors in the single-beam MOT chamber of the technology demonstrator. The base length of each prism mirror is $L = 12.5$ mm, which means the effective MOT beam dimensions will be 12.5 mm × 12.5 mm. Once the four prism mirrors have been arranged in the configuration shown in Figure 4.5, the thickness and diameter of the mirror assembly is 12.5 mm and 39.5 mm, respectively. These two values set the minimum limit of the chamber volume.

Indium Seals and Viewports: To obtain maximum optical access, the diameter of the viewport should be greater than the diameter of the four mirrors configuration. To withstand one atmosphere pressure differentials, as the window diameter increases so should the window thickness. Vacuum companies sell standard viewports mounted in CF flanges, which use copper gaskets to create a vacuum seal for ultrahigh vacuum. For example, one commercial viewport mounted in a flange has a clear aperture of 68.3 mm and glass thickness of 6.4 mm, while the flange thickness is 17.3 mm. Using these standard flanges will increase the distance between the pair of anti-Helmholtz coils, resulting in a lower magnetic field gradient. On the other hand, customized viewports from a vacuum company would be very expensive, especially for the non-standard, small-sized viewports used in our chamber. To reach the ultra high vacuum regime (10^{-9} mbar to 10^{-11} mbar) for the clock experiment, an alternative approach is to use indium to seal the bare viewport directly to the chamber. The indium sealing process is explained in Figure 4.6. The 1.0 mm diame-

| (a) Cleaning | (b) Twisting | (c) Tightening |
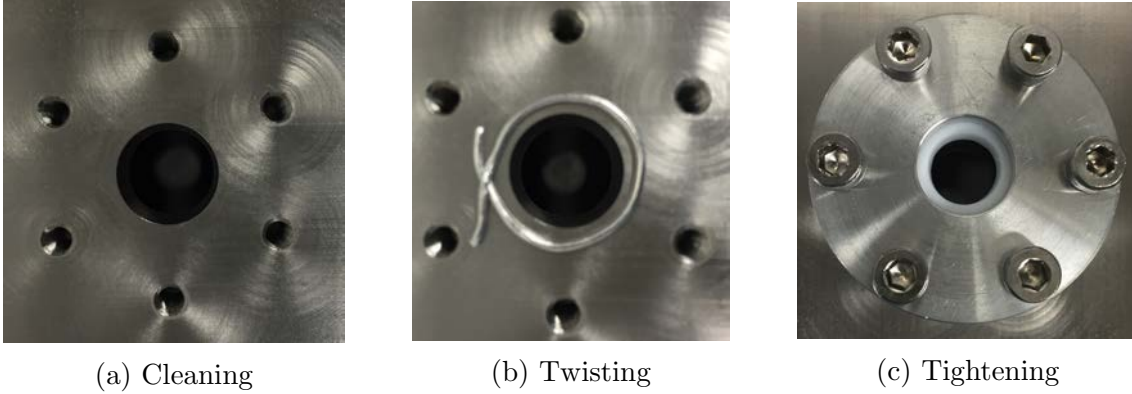
Figure 4.6: a. Cleaning the polished metal surface and the indium wire with propanol; b. Making the indium into a ring with a diameter greater than the diameter of the aperture and smaller than the diameter of the glass window; Twisting the two ends of the indium wire; Placing the glass window, Teflon spacer, the aluminum ring and the bolts; c. Tightening the bolts in opposition; Releasing the bolts in opposition after the designed vacuum achieved.

ter indium wire is used to seal the large viewports, and the 0.5 mm diameter indium wire is used to seal the smaller viewports. The tightening torque is determined by the glass window.

To reduce power loss at the optical surfaces, anti-reflection (AR) coatings are necessary for the viewports. Strontium clocks typically use lasers spanning from the visible to the near-infrared spectrum. The specific coating applied to each window will depend on which laser wavelengths will be passing through that window. Both the 461 nm blue and 689 nm red cooling lasers share the same optical path, so the broadband AR coating for the windows these beams passing through covers the range 400 nm – 700 nm. The 813 nm lattice laser and 698 nm clock laser also share the same optical path, so the AR coating for these windows covers the visible and near-infrared spectrum. The VIS 0° and VIS-NIR coatings from Edmund Optics satisfy these requirements. Table 4.1 lists the reflectance properties at different wavelengths for these AR coatings.

The VIS 0° coated viewport (Edmund Optics, 47-523) for the cooling lasers has a 50 mm diameter and a 4 mm thickness. The total thickness of the optics required

Coating Name	r_{461}	r_{679}	r_{707}	r_{813}	r_{698}
VIS 0°	<0.2%	<0.2%	<0.4%	n/a	<0.3%
VIS-NIR	<0.5%	<1%	<1%	<0.5%	<1%

Table 4.1: Reflectance of different AR coatings. r_x denotes the reflectance at x nm.

for the MOT chamber, including two viewports, the prism mirrors, is 20.5 mm. To avoid increasing the thickness of the chamber any further, the viewports (Edmund Optics, 45-659) along the edge of the chamber used for the lattice laser have a 15 mm diameter with the VIS-NIR coating.

Anti-Helmholtz coils: The blue MOT transition in strontium has a broad 32 MHz linewidth, which helps the cooling efficiency. However, the wide linewidth requires a high magnetic field gradient of $\approx$50 G/cm, as stated in the Chapter 2. This high gradient requires high current and high power. For mobile applications, especially the strontium clocks in space, the high power consumption of such coils is unacceptable. For example, in the SOC II experiment (see Figure 4.3), two sets of 160 mm × 100 mm × 2 mm double-layer copper plates act as heat sinks to cool the coils, hence decreasing the power transmission to the vacuum chamber. An alternative solution is to mount the coils inside the chamber near the MOT region. This solution is not ideal, however, because the coils would block the optical access in the chamber and may possibly heat the atoms in the MOT. Instead, outside-the-chamber coils is going to be optimized to balance the gradient, power consumption and coil size in our miniaturized strontium clock design.

From the Biot-Savart law, we can deduce the formula for the magnetic field B of the anti-Helmholtz coils along their common axis when the coils have the same number of turns n and current I:

$$B = \frac{\mu_0}{2}nIR_c^2\left(\frac{1}{R_c^2 + (x - d/2)^{3/2}} - \frac{1}{R_c^2 + (x + d/2)^{3/2}}\right), \tag{4.1}$$

where μ_0 is the permeability of free space, R_c is the coil radius, x is the position along the coil axis and d is the distance between the coils. The derivative of the magnetic field provides the field gradient, a critical property for laser cooling.

From Pouillet's law, the power consumption P in one coil for the above magnetic field is

$$P = I^2 \frac{2\pi \rho R_c n}{\pi (d_w/2)^2}, \tag{4.2}$$

where ρ is the wire resistivity and d_w is the diameter of the wire cross section. Because the cooling lasers passing through the center of the coils, the minimum inner coil diameter must be larger than the diameter of the prism mirror assembly inside the chamber. For a unibody design, the coil mounts attach directly to the experiment chamber. To avoid misalignment of the MOT beams in the mobile clock, the laser expansion telescope system should also attach directly to the experiment chamber. This stipulation limits the maximum possible external coil diameter. Taking these parameters into consideration, the coil-mount assembly design can be seen in Figure 4.7. The gap on the mount allows one end of the coil wire to pass through the mount for electrical contact to a current supply. The semicircular gaps on the mount are used to fix the coil mount to the chamber.

Table 4.2 shows the optimal coil parameters for the first stage cooling procedure in our experiment. The inner and outer coil diameters are 41 mm and 61 mm, respectively.

I	n	d_w	∂B	d	R_c	P
2.5 A	110	0.9 mm	35 G/cm	36.5 mm	51 mm	3.1 W

Table 4.2: Optimized coil parameters according to Equation 4.1 and 4.2.

For designing the chamber, one important issue is the achievable pumping speed to control the vacuum environment inside the chamber. Two different chamber designs
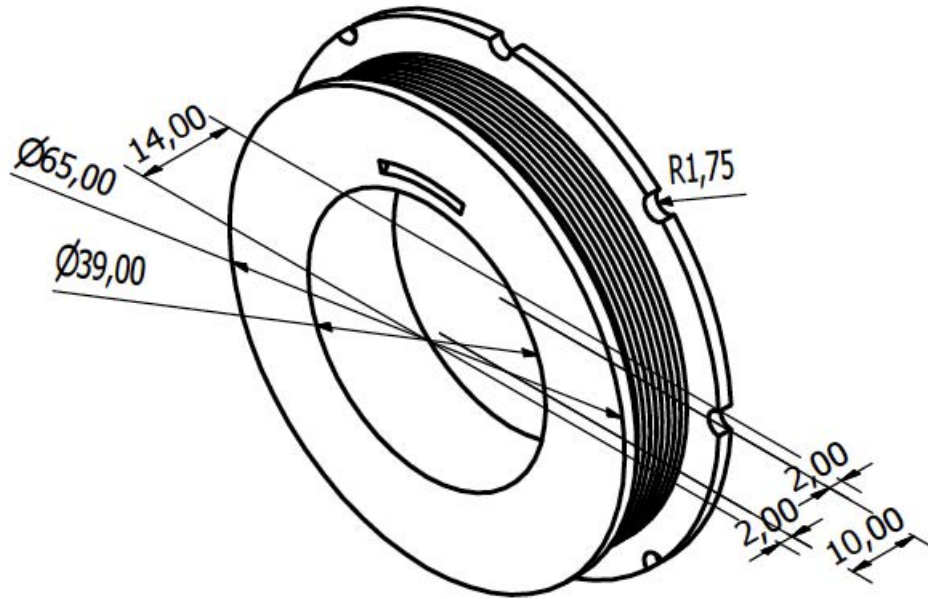
Figure 4.7: The parameters of the coil mount is specified in the picture in unit mm.

were manufactured and tested in the laboratory. The main difference between the two designs is the pumping mechanism – the first version uses a 2 L/s ion pump, while the second version connects to a hybrid getter-ion pump which has a pumping speed of 100 L/s for H_2. To minimize the weight of the vacuum system while still maintaining its material strength, titanium is used to manufacture the chamber.

Chamber I: As seen in Figure 4.8, there are two main sections of the vacuum chamber. The cubic section contains three standard DN16CF flanged ports used to house an ion pump, a valve and a strontium dispenser. Connected to vacuum electrical feedthroughs to apply a current, the dispenser has a slit at the end to emit strontium atoms into the chamber. The hot atoms from the dispenser enter the MOT trapping region through a borehole 28 mm long and 8 mm in diameter. No differential pumping stage was used in this design for two reasons. First, the ion pump is mounted near the dispenser which emits the atoms directly to the MOT chamber. With a differential pumping stage between the two section, the pressure in the MOT chamber could not be reduced by the ion pump; Second, the 8

60

mm diameter borehole allows the option of holding strontium oxide powder, which requires a large optical access to be used as a source of strontium vapor (see Chapter 6).
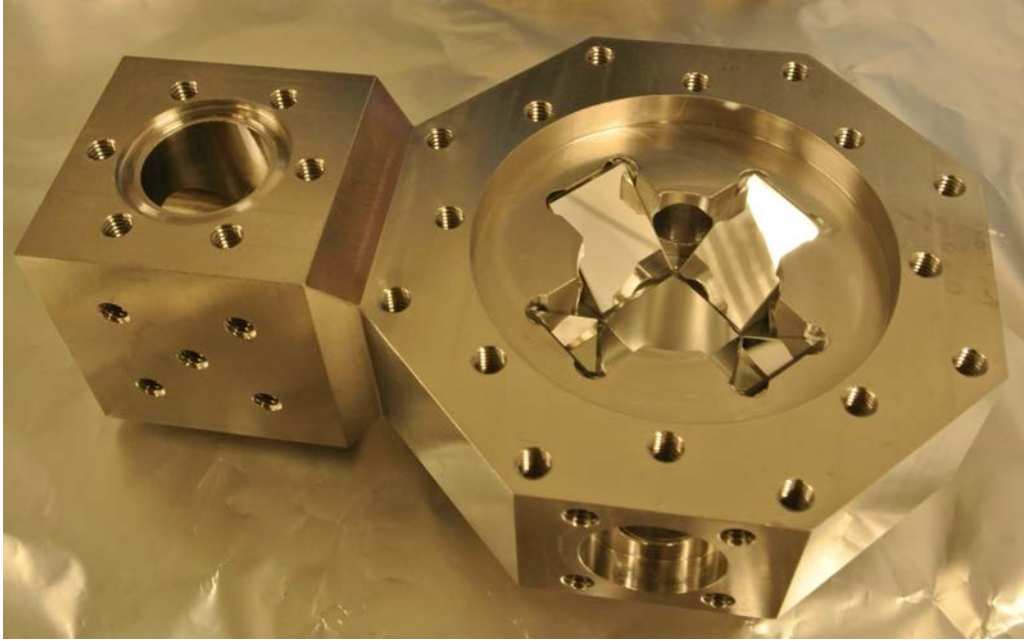
Figure 4.8: The octagonal chamber holds the prism mirrors for trapping the atoms. A valve, a dispenser and a ion pump with pumping speed of 2 L/s are connected to the vacuum setup through the cubic chamber. Some strontium oxide sample is held in the borehole which connects the octagonal chamber and the cubic chamber.

The octagonal section of the vacuum chamber, referred to as the scientific chamber, has a thickness of 22.5 mm. The four prism mirrors are positioned in the four square through-holes in the chamber. These four gaps, each with three walls, have the same 12.5 mm width as the metallic mirrors. The square gaps are actually manufactured to be 0.1 mm wider than the width of the prism mirrors to allow for the possibility of thermal expansion. The rounded corners in the square gaps are filled with vacuum glue to secure the prism mirrors. The two 51 mm diameter recessed round surfaces are polished for indium sealing. Another advantage of the flat surface means that by pressing another flat surface firmly against it, the bottoms of the mirrors can be guaranteed to lie in the same plane. There are also three side viewports on the octagon which are sealed with 15 mm diameter windows. The two windows

orthogonal to the direction of the atomic beam are suitable for the optical lattice laser or a camera, and the window in the line of sight of the atomic beam can be used for the repumper lasers or for a strontium oxide 'emission' laser.

Up to the first stage cooling step, a visible blue MOT, was realized in Chamber I. However, the ion pump could not provide sufficient pumping speed to support the MOT operation. During operation of each strontium source, strontium oxide and the dispenser, the pressure reading on the ion pump controller reaches 10^{-7} to 10^{-6} mbar. At these background pressures, the excessive density of hot background atoms collide too frequently with cooled atoms, heating them up and preventing the formation of a cold MOT. Successful MOT loading only occurred when a turbo pump assisted the ion pump to reduce the pressure in the vacuum chamber. Despite the insufficient pumping speed in Chamber I, it still trapped strontium for the first time a single-beam MOT configuration, using both the dispenser and strontium oxide sources. Based on the lessons learned when designing and testing Chamber I, the main improvement for Chamber II is to increase the achievable pumping speed.

Chamber II: In a vacuum chamber with a complicated inner structure, the nominal pumping speed cannot actually be achieved because the intermediate piping systems limit the actual pumping speed. A correction between the nominal pumping speed S and the effective pumping speed S_{eff} of the area of interest is given by

$$\frac{1}{S_{eff}} = \frac{1}{S} + \frac{1}{C},\tag{4.3}$$

where C is the total conductance of the vacuum chamber. Calculating the total conductance of the vacuum components is similar to the calculation of resistance in

62
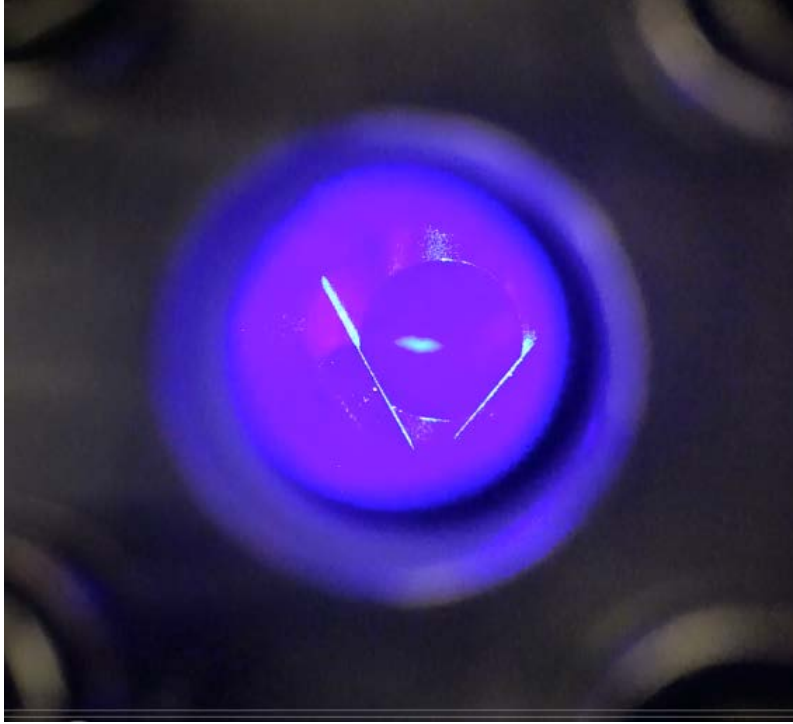
Figure 4.9: With high power homemade laser and turbo pump connected to the vacuum setup. A blue MOT has been realized. Although the 2 L/s ion pump design failed, we have proved that single-beam MOT configuration for strontium could be realized.

electrical circuits. For series connections, the total conductance C_s is

$$\frac{1}{C_s} = \frac{1}{C_1} + \frac{1}{C_2} + \frac{1}{C_2} \cdots , \tag{4.4}$$

where C_1, C_2, C_3 are the conductance of the series sub-systems. Parallel connections have a total conductance of

$$C_p = C_1' + C_2' + C_3' \cdots , \tag{4.5}$$

where C_1', C_2', C_3' are the conductance of the parallel sub-systems. The Knudsen equation [88] gives the most precise approximation of the conductance of air in a straight pipe at room temperature (20°). Due to the ultra high vacuum condition in our experiment, the atom flow enters the molecular regime, which occurs when

$d \cdot \overline{p} < 10^{-2}$ mbar(d is the diameter of the tube, $\overline{p}$ is the volume flow rate at unit pressure). The Knudsen equation can be simplified as

$$C_m = 12.1 \cdot \frac{d^3}{l} \qquad (4.6)$$

where C_m is the pipe conductance in units of L/s, d is the pipe diameter in units of cm and l is the length of the pipe in units of cm.

Using Equation 4.3–4.6 to calculate the effective pumping speed of the small 2 L/s ion pump used in Chamber I gives an actual pumping speed of 1 L/s. Considering the low pumping speed, Chamber II utilizes an enlarged effective pipe diameter as well as a small hybrid getter-ion pump with a higher nominal pumping speed than the small ion pump.

Figure 4.10 shows a CAD drawing of Chamber II, a modified version of Chamber I (see Figure 4.8). The design of the octagonal section of both chambers remains mostly the same. Chamber II, however, has a hollow structure inside the chamber frame. Since the coils limit the thickness of the chamber, the effective diameter of the "pipes" in the chamber could only be increased by drilling more holes in the chamber. The cubic section of Chamber I with three DN16CF flanged ports was replaced in Chamber II by a DN35CF flange. As seen from the calculation of the effective pumping speed in Chamber I, one solution to improve the pressure in the chamber is to use a pump with a higher nominal pumping speed. Pumps with higher pumping speeds typically require larger flanges in order to not restrict the actual pumping speed. By increasing the size to a DN35CF standard flange, a stronger physical connection can be made between the chamber and other vacuum components, which is also beneficial for a mobile system.

The calculated conductance in Chamber II is 7 L/s, 7 times the achievable pumping
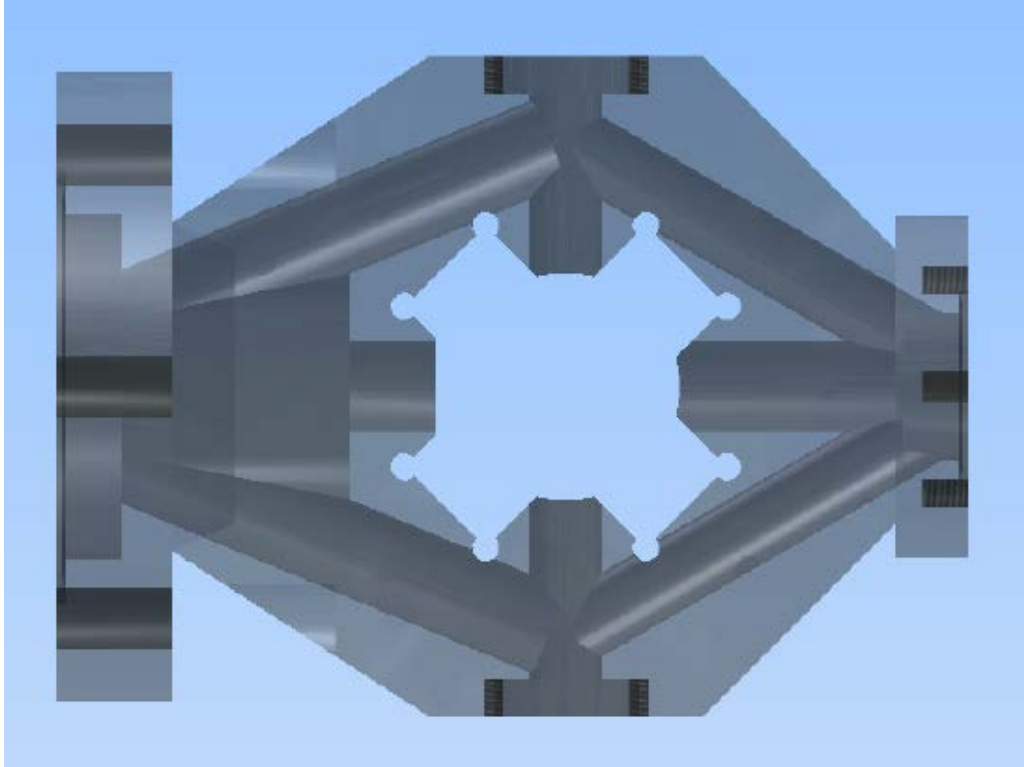
Figure 4.10: The transparent effect shows the inner structure of the Chamber II.

speed in Chamber I. The 2 L/s ion pump used in Chamber I is not capable of reaching the maximum possible pumping speed achievable in Chamber II, so Chamber II uses a compact NEXTorr D 100-5 getter-ion pump from SAES (see Figure 4.11). This pump features a nominal pumping speed of 100 L/s for H_2, and the ion pump alone is capable of pumping O_2 at 5 L/s. The pumping speed for strontium is not specified on the pump's data sheet. During operation of the experiment, with 5×10^6 atoms in the blue MOT, the NEXTorr pump indicates a pressure of 1.5×10^{-9} mbar. As mentioned previously in this chapter, the ideal vaccum pressure for the operation of a strontium clock is in the range of 10^{-10} mbar to 10^{-11} mbar.

Figure 4.12 shows the assembled vacuum system for Chamber II without coils. The vacuum is maintained by the getter pump when the ion pump is not operational. The robustness of the vacuum system was verified when the system was transported from Birmingham to London in a van via motorway, with a layer of cotton insulation

Figure 4.11: This picture shows the structure of the NEXTorr pump. Before mounting, the getter pump is vacuum sealed. Before using the pump, the getter material needs to be activated.

as the only vibration isolation mechanism. The pressure drifted between 1.1×10^{-10} mbar and 1.3×10^{-10} mbar. For general movement, the vacuum system

4.2.2 Integrated strontium reference cell

Figure 4.12 shows a 80 mm $\times$ 80 mm $\times$ 110 mm titanium cuboid as the supporting center of Chamber II. All other chamber modules attach to this supporting cuboid. As the heaviest individual component, the pump mounts to the bottom of the cuboid. The rough pumping valve connects to the lower part of the cuboid to avoid blocking the beam paths or interfering with the electrical connections for the dispenser. The centers of the scientific chamber and the dispenser lie on a common horizontal axis. Another module, a spectroscopy cell for locking the 461 nm laser to an atomic reference, is embedded directly within the cuboid structure. The 80 mm long spectroscopy cell, which has a diameter of 8 mm, is the smallest and most integrated locking reference for a 461 nm laser developed at the University of Birmingham. The evolution of laser frequency stabilization designs demonstrates the progression towards compact and mobile systems.
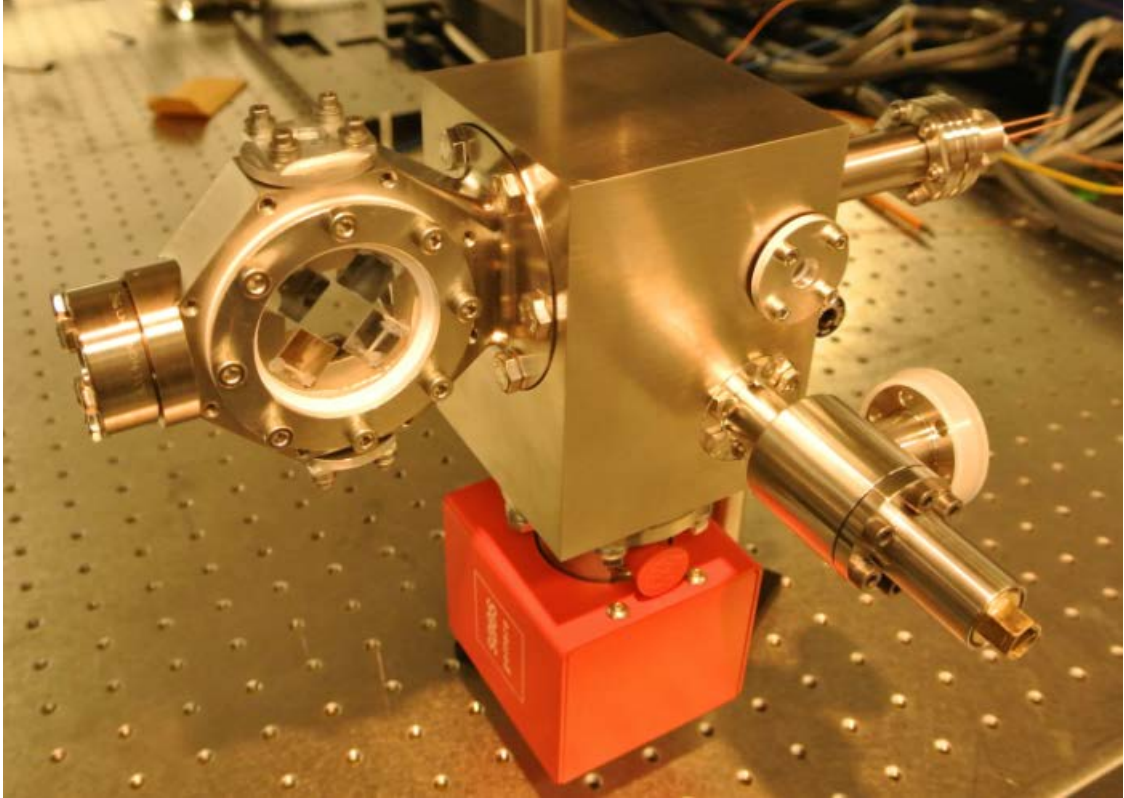
Figure 4.12: Chamber II with every vacuum components connected. Both the chamber and the cubic housing for the NEXTorr pump are made by titanium.

Spectroscopy cell with an oven: Unlike rubidium, which has a vapor pressure around 10^{-7} mbar at room temperature, strontium must be heated to 550 K to reach a similar vapor pressure. In our lab, the strontium were heated to more than 600 K. The first strontium spectroscopy cell built in Birmingham, along with the schematics for the laser locking electronics, can be seen in Figure 4.13. It contains an oven with 2 g of strontium at the bottom of a glass vacuum chamber. Heating wires around the oven connect to an external power supply via a vacuum electrical feedthrough. The two arms of the cell, which have AR coated windows at the ends, each have a length of 15 cm. After several years of operation, the glass tube above the oven has been coated completely with strontium, while the viewports are almost free from coating.

Using this strontium spectroscopy cell, the 461 nm laser is locked to the $^1S_0 - ^1P_1$ transition using frequency modulation (FM) spectroscopy [89]. Prior to entering the
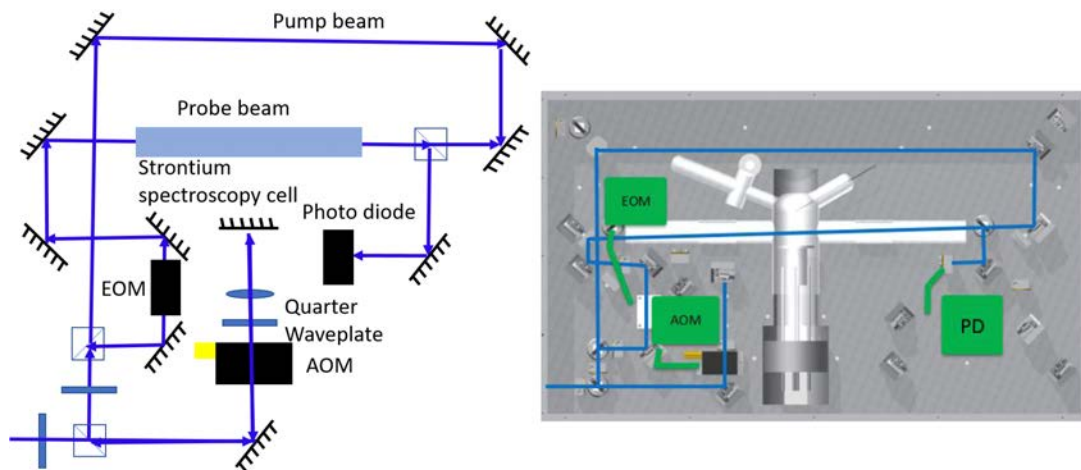
Figure 4.13: The oven based spectroscopy cell is mounted in a aluminum box as the modular design. The AOM in the module is used to shift the frequency of the blue laser. The schematic graph shows the locking scheme of the frequency modulation locking.

spectroscopy cell, the 461 nm laser is split into a pump beam and a probe beam by a polarizing beam splitter (PBS) cube. The pump beam enters the spectroscopy cell directly through one of the viewports. Before entering the cell from the other viewport, the probe beam is modulated by an electro optical modulator (EOM) at a frequency of 43 MHz generated by a local oscillator. This pure phase modulation adds frequency side-bands to the probe laser's spectrum. The solid strontium is heated to a vapor in the oven and the atomic beam is emitted in an orthogonal direction to the counter propagating pump and probe beams. The signal observed on the photo diode is mixed with the local oscillator's signal. The amplified error signal can then be sent to a proportional integral derivative(PID) [90] controller to provide feedback to the 461 nm laser frequency controller, the fast signal to the laser current while the slower one to the piezo. Figure 4.14 shows a typical error signal obtained from the FM spectroscopy locking module. Within the Doppler valley signal, the $^1S_0 - ^1P_1$ transition for the ^{88}Sr and ^{86}Sr isotopes can be seen in the error signal.

As shown in Figure 4.13, there is an electrode in the top right arm of the glass
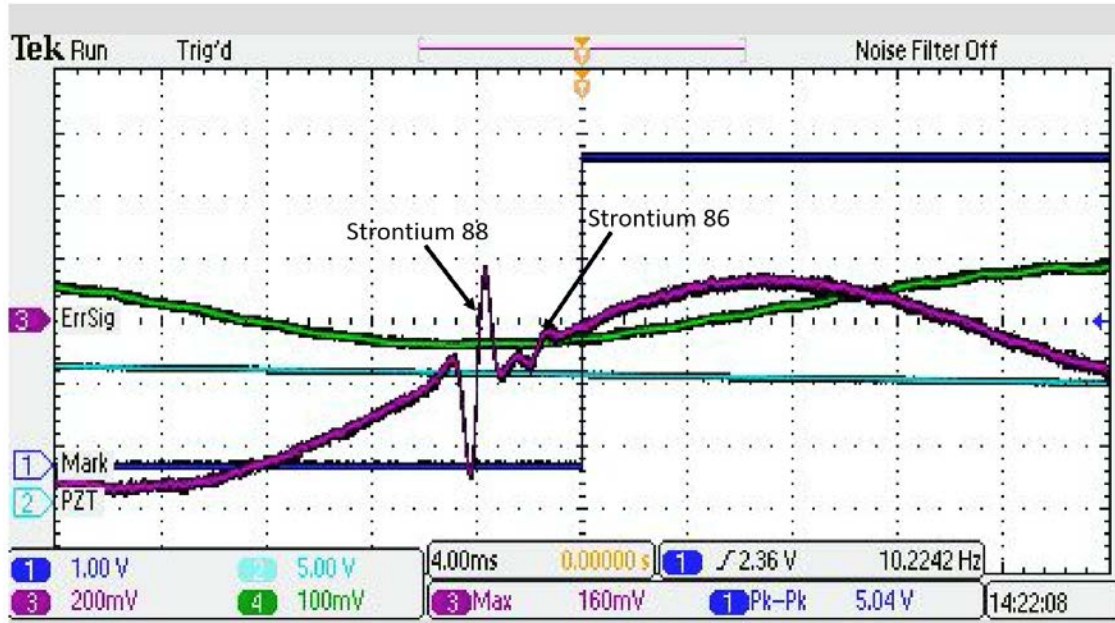
Figure 4.14: The green line the the photo diode signal which shows the Doppler valley. The purple line is the error signal. Both [88]Sr and [86]Sr are visible.

chamber. In addition, a second electrode is connected to the electrical feedthrough near the oven. Upon vaporizing the strontium and applying 300 V across the two electrodes, the discharged strontium atoms can populate the ^3P_j states. This extra step allows us to also lock the 679 nm and 707 nm repumping lasers to the $^3P_{0,2} - ^3S_1$(see Figure 2.4) transitions using the same FM locking scheme.

Whether heating or charging the atoms, the module requires high power ($>$20 W) and high voltage ($\approx$300 V). This feature is not ideal for a mobile system. In addition, a fragile cell made of glass is a disadvantage in the moving process. Following the design in [91], the spectroscopy module was replaced with a second generation design.

Spectroscopy cell with dispenser: For the second generation spectroscopy cell, seen in Figure 4.15, the glass tube from the first generation module is replaced with a steel 4-way cross and the glued viewports have been changed to CF flanged viewports sealed with copper gaskets. Inside the 4-way cross, a dispenser replaces the oven, and the divergence of the atomic beam is limited by two pieces of aluminium

69

foil mounted on either side of the dispenser. By not attaching a glass tube to an aluminum box as in Figure 4.13, the 4-way cross version allows more freedom for mounting and transportation.
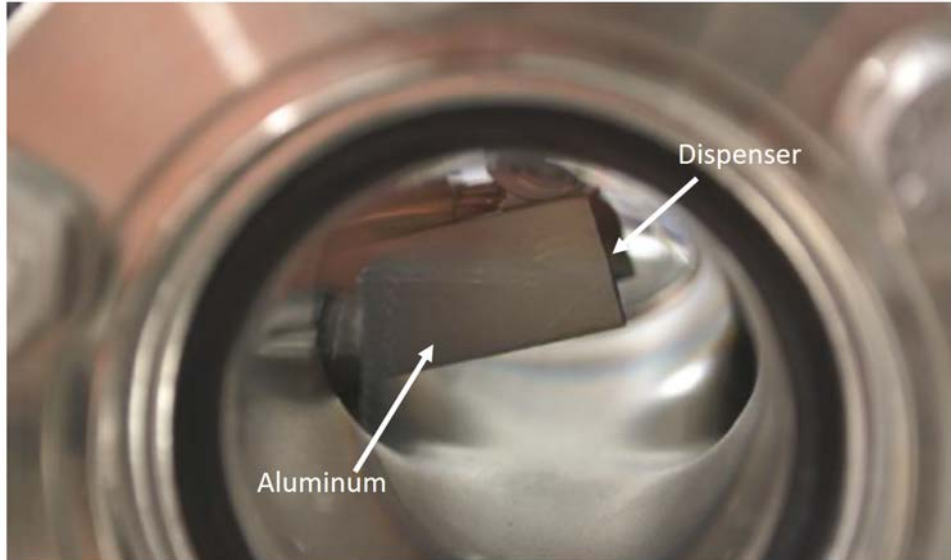
Figure 4.15: A dispenser in 4-way cross replaced the oven in a glass tube. The dispenser is covered by an aluminum foil to prevent the coating on the viewports.

Along with a new spectroscopy module design, a new locking scheme, modulation transfer (MT) spectroscopy [80], is employed. In this method, the "pump" beam is modulated by an EOM instead of the probe beam. In the FM locking scheme, the error signal includes a Doppler valley signal which can transfer laser intensity fluctuations into laser frequency fluctuations. In MT locking, however, the Doppler valley signal is not present on the error signal, and the lock is less susceptible to laser intensity fluctuations. Figure 4.16 shows a typical error signal from our MT locking scheme.

The dispenser requires a power supply with >13 A current to emit strontium atoms. Also, comparing the 4-way cross in the spectroscopy module to the atom chamber in Figure 4.12, they have a similar size. Therefore, further reduction of the size and power consumption of the laser locking module would greatly benefit the progression towards a mobile strontium clock.
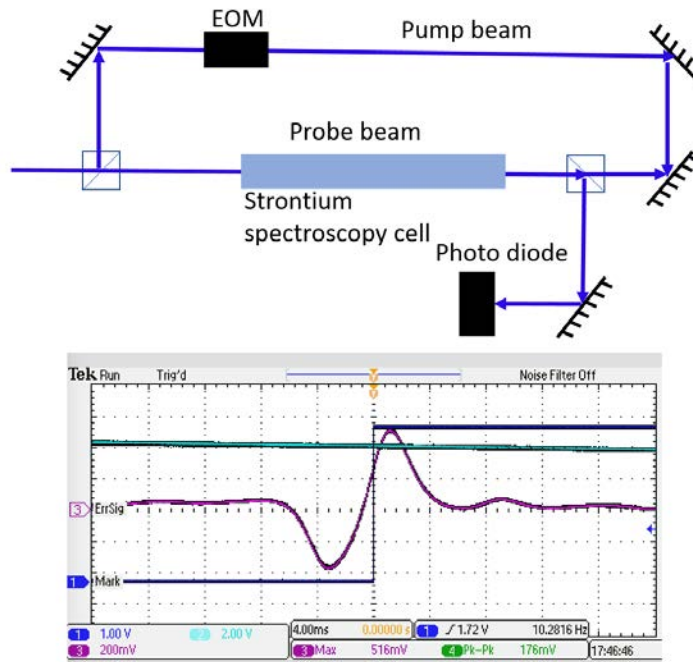
Figure 4.16: The purple line is the error signal. The center feature is from ^{88}Sr and the signal from ^{86}Sr can just be seen.

Integrated spectroscopy cell: Less than 5% of the strontium atoms emitted by the dispenser are actually cooled and captured by the MOT. Integrating the spectroscopy cell into the mobile clock experiment chamber in the path of the atomic beam between the dispenser and the MOT region provides an efficient solution to make use of the excess atoms that would not be loaded into the MOT.

As mentioned at the beginning of this section, Chamber II has a spectroscopy cell in the cuboid next to the dispenser. The interior structure of the cell, including the dispenser, can be seen in Figure 4.17. Hot atoms emitted from the dispenser first pass through the spectroscopy cell before reaching the MOT capture region. Some of these atoms that pass through the spectroscopy cell are resonant with the blue pump and probe lasers. In between the getter-ion pump and the spectroscopy cell is a 4 mm diameter hole, which lies along the same axis as the center of the dispenser and the center of the MOT chamber. This hole helps to collimate the atomic beam and prevents some excess atoms from entering the MOT chamber

71

where they would otherwise increase the background pressure. The same MT locking scheme as described previously is used in the integrated spectroscopy cell.
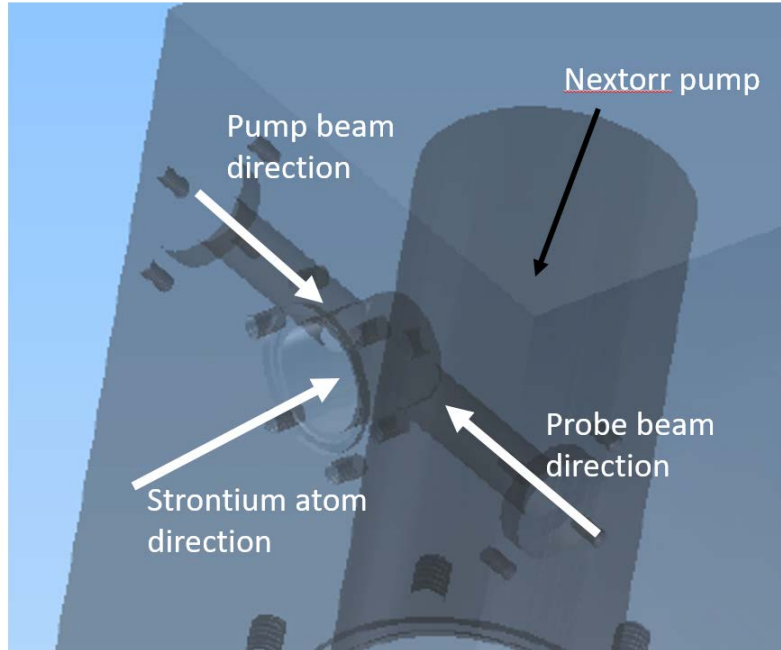
Figure 4.17: The CAD design in transparent effect shows the inner structure where the atoms and the locking lasers meet. The atoms used for locking the 461 nm laser is on the way to the 3D MOT chamber.

Other possible laser locking solutions also exist for the mobile chamber. For example, stabilizing lasers to Fabry-Pérot (FP) cavities is a widely used technique in spectroscopy experiments [92]. For a mobile atomic clock, stabilizing lasers to short FP cavities would further reduce the size of the system, especially in situations where locking to an atomic transition is difficult or inconvenient. In fact, developing miniaturized optically contacted FP cavities is an ongoing project within our lab. However, for the demo-MOT design, locking the 461 nm laser directly to the $^1S_0 - {}^1P_1$ transition using a spectroscopy cell is a simpler and cheaper option, especially when it allows us to use a single dispenser for both MOT loading and laser locking.

4.2.3 Single beam telescope

The single-beam MOT structure depicted in Figure 4.4 is composed of two parts – the prism mirrors inside the chamber and the single beam cooling laser. With a final design for the vacuum chamber, the desired diameter of the laser beam can be determined. Because it is bulky and inconvenient to work with laser beams with the same diameter as the chamber window, the initial beam diameter before entering the chamber is much smaller than the window. We use a telescope to expand the beam and then collimate it at the correct diameter just before it enters the chamber. Using a free-space laser beam for the cooling laser has the advantage of low power loss during propagation throughout the MOT chamber. The mirrors in the beam path have >99% reflectivity, while the coupling efficiency of a single mode polarization-maintaining (PM) optical fiber for blue a laser is <70%. In a compact laser system, the 30% power loss could prove critical. On the other hand, the beam's spatial mode profile coming from a fiber is nearly a perfect Gaussian mode, while the profile coming directly from a laser diode is typically much less ideal. If the beam profile has defects, it can lead to intensity imbalances between the four cooling beams reflected off the prism mirrors (see Figure 4.5 and Chapter 6).

Gaussian beam from a fiber: Mathematically, the electric field amplitude of a Gaussian beam is

$$E(r, z) = E_0 \frac{\omega_0}{\omega(z)} \exp\left(\frac{-r^2}{\omega^2(z)}\right) \exp\left(-ikz - ik\frac{r^2}{2R(z)} + i\psi(z)\right), \qquad (4.7)$$

where r is the radial distance from the center axis of the beam, z is the axial distance from the beam's waist, E_0 is the electric field amplitude at the origin, ω_0 is the waist radius, $\omega(z) = \omega_0\sqrt{1 + \frac{z\lambda}{\pi\omega_0^2}}$ is the radius at z, λ is the wavelength of the

laser, $R(z) = z \left[1 + \left(\frac{\pi \omega_0^2}{z\lambda} \right)^2 \right]$ is the beam's wavefront radius of curvature at z and $\psi(z)$ is the Gouy phase at z. The corresponding intensity distribution is given by

$$I(r,z) = \frac{|E(r,z)|^2}{2\eta} = I_0 \left(\frac{\omega_0}{\omega(z)} \right)^2 \exp \left(\frac{-2r^2}{\omega^2(z)} \right), \tag{4.8}$$

where η is the characteristic impedance of the medium ($\eta \approx 376.7\,\Omega$ in vacuum) and I_0 is the intensity at the origin. For a circular Gaussian beam, the intensity at cylindrical coordinate (r,z) can be expressed as

$$P(r,z) = P_0 \left(1 - \exp \left(\frac{-2r^2}{\omega^2(z)} \right) \right), \tag{4.9}$$

where $P_0 = \frac{1}{2}\pi \omega_0^2 I_0$ is the total power in the Gaussian beam. Approximately, the central part of the cooling laser which is not reflected by the metallic mirrors has the power of $P(r = 0.5L, z)$, where L is the width of the prism mirror. While those four beams reflected by the prism mirrors, the side beams, each has a power around $\frac{1}{8}(P(r = 1.5L, z) - P(r = 0.5L, z))$.

As evident from Equations 4.7–4.9, the spatial intensity distribution of a laser at any point in space is fixed by the beam waist and laser wavelength. For a single mode PM fiber, the diameter of the beam at the exit port of the fiber is called the mode field diameter (MFD) of the fiber, which is determined by the numerical aperture (NA) of the fiber:

$$MFD = \frac{2\lambda}{0.82\pi NA}. \tag{4.10}$$

Table 4.3 lists the parameters for two possible fiber options to be used in the mobile clock experiment. By knowing the laser wavelength and the NA of the fiber, the laser intensity distribution can be calculated. Figure 4.18 shows a power comparison between the central cooling beam and one of the four side cooling beams along the

z axis. 10 mW of 461 nm laser light exits the output end of a fiber, which is located at $z = 0$. The central part of the beam entering the MOT chamber contains almost all the power for small values of z, while the side beams have almost no power. As the Gaussian beam diverges along the z axis, the power ratio between the central beam and each side beam approaches 1. At $z = 150$ mm, the central beam power drops to about 3 mW, and the side beam power rises to approximately 1 mW. Between $z = 150$ mm and $z = 200$ mm, the side beam power remains relatively constant, while the central beam power continues to decrease. Beyond $z = 200$ mm, both beams continue to decrease towards 0 mW. This behavior suggests that the collimation lens should be placed somewhere between $z = 150$ mm and $z = 200$ mm to maximize the power in the side beams while simultaneously keeping the power ratio between the central and side beams below 3:1.

Fiber	Wavelength (nm)	NA	Polarization Extinction Ratio (dB)
1	460-550	0.12	>23
2	460-700	0.11	>18

Table 4.3: Fiber 1 is PMC-460Si-3.0-NA012-3-APC-200-P from Schäfter+Kirchhoff. Fiber 2 is P3-488PM-FC-2 from Thorlabs. Fiber 1 is featured for its higher polarization extinction ratio. Fiber 2 is used due to its wider wavelength range when the red MOT cooling beam is required in addition to the blue MOT cooling beam.

Beam telescope: As the laser propagation simulation suggests in Figure 4.18, the side beam power reaches a maximum between 150 mm and 200 mm away from the fiber end. To make the system as compact as possible, we choose a collimation lens with focal length 150 mm. The schematic drawing of the telescope optics is shown in Figure 4.19. There is a quarter-wave plate between the lens and the fiber adapter to convert the linearly polarized light into circularly polarized light.

MOT beam mask: The vacuum chamber, which is made of titanium, scatters any stray laser light incident on its surface. If the full Gaussian MOT beam enters the chamber, reflections off the asymmetrical inner walls of the chamber will introduce
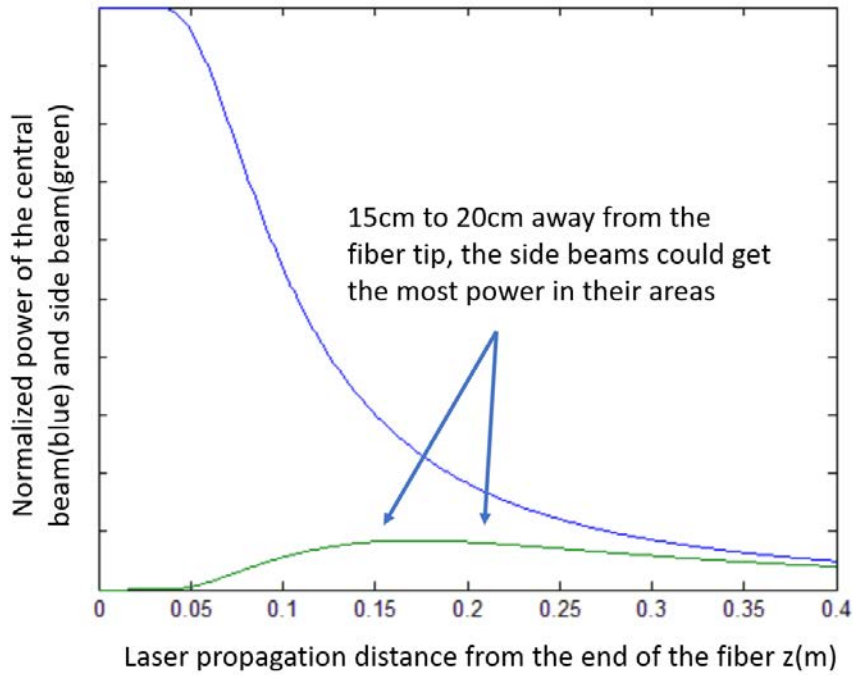
Figure 4.18: Along the z axis, the central beam's power goes down and the side beam's power goes up first and then goes down. The turning point is around $z = 150mm$. The y-axis is the power and maximum is the output of the fiber.

stray light into the MOT capture region. This scattered light would affect the signal to noise ratio of the detection. To quickly and cheaply solve this issue, a 3D printed plastic mask (see Figure 4.20) was mounted at the end of the telescope.

The round hole in the center of the mask is left for mounting neutral density(ND) filter. For 160 mW 461 nm laser out of the fiber for the first cooling stage(see Chapter 5). There is $\approx$ 64 mW power in the central beam. For the 12.5 mm $\times$ 12.5 mm beam size, the intensity is $\approx$ 41 mW/cm^2 which is close to the saturation intensity of 43 mW/cm^2. It is a question about how the power difference would affect the MOT on either temperature and atom number. This research is still in progress. Another reason to mount the mask is to filter the stray light from the inner surface reflection.
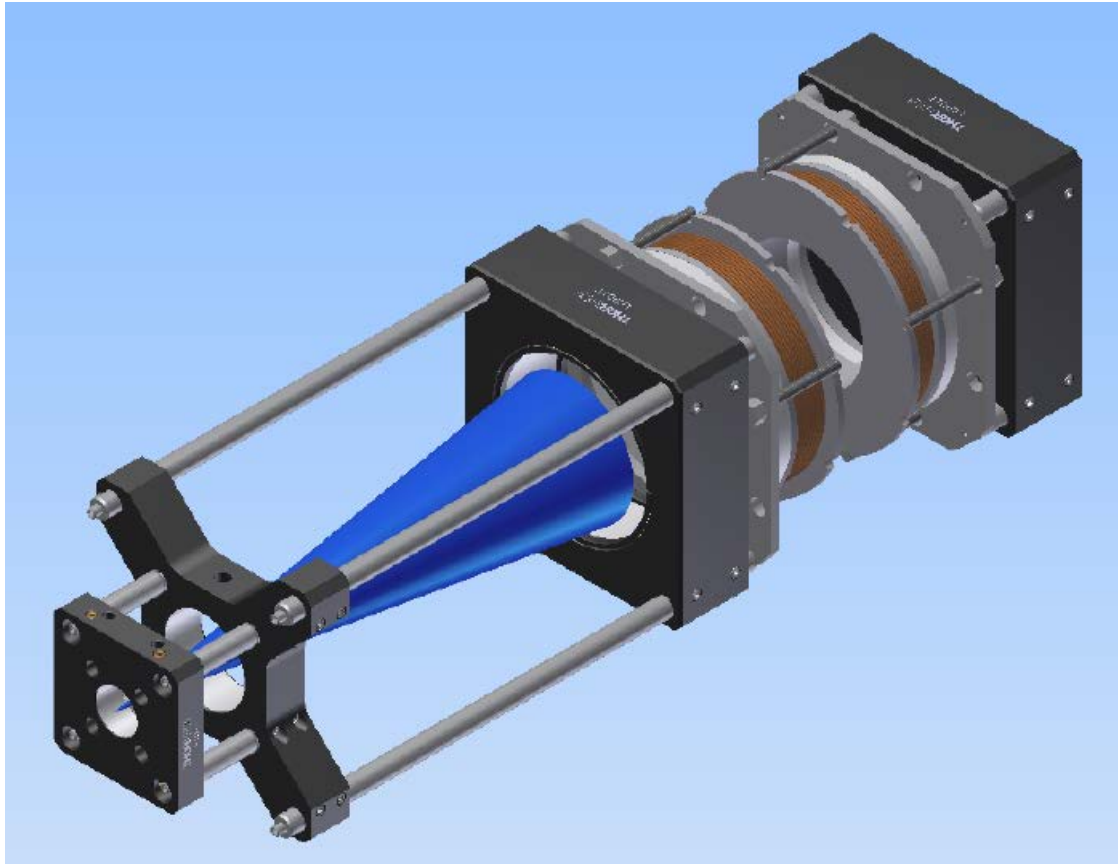
Figure 4.19: Schematic drawing of the optics. A commercial lens cage system made by is used to hold the collimation lens, the quarter waveplate and the fiber adapter. The cage system makes it convenient to adjust the lens and wave plate.
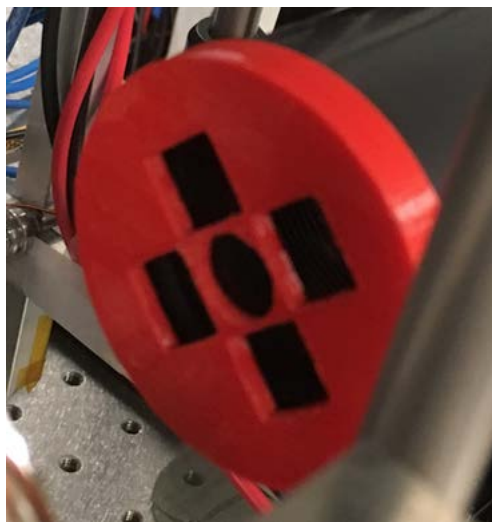
Figure 4.20: The mask is 3D printed. The four side holes are square and the center one is round for testing neutral density filters.

Chapter 5

Blue and Red MOT in the Single-beam MOT configuration

With all the hardwares introduced in the last two chapters, for the first time, we have realized the single-beam ^{88}Sr MOT. This chapter will present the related measurements and results.

A vacuum system using Chamber II (Figure 4.12) was first made to build a blue MOT demonstrator as preliminary research towards the final miniature clock vacuum chamber design. This chamber is capable of testing many different features useful for implementation in the final miniature clock, including a home-made 461 nm extended cavity diode laser (ECDL), a modified pyramid MOT design, SrO as a source of ^{88}Sr vapor, the pumping ability of the new hybrid getter-ion pump and the embedded spectroscopy locking cell. Once each of these features was tested or verified using the demonstrator design, the vacuum system was moved to the laboratory to explore its capability for operating in a actual strontium optical clock. Using laboratory-based equipments – 400 mW 461 nm laser from M Squared(SOLSTIS ECD-X) and homemade 689 nm cooling laser, we achieved a broadband red MOT with 10^4 atoms. Efforts to improve the number of atoms in the red MOT as well as to load the atoms into an optical lattice in this chamber are ongoing.

5.1 Velocity distribution

The velocity distribution of the atoms emitted from the dispenser is a key characteristic in system evaluation because it affects the total number of atoms that can be loaded into the blue MOT. Velocity distribution measurements were taken in the chamber center.

To measure the longitudinal velocity distribution a 461 nm laser beam is aligned to counter propagate with the atomic beam. Scanning the frequency of the counterpropagating laser allows us to measure the longitudinal velocity distribution. To measure the transverse velocity distribution of the atomic beam, the blue laser is aligned orthogonally to the atomic beam at the point where you would like to measure the velocity distribution.

The fluorescence from the atomic beam is amplified by a photomultiplier tube (PMT) with a 1.5 mm diameter aperture. As the laser frequency is scanning, the fluorescence intensity of the atoms changes, leading to a change in current in the PMT. Converting the PMT current into a voltage measured with an oscilloscope, the velocity distribution of the atoms in the region of interest can be measured.

Atoms at rest are excited by a laser on resonance with the atomic transition frequency f_0. Due to the Doppler effect, atoms moving with velocity v are excited by a laser resonant with the Doppler shifted transition frequency f_D:

$$f_D = f_0(1 + \frac{v}{c}),$$ (5.1)

where c is the speed of light. The frequency shift $\Delta f = f_D - f_0$ can be expressed as

$$\Delta f = \frac{v}{c}f_0.$$ (5.2)

In the case of strontium atoms, atoms with a 50 m/s velocity lead to a 100 MHz Doppler shift in the resonance frequency. To cover a wide velocity distribution of the atoms, at least 1 GHz detuning should be scanned with the laser. However, an acousto-optic modulator (AOM) with such a wide frequency range for a 461 nm laser is not available in our lab. Instead, the grating which selects the laser frequency in our ECDL (see Chapter 6) was scanned to adjust the frequency.

A side effect of scanning the grating is that the laser power changes along with the frequency. To account for this, the detection laser is split into two beams, one for fluorescence detection and the other for monitoring power fluctuations. The 461 nm laser is split by a 90%/10% beam splitter (BS) before entering the chamber, with the weak beam going to a photo diode (PD) to record the power drift. By monitoring the power fluctuations on the same oscilloscope as the fluorescence, the drift in the fluorescence measurement due to laser power drift can be removed.

A third oscilloscope channel monitors the laser wavelength as determined by a wavelength meter. The spectral bandwidth of the wavelength meter(ADVANTEST Q8326) used in our lab only extends down to 480 nm, leading to an unknown absolute accuracy in the wavelength measurements. As a result, the transverse velocity distribution in the center of the MOT chamber is measured first because the peak of the distribution indicates the unshifted atomic resonance frequency of zero velocity atoms.

Figure 5.1 identifies the resonance frequency of the ^{88}Sr atom by measure the fluorescence intensity in the center of the MOT chamber with dispenser currents of 3.6 A, 4.0 A and 4.3 A. For the $^1S_0 - ^1P_1$ transition in the four isotopes of strontium, the frequency shifts relative to ^{88}Sr are -49.2 MHz, -124.5 MHz and -270.6 MHz for ^{87}Sr, ^{86}Sr and ^{84}Sr, respectively [75]. The bump on the three curves which are more than 100 MHz which means it is the ^{86}Sr isotope. ^{87}Sr is not visible in the

plots because of the low resolution of the laser scan and the wavelength meter.
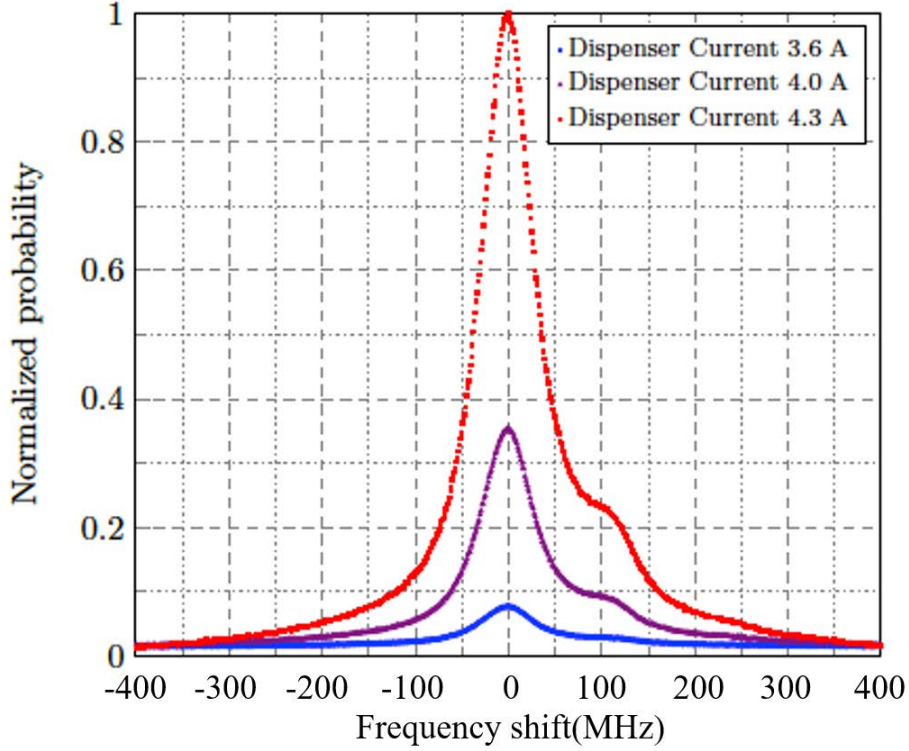
Figure 5.1: Transverse fluorescence intensity in the center of the chamber with dispenser currents of 3.6 A, 4.0 A and 4.3 A. The result shows the relative resonance frequency of the ^{88}Sr atoms, preparing for the longitude velocity measurement. The bump on the right side of the curve is ^{86}Sr.

In Figure 5.2, the points show the measured results of the longitudinal velocity distribution in the center of the MOT chamber for dispenser currents between 3.6 A and 4.3 A. The dashed line is a Maxwell-Boltzmann distribution fit to the data. For higher currents, the peak of the curves moves towards higher temperatures in accordance with the theory.

For Maxwell-Boltzmann distribution, the most probable speed v_p of a gas is

$$v_p = \sqrt{\frac{2k_BT}{m}} = \sqrt{\frac{2RT}{M}}, \tag{5.3}$$

where $k_B = 1.38064852(79) \times 10^{-23}$ J K^{-1} is the Boltzmann constant, T is the thermodynamic temperature of the gas, m is the particle mass, $R = 8.3144598(48)$
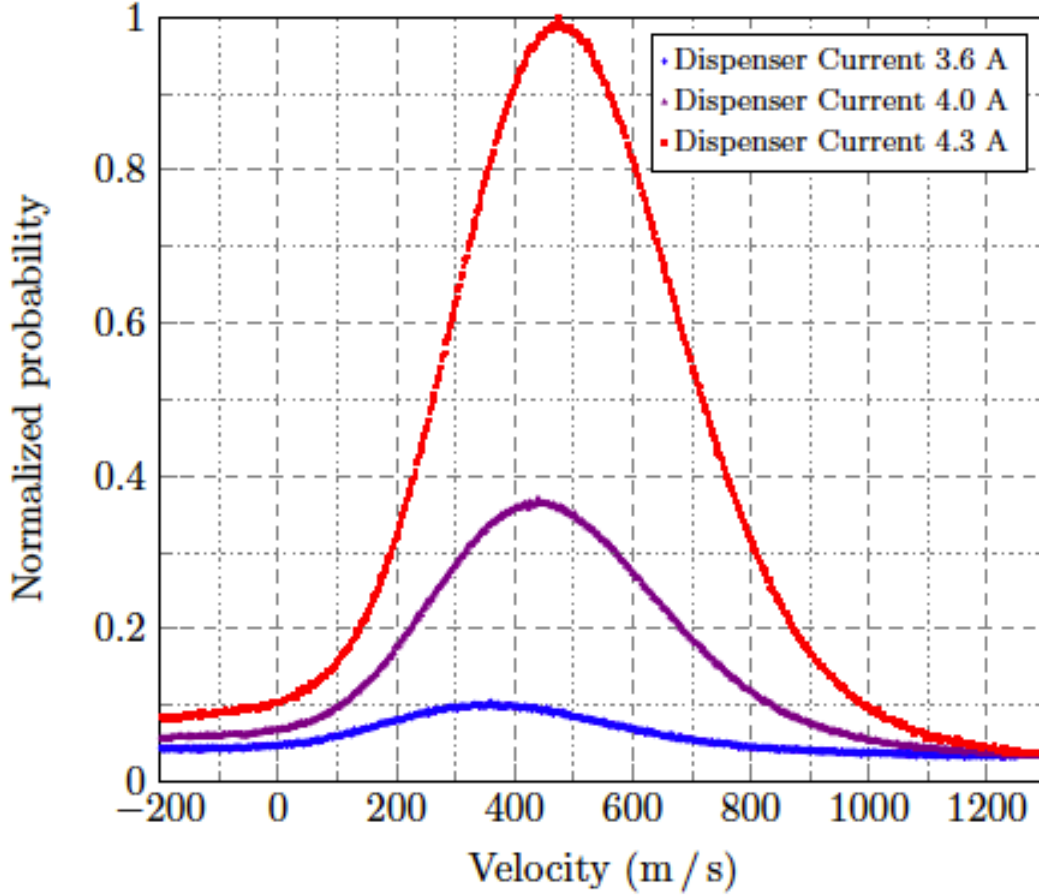
Figure 5.2: Longitude velocity distribution in the center of the scientific chamber with dispenser currents of 3.6 A, 4.0 A and 4.3A. The negative velocity may come from the strontium atoms being reflected from the wall of the vacuum chamber.

J mol^{-1} K^{-1} is the gas constant and M is the molar mass of the material. From Figure 5.2, the strontium gas temperatures are 686.6±10.0 K, 1022.1±10.0 K and 1192.6±10.0 K for dispenser currents 3.6 A, 4.0 A and 4.3 A, respectively.

The longitudinal velocity distribution reveals that an increase in dispenser current increases the overall number of atoms in the low velocity tail of the distribution, which leads to a higher number of atoms loaded into the MOT. A higher dispenser current will increase the pressure in the chamber, limiting the lifetime of the MOT. The vacuum pressure has been recorded during velocity distribution measurements. The results are shown in Table 5.1, which shows the upward trend of the vacuum pressure when the dispenser current is increased. A trade-off occurs between the number of atoms loaded into the MOT and an increase in the vacuum pressure
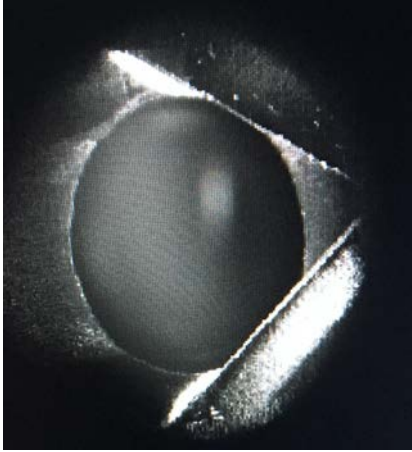
(a) Real MOT image

(b) MOT image without background

Figure 5.3: Blue MOT with the Low Power 461 nm Diode Laser

during MOT operation.

3.6 A	4.0 A	4.3 A
$(1.5 \pm 0.2) \times 10^{-10}$ mbar	$(2.7 \pm 0.1) \times 10^{-10}$ mbar	$(1.5 \pm 0.3) \times 10^{-9}$ mbar

Table 5.1: The vacuum pressure recorded by the ion pump of the getter-ion pump. The error came from the average of three measurements. These measurements were taken after 30 minutes continuous dispenser operation when the vacuum reading had reached the steady states.

5.2 Blue MOT using a 461 nm diode laser

The first blue MOT using a single beam configuration was obtained using a home-made 461 nm extended cavity diode laser (ECDL). Figure 5.3a shows a picture of the MOT as seen on a CCD camera(pco.pixelfly usb, model PF-M-QE-PIV), and Figure 5.3b shows the MOT image after subtraction of the strong background fluorescence. To load the MOT in Figure 5.3, the dispenser current is 3.6 A, and the corresponding vacuum pressure is 1.9×10^{-10} mbar. The coil current is 2.5 A, providing 35 G/cm magnetic field gradient. The total laser power entering the telescope system is 12.5 mW. As calculated in the single beam telescope Section 4.2, this corresponds to 3.75 mW (or 2.4 mW/cm^2) in the center beam and 1.25 mW (or 0.8 mW/cm^2) in each

of the side beams. The laser detuning is 40 MHz, and no repumping lasers were used while loading the MOT.

Given the above parameters, the atom number is estimated by the MOT fluorescence. For an atom in the MOT, the scattering rate of an atom γ_p, in number of photons emitted per second, is related to the laser intensity I and detuning Δ [93] by

$$\gamma_p = \frac{I/I_s \cdot \Gamma/2}{1 + I/I_s + (2\Delta/\Gamma)^2}, \tag{5.4}$$

where $I_s = 43$ mW/cm^2 is the saturation intensity, and $\Gamma/2\pi = 32$ MHz is the natural linewidth of the $^1S_0 - ^1P_1$ transition. While the atoms emit photons in all directions, only a fraction of those atoms actually hit the camera's CCD. The camera's photon collection efficiency r can be calculated as

$$r = \frac{\pi(D_L/2)^2}{4\pi(d_L/2)^2} = \frac{D_L^2}{4d_L^2}, \tag{5.5}$$

where D_L is the diameter of the camera lens, and d_L is the distance between the photon source and the lens. The efficiency of the detection system also creates errors for the fluorescence intensity calculation. The transmission efficiency T_L of the lens and the quantum efficiency QE of the sensor at 461 nm affect the number of photons recorded by the sensor per unit time, n:

$$n = \frac{N}{QE \cdot t \cdot T_L}, \tag{5.6}$$

where N is the number of photons emitted by the MOT which reach the lens during the camera exposure time t. In our experiment, the camera (pco.pixelfly usb, model PF-M-QE-PIV) has a quantum efficiency of 55% at 461 nm. Combining Equations

5.4, 5.5 and 5.6 gives an estimate of the atom number N_{MOT} in the MOT:

$$N_{MOT} = \frac{n}{\gamma_p \cdot r}. \tag{5.7}$$

The MOT loaded using the 461 nm diode laser captured $\approx$1000 atoms. Even though the setup meets the minimum requirement of a visible MOT, the small atom number limits the further progression of the clock to the second stage cooling. More blue laser power is required to load a larger number of atoms into the MOT.

5.3 Blue MOT from the high power 461 nm laser

The homemade high power 461 nm laser outputs over 300 mW of power and replaces the low power 461 nm diode laser to explore the potential of the vacuum system for use in a functional strontium clock. Adding two repumping lasers at 707 nm and 679 nm also increases the total number of atoms loaded into the MOT. After optimization, the atom number in the MOT reaches the 10^6 level, which is sufficient to proceed to the next step – the red MOT.

Figure 5.4 shows an image of the MOT image using the 80 mW blue laser as cooling light, 5 mW of 707 nm repumper, 5 mW of 679 nm repumper and a dispenser current of 4.5 A, while the other experimental conditions remain unchanged from the previous MOT using the low power blue diode laser. Compared to the MOT in Figure 5.3, the brightness of the trapped atoms in Figure 5.4 is easily distinguishable from the background fluorescence.

Loading time: As indicated in Figure 5.2, higher dispenser currents emit a larger number of low velocity strontium atoms. Using a PMT to monitor MOT fluorescence and manually switching the anti-Helmholtz coil currents on and off, we can observe
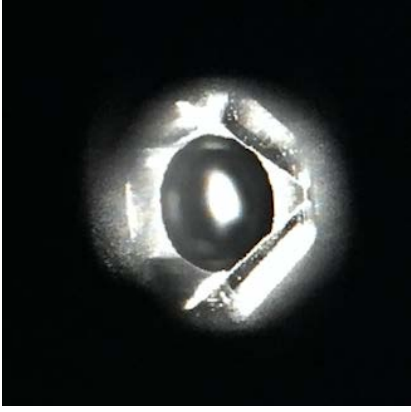
(a) Real MOT image by high power blue laser and repumping laser

(b) MOT image without background by high power blue laser and repumping laser

Figure 5.4: Blue MOT from the High Power 461 nm Laser and Repumping Lasers

MOT loading curves for different dispenser currents. Figure 5.5 shows the results of each loading curve measurement with the background fluorescence subtracted. To find the loading times for different dispenser currents, the PMT signal is fit with the MOT loading rate equation:

$$N(t) = N_s(1 - e^{t/\tau}), \tag{5.8}$$

where $N(t)$ is the number of atoms in the MOT as a function of time t, N_s is the steady state atom number and τ is the MOT loading time.

Table 5.2 shows the measured loading times for five different dispenser currents. As expected, higher dispenser currents leads to decreased loading times.

Dispenser current(A)	3.7	4.0	4.3	4.5	4.7
Loading time(s)	1.45	0.59	0.23	0.18	0.16

Table 5.2: MOT loading time vs Dispenser current. Increasing the current on the dispenser would result in a shorter loading time. The 0.2 second delay is added to observe the background noise.

Atom number: Figure 5.5 suggests that higher dispenser currents leads to a higher steady state atom number. Laser intensity, or power, can also affect the trapped
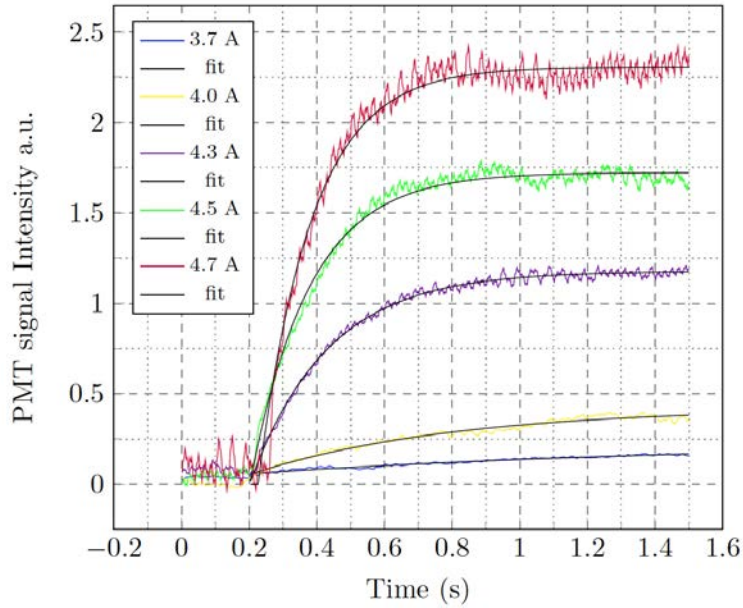
Figure 5.5: MOT loading vs Dispenser current. The vertical axis is in arbitrary unit. The actual loading signal is in colored lines and the black line is the fitting.

atom number. To investigate this, we loaded MOTs using lasers with 80 mW and 160 mW coming out of the fiber before entering the chamber. Figure 5.6 shows comparison images of the MOT in the steady state for both laser powers using different dispenser currents. The first row of MOT images uses the 160 mW 461 nm laser, and the second row uses the 80 mW blue laser. From left to right, the five pictures in each row represent MOT images generated by dispenser currents of 3.7 A, 4.0 A, 4.3 A, 4.5 A, 4.7 A, respectively. The color-coded axes are in arbitrary normalized units.
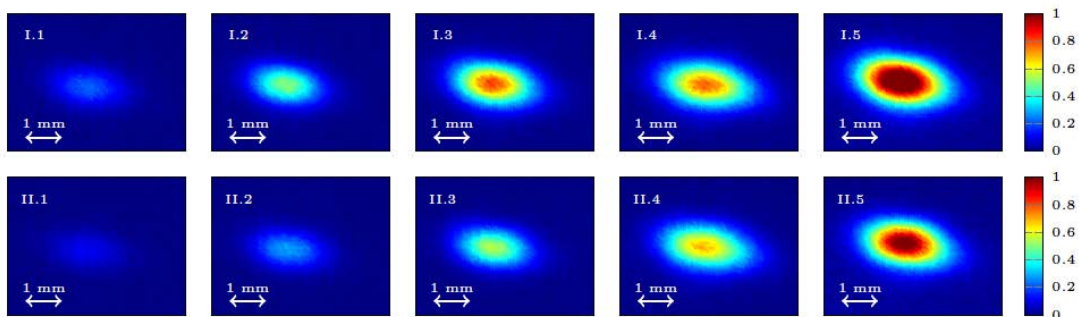
Figure 5.6: Images of stable MOTs with different dispenser currents and laser powers

Using Equations 5.4 to 5.7, the atom numbers in each MOT are calculated. Figure

5.7 shows the dependence of the atom number on dispenser current and laser power. At higher dispenser currents, higher laser powers result in higher atom numbers. This trend likely continues for lower dispenser currents, but the signal-to-noise (SN) ratio in the camera images is too low to resolve differences in atom numbers at these levels.
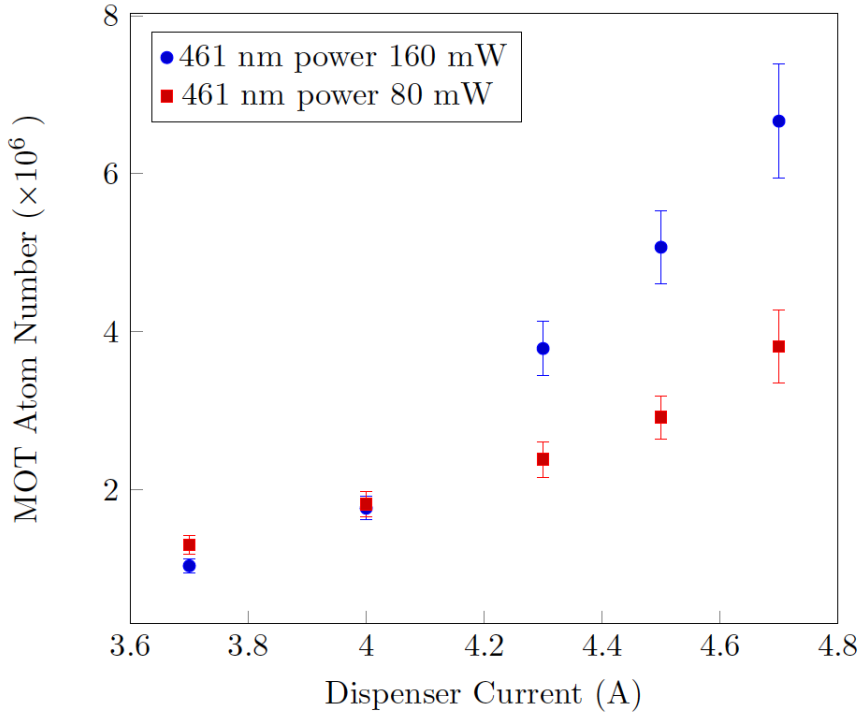
Figure 5.7: The Dependence of the Atom Number on Dispenser Currents and Laser Power

During the velocity distribution measurements, the dispenser current only went up to 4.3 A, where the vacuum pressure readings remained in the lower 10^{-10} mbar range. However, in pursuit of higher atom numbers, the dispenser current was increased to higher values. For 4.5 A and 4.7 A, the vacuum readings are $(2.6 \pm 0.1) \times 10^{-9}$ mbar and $(5.9 \pm 0.2) \times 10^{-9}$ mbar, respectively. From previous experience with the SOC II project [79], with around 50% transfer efficiency from the first stage to second stage cooling, 5×10^6 atoms in the blue MOT is acceptable. As a result, the dispenser current is limited to 4.5 A in the following experiment.

Temperature of the MOT: In preparation for transferring atoms into the red

MOT, the temperature of the atoms in the blue MOT has been determined using the time-of-flight [94] measurement technique.

In the first step, strontium atoms are cooled and loaded into a blue MOT. An in situ image of the MOT is captured by a well calibrated camera whose focal plane coincides with the MOT cloud. Assuming the atomic cloud has a uniform temperature T_M, the velocity distribution $f(v)$ of the atoms is a Maxwell-Boltzmann distribution:

$$f(v) = \sqrt{\frac{m}{2\pi k_B T_M}} e^{-\frac{mv^2}{2k_B T_M}}, \tag{5.9}$$

where m is the mass a single strontium atom and v is the velocity. The spatial distribution $f(r)$ of the atoms in the MOT follows a Gaussian distribution:

$$f(r) = \frac{1}{\sqrt{2\pi} r_M} e^{-\frac{r}{2r_M^2}}, \tag{5.10}$$

where r is the position of an atom in the cloud, and r_M is the radius of the MOT. In the second step of the time-of-flight measurement, the anti-Helmholtz coils and cooling laser are switched off. In the absence of the optical and magnetic fields, the atom cloud will expand freely. After some time t, the atom originally in position r_i travels to position $r_t = r_i + vt$. The position distribution after evolution time t becomes

$$f'(r_t, t) = \int_{-\infty}^{+\infty} f(r_i) f(v) dr_i = \int_{-\infty}^{+\infty} f(r_i) f\left(\frac{r_t - r_i}{t}\right) dr_i = f(r_i) * f(v). \tag{5.11}$$

From Equation 5.11, the MOT radius becomes

$$r^2 = r_0^2 + (\frac{k_B T_M}{m})^2 t^2. \tag{5.12}$$

The third step in the time-of-flight measurement is to switch on the blue laser to take an image of the atom cloud at time t. Comparing the images before and after a free expansion time t, the temperature of the MOT can be calculated using Equation 5.11. Figure 5.8 contains two pictures of the cloud from a time-of-flight measurement with a 17 ms expansion time. Along the y axis, the original radius of the MOT is 1.25 mm, and after 17 ms, the radius has expanded to 1.75 mm. For the x axis, the radius expands from 0.51 mm to 0.75 mm. The temperature along the y axis is 2.58 ± 1.16 mK, while the temperature along the x axis is 1.22 ± 0.37 mK. This result is in reasonable agreement with the 1.5 mK Doppler cooling limit for strontium atoms during the first stage cooling process.
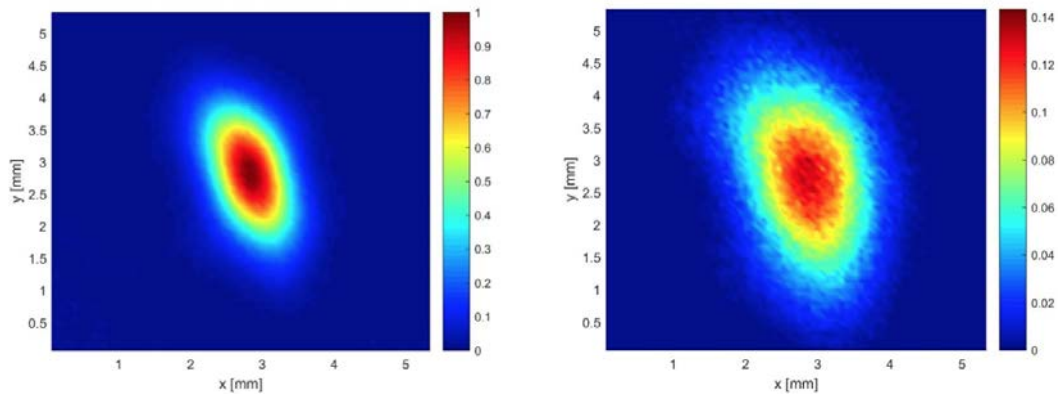
Figure 5.8: Time-of-flight Method is used to to measure the temperature of the MOT. After takeing a picture, the MOT is released by turning off the light field and magnetic field. After 17 ms, the cooling laser is turned on the take another picture. The size difference tells us the temperature in the low mK level.

MOTs for four different isotopes of Sr: All of the data presented so far for the blue MOT is based on the ^{88}Sr isotope. We have also been able to demonstrate the possibility to trap the other two stable, less abundant isotopes of Sr in our miniaturized chamber, including ^{87}Sr, which is the isotope of generally used in optical lattice clocks, and ^{86}Sr and ^{84}Sr which are used in strontium Bose-Einstein condensate (BEC) experiments.

The $^1S_0 - {}^1P_1$ cooling transition frequency is slightly different for each isotope. The
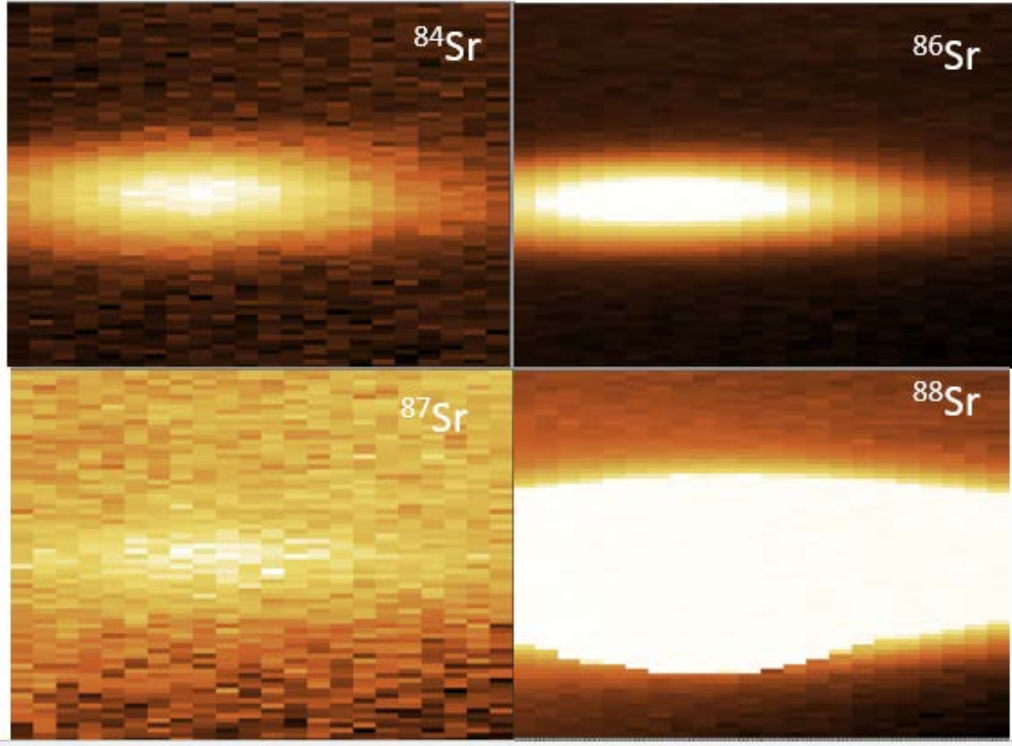
Figure 5.9: The experimental condition were set to the same for the four isotopes. ^{87}Sr is convered by the strong fluorescence of ^{88}Sr.

master laser is locked to ^{88}Sr atoms and the frequency is shifted by AOMs. The frequency is red-detuned by 49.2 MHz for ^{87}Sr, 124.5 MHz for ^{86}Sr and 270.8 MHz for ^{84}Sr. All other experimental parameters remain the same for all isotopes – the dispenser current is 4.5 A, the laser power is 160 mW, frequency detuning is 40 MHz, the magnetic field gradient is 35 G/cm and the camera exposure time is 0.5 ms. Figure 5.9 shows the MOTs obtained for ^{88}Sr, ^{87}Sr, ^{86}Sr and ^{84}Sr.

5.4   Red MOT

Using the modified pyramid MOT chamber, atoms have been successfully transferred from the blue MOT into a broadband red MOT. This demonstrates the suitability of the chamber design for its continued development towards a miniaturised strontium clock. In addition, to our knowledge this is the first red MOT loaded using a single

beam pyramid MOT design. The red second stage cooling laser is a homemade 689 nm external cavity diode laser (ECDL), which is stabilised to a 3 cm long F = 10000 high finesse optical cavity. To efficiently transfer atoms from the "hot" blue MOT to the "cold" red MOT, the 689 nm laser is frequency broadened first. Once atoms are transferred into the broadband red MOT, the frequency modulation is removed to generate a cold, single frequency MOT. A broadband red MOT of around 1000 atoms has been realized using the single-beam MOT chamber. With further optimization, we expect to be able to increase the transfer efficiency into the red MOT.

689 nm laser locking and broadening: As explained in Chapter 2, before transferring atoms into the lattice, strontium atoms undergo two cooling stages. After loading a large number of atoms into the blue MOT, the $^1S_0 - {}^3P_1$ intercombination transition, with a linewidth of 7.5 kHz, is used to cool the atoms to below the μK level. The free running linewidth of the 689 nm ECDL is in the 100 kHz range, which is broader than the transition linewidth. To obtain such a narrow transition, a Fabry-Perot cavity is a popular technique for stabilising the laser frequency.

To make a stable red MOT laser, the 689 nm laser diode has a AR coating to prevent mode competition, which may lead to instabilities in the laser frequency. Although using the same Littrow configuration as the 461 nm diode laser, the distance between the diode and the grating is 10 cm, much longer than the 3 cm cavity length in the blue laser. When the laser is in free running mode, the linewidth is about 170 kHz. The laser is locked to a homemade high finesse cavity to narrow the laser linewidth. As seen in Figure 5.10, the mirrors with multiband coatings are attached to the cavity using optical contacting techniques. The details can be found in Reference [95]. With the addition of a tapered amplifier (TA), 13 mW of 689 nm light is coupled into the fiber to the single-beam MOT chamber to cool the atoms.

Figure 5.10: The cavities are multiband coated for stabilizing more than one laser in one cavity. The length of the ultra low expansion(ULE) cavity body is $30mm$.

As the temperature measurement states, the atoms in the blue MOT reach temperatures of a few mK. Doppler broadening at such low temperatures still occurs at the MHz level. Applying the cavity locked 689 nm laser directly to the blue MOT, only a few percent of the atoms can be trapped in the red MOT. The conventional way to solve this issue is to split the second cooling stage into two phases. In the first phase, the red cooling laser is artificially spectrally broadened to a few MHz to initially load the atoms in the red MOT. In the second phase, the broadening is removed to cool the atoms to their minimum temperature.

We use an AOM to broaden the frequency of the 689 nm cooling laser. The frequency modulation depth is 1.2 MHz centered around the natural transition frequency to effectively cover the entire Doppler broadened frequency spectrum of the atoms in the blue MOT. By scanning the AOM frequency, the total laser power is distributed between all the frequency components. The more closely spaced the frequency components of the cooling laser are, the more atoms it can cool. Each frequency component should contain a laser intensity higher than the saturation intensity of 3 μW/cm^2. Although 13 mW of red light is coupled out of the fiber, only about 4 mW is actually available to cool the atoms in the single beam config-

uration. The frequency modulation rate of the laser is set to 40 kHz, and the total laser intensity is $\approx$400 μW/cm^2.

Sequence to reach the red MOT: Figure 5.11 details the experimental timing sequence used for cooling and trapping strontium atoms in the broadband red MOT phase.
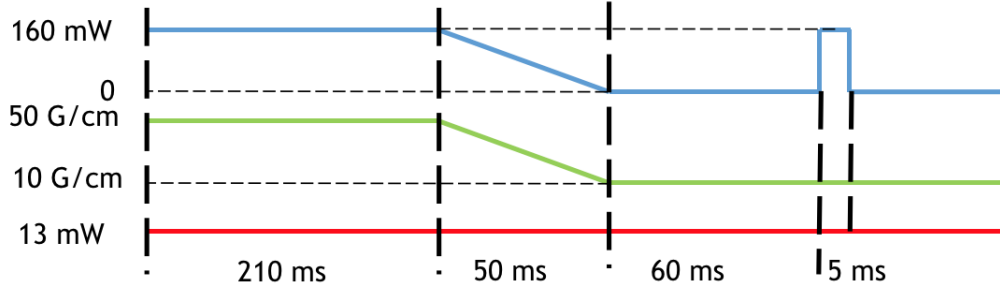
Figure 5.11: Sequence from hot atom to the second stage cooling. The power axes of 461nm laser and 689nm laser is the total power in the fiber, $\approx$30% of the power is used to cool the atoms. The 707 nm laser is always shining to the chamber center.

The dispenser current is at 4.5 A throughout the entire process. The 707 nm repumping laser is always on, while the 679 nm repumping laser was always off due to a malfunction in this laser. The 461 nm laser has a power of 160 mW coming out of the fiber. From this light, only 48 mW is incident on the MOT trapping region. 2.5 A applied to the anti-Helmholtz coils corresponds to a gradient of 35 G/cm in the centre of the chamber. After 210 ms, around 5×10^5 atoms are trapped in the blue MOT. At this point, the blue cooling laser power is ramped down to zero over a period of 50 ms. At the same time that the blue MOT beams are ramping down, the magnetic field gradient simultaneously ramps down to 7 G/cm. The 13 mW 689 nm laser, which is overlapped with the 461 nm laser inside the same fiber (see Chapter 3), is applied to the atoms throughout the entire timing sequence. Effectively, 4 mW of the broadband second stage cooling laser falls in the MOT trapping region. 60 ms after the blue laser and the field gradient are ramped to their minimum values, the blue laser is switched on for 5 ms to detect the red MOT via fluorescence. The cam-

94

era is also triggered at the beginning of the 5 ms time frame with a 5 ms exposure time. Three pairs of Helmholtz coils are always on to compensate for the Earth's background magnetic filed and any stray magnetic fields present in the vicinity of the experiment chamber.

Figure 5.12 is an image of the first broadband red MOT detected in the modified pyramid MOT chamber. The diameter of the red MOT is around 4 mm and it contains about 1000 atoms. With around 5×10^5 atoms in the blue MOT, the transfer efficiency between the blue and red MOTs is $\sim 2\%$. Work at this stage is ongoing, and we expect to improve the transfer efficiency with further optimisation. With these preliminary results showing a red MOT, we have paved the way towards successfully demonstrating a miniaturized strontium lattice clock.
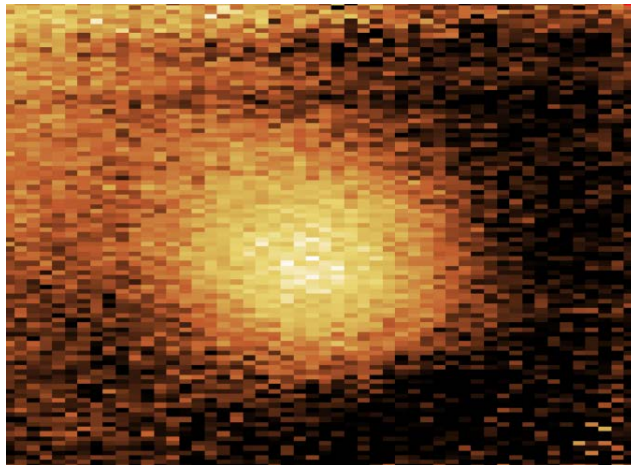
Figure 5.12: Red MOT image

Chapter 6

New Atom Source for Strontium Clock

All early versions of the strontium clock experiments at the University of Birmingham, including the use of a 2D MOT for a transportable system(see Figure 4.1) and the Zeeman slower used in the SOC II project (see Figure 4.3) [79], require a high power 461 nm laser to slow the atoms. The high power requirements, typically in the range of 50-100 mW, necessary to operate a 2D-MOT or Zeeman slower are currently not available in a compact format. These pre-cooling apparatuses increase the overall volume and complexity of the clock apparatus. The low vapor pressure of strontium at room temperature requires the continuous operation of ovens or dispensers to provide a source of strontium atoms. The high temperatures of over 400 °C of these devices causes a significant AC-Stark shift in the clock transition by the black body radiation (BBR) [96] which shifts the clock frequency and affects the clock accuracy.

To avoid the above drawback a new strontium source has been developed with low power consumption requirements and which do not require pre-cooling laser techniques. As a potential solution, we have used strontium oxide as a source of strontium vapor to load a blue MOT with atom numbers in the 10^6 range. This research may give rise to a great improvement available for use with strontium

optical lattice clocks.

The first section of this chapter talks about the discovery of SrO as an atom source. The second section is based on a paper "Laser controlled atom source for optical clocks" that has been published on Scientific Report 6, Article number:37321. The authors are Ole Kock, Wei He, Dariusz Swierad, Lyndsie Smith, Joshua Hughes, Kai Bongs and Yeshpal Singh. The first two authors contributed equally to the work.

6.1   From coating removal to atom source

As some of the discoveries in history began with another problem which needed to be solved. After 4 years of operation, one viewport facing the dispensers in the transportable strontium clock apparatus (see Figure 4.1) was coated with strontium. Because the strontium coating blocked the transmission one of the repumping lasers, we wanted to remove the coating without opening the vacuum, which would ruin the dispensers and would require a re-baking of the system. The paper [97] on light-induced atom desorption (LIAD) of alkali metals raised the possibility of removing the strontium atoms using an ultraviolet (UV) laser. Figure 6.1 shows the first test using the oven based spectroscopy cell, which is heavily coated with strontium. With an unfocused 405 nm UV laser, no visible change could be detected on the strontium coating. After focusing the beam on the inner surface as seen in Figure 6.1a, we observed a change in color between the illuminated coating area and the unexposed coating area.

To verify if the color change came from coating removal or from thermal effects on the glass, a 461 nm laser on resonance with the $^1S_0 - ^1P_1$ transition was used to detect fluorescence of the atoms. In Figure 6.1b, atomic fluorescence is observed near the focus of the 405 nm laser. The fluorescence not only provided a method to
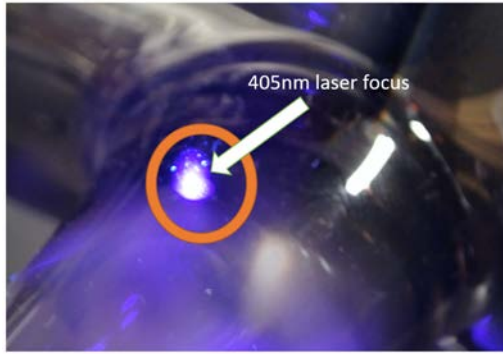
(a) A $405nm$ laser was focused to the inner surface of the cell where had been coated with strontium.
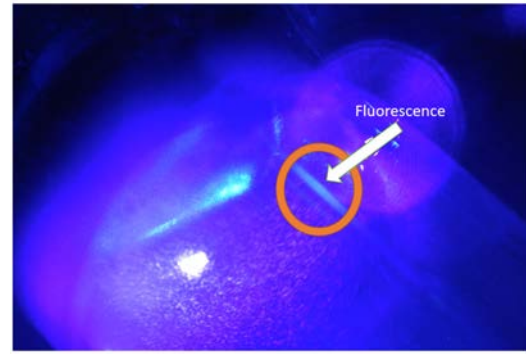
(b) When the strontium was released from the coating, a fluorescence was observed.

Figure 6.1: The test of removing strontium coating

remove a strontium coating, but also presented the possibility of using laser-induced strontium emission as an atom source.

Further investigations were undertaken to clarify the effects causing the emission of atoms. A compact test vacuum chamber as seen in Figure 4.2 provided the experimental environment for the possible atom source. Figure 6.2 shows the fluorescence from the Sr sample in the MOT chamber. The solid strontium was mounted on an aluminum tray 4 cm away from the chamber center as seen in Figure 6.2a. The short distance between the atom source and a resonant laser beam was to facilitate a bright fluorescence signal. Figure 6.2b demonstrates strong fluorescence from the solid strontium.

Solid strontium with a purity of 99% from Sigma-Aldrich was used in the experiment. The strontium pieces are packaged under mineral oil due to the quick oxidation of the sample after strontium becomes exposed to air. During the vacuum chamber assembly, the vacuum chamber was filled with argon to remove any oxygen previously present. Before sealing the last viewport, the strontium was washed with acetone and moved to an aluminum holder inside the chamber. Although the pumping began nearly instantly, the remaining oxygen in the chamber reacted with the strontium
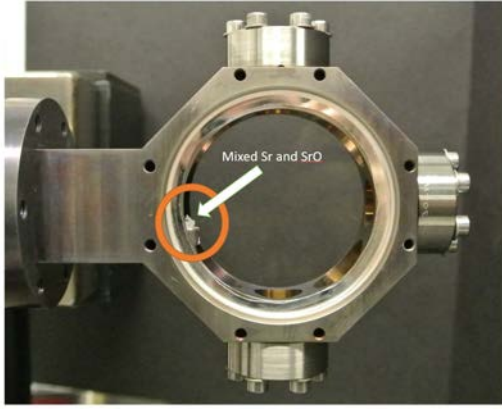
(a) The strontium sample is held near the center of the MOT chamber. The strontium sample is visible at the left hand side of the viewport.
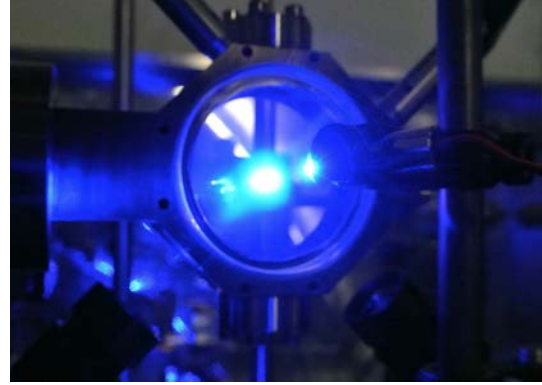
(b) While focussing the 405 nm laser on the Sr sample, a strong fluorescence was visible in the chamber.

Figure 6.2: Solid strontium tests in MOT chamber

to leave a layer of white strontium oxide covering the solid strontium (see Figure 6.2a).

Using a 405 nm laser focused on the strontium sample to produce a source of strontium atoms, we were able to load atoms into a blue MOT. However, the mechanism for the emission of strontium in the presence of both solid strontium and strontium oxide had not been well researched. Since it is difficult to completely eliminate the presence of oxygen in the vacuum chamber, we followed the route of investigating the effects of the oxide layer by using pure strontium-oxide as a source. Figure 6.3 shows a viewport in a simple vacuum system made with a 4-way cross.

The vacuum included three samples – commercial SrO powder with 99.9% purity from Sigma-Aldrich, homemade SrO powder made by exposing bulk strontium to air for a few hours and the same solid strontium used in the MOT chamber. The solid strontium was placed within the setup at the last minute as in the MOT chamber, which was exposed as briefly as possible to air. The same 405 nm emission laser with variable power used in the MOT experiment was focused on the samples, and fluorescence was observed from each of them. Even if pure strontium is capable of
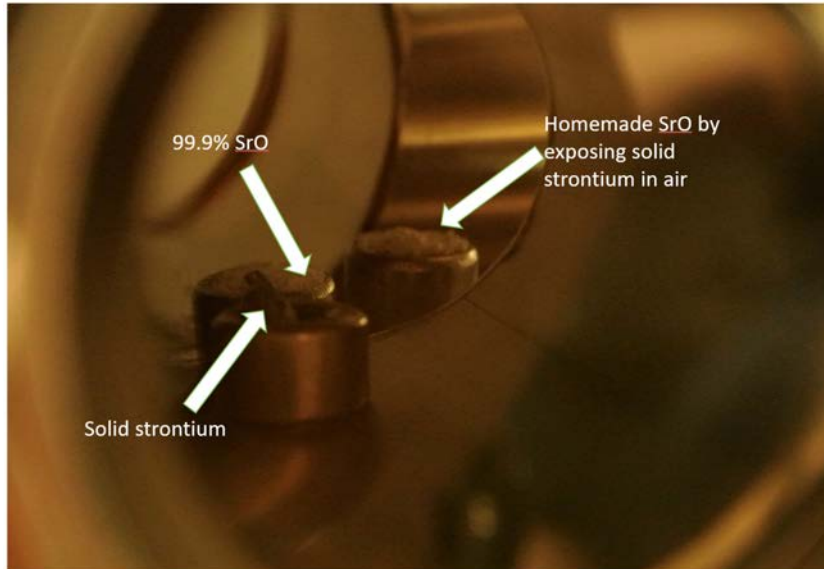
Figure 6.3: Three different strontium-oxide preparations in a vacuum chamber: Pure commercial SrO powder, homemade highly porous SrO, a layer of SrO on the solid strontium tested in the vacuum.

emitting strontium atoms, strontium oxide can also be considered as a strontium source.

With the realisation that strontium-oxide is a viable source, we stopped pumping the MOT chamber for 4 hours to fully oxidize the solid strontium. Then the pumping was restarted to reach the typical MOT operation pressure of 10^{-9} mbar. A conventional six-beam MOT configuration was used for loading and decay measurements. The emission laser was focused at the surface of the sample with a diameter of 200 μm. A computer control system switched the emission laser on and off by controlling a shutter with a short 8 ms jitter. A typical MOT capture-and-release experiment using SrO as an atom source is shown in Figure 6.4. For the measurement in Figure 6.4, the shutter was open for 2 s and closed for 2 s.
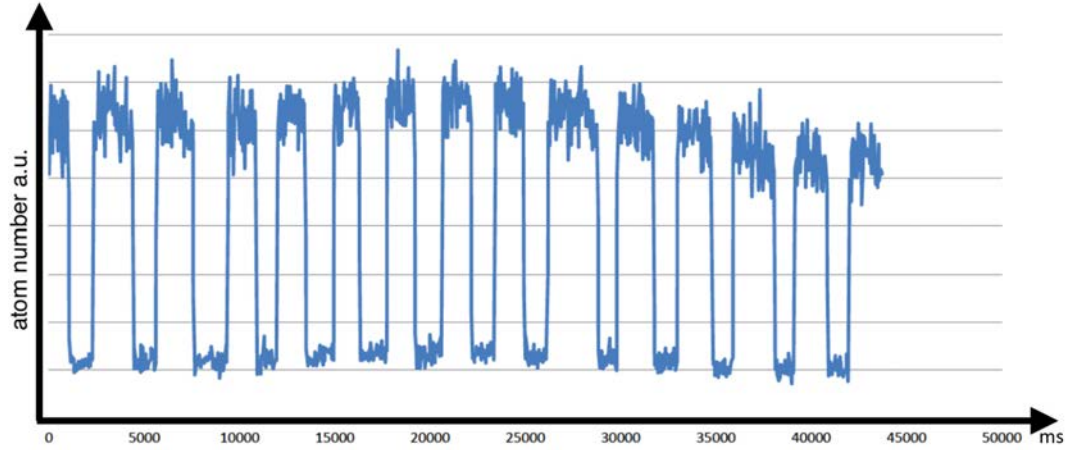
Figure 6.4: The y-axis is the atom number in the MOT. The x-axis is the time in ms unit.

6.2 Laser controlled atom source for optical clocks

6.2.1 Abstract

Precision timekeeping has been a driving force in innovation, from Stonehenge defining agricultural seasons to atomic clocks enabling satellite navigation, broadband communication and high-speed trading. We are on the verge of a revolution in atomic timekeeping, where optical clocks promise an over thousand-fold improvement in stability and accuracy. However, complex setups and sensitivity to thermal radiation pose limitations to progress. Here we report on an atom source for a strontium optical lattice clock which circumvents these limitations. We demonstrate fast, cold and controlled emission of strontium atomic vapours from bulk strontium oxide irradiated by a simple low power diode laser. Our results demonstrate that millions of strontium atoms from the vapour can be captured in a magneto-optical trap (MOT). Our method enables over an order of magnitude reduction in scale of the apparatus. Future applications range from satellite clocks testing general relativity to portable clocks for inertial navigation systems and relativistic geodesy.

101

6.2.2 Background of the research

In recent years, there has been tremendous progress in the field of precision metrology and quantum measurements with optical lattice clocks demonstrating a frequency uncertainty on the order of 2 parts in 10^{18} [4, 41, 98, 99]. In an optical lattice clock, many ultracold neutral atoms confined in periodic light potentials can be used simultaneously for precision metrology and quantum measurements, and the spectroscopy becomes independent of the motion of the centre-of-mass of the atoms [1]. The wavelength and polarisation of the lattice laser is chosen such that the two probed electronic states of an atom experience the same light shifts and perturbations on the clock transition are minimised. One central remaining systematic effect in these systems is posed by systematic shifts caused by black body radiation (BBR) [96, 100, 101]. This thermal radiation depends on the temperature of the enclosure of the probed atoms, where particular challenges result from an inhomogeneous thermal distribution around the atom source. This is of particular importance for Sr which typically has to be heated to several hundred degrees to generate sufficient vapour pressure.

The atom source creates another limitation when it comes to novel applications of state-of-the-art clocks. The typically used Zeeman slower systems add size, complexity and power consumption, rendering the creation of a master space optical clock [102, 103] or portable clocks for mapping the Earth's gravitational field via relativistic geodesy [104–106] extremely challenging.

Here we report on a novel atom source, which operates without any significant heat generation, uses minimal space and allows a high degree of control in a simple, low-power setup. Starting from strontium-oxide, our source differs from light-induced atomic desorption (LIAD) [97, 107–112], which has been successfully used with al-

kali metals, but to our knowledge has not been demonstrated using alkaline earth metals. We demonstrate the practicality of our laser-controlled atom source by the operation of a Sr magneto-optical trap (MOT) and we characterise lifetimes and velocity distributions. We find that the parameters are suitable for the operation of optical lattice clocks, opening the pathway to compact systems for novel applications outside of the laboratory.

6.2.3 Results

Our atom source relies on the release of Sr atoms from a bulk sample of strontium oxide when irradiated with a laser. In the experimental setup shown schematically in Figure 6.5a, we employ a simple off-the shelf 405 nm diode laser module for this purpose. However, note that we observe atom emission for many wavelengths, including 532 nm, 922 nm and 1560 nm, at laser powers as low as 5 mW. When irradiating the SrO, we can readily see fluorescence of Sr atoms in a nearby probe beam resonant with the 461 nm transition in Sr (Figure 6.6). The remaining question is whether the velocity profile of the emitted atoms contains suitably low velocities to allow trapping with laser cooling methods.
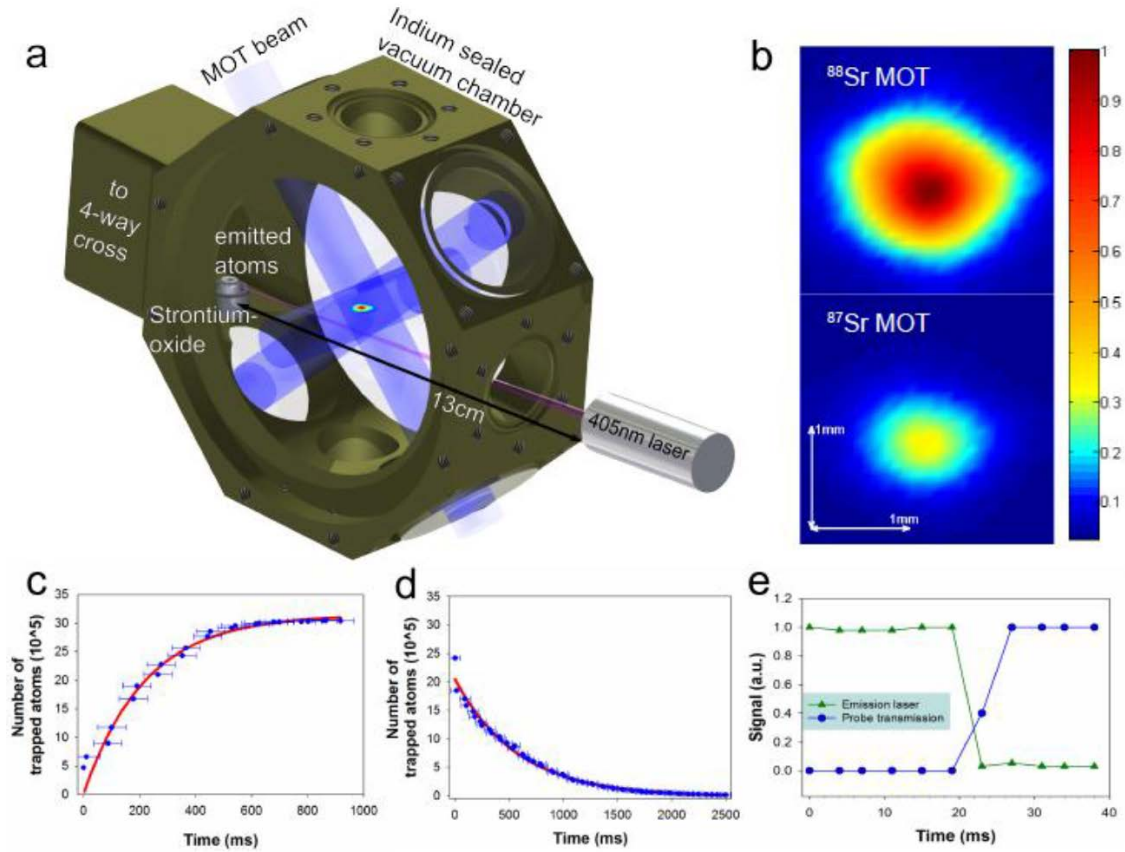
Figure 6.5: **Experimental setup.** **(a)** A schematic showing all three pairs of MOT beams, the emission laser at 405 nm and the vacuum chamber. The figure shows a low power diode laser at 405 nm focused onto a strontium oxide sample in solid form. As a result, Sr atoms are emitted and captured in a 3D-MOT. The MOT beams are shown in blue. The MOT fluorescence and a separate probe beam at 461 nm (not shown here) are used as the two detection methods for the Sr vapours. **(b)** Typical photographs of a ^{88}Sr (top) and ^{87}Sr (bottom) MOT, consisting of $\approx 4 \times 10^6$ atoms and $\approx 1 \times 10^6$ atoms, respectively. **(c)** Loading of the ^{88}Sr MOT. **(d)** Decay of the ^{88}Sr MOT. **(e)** Measured delay between switching off the emission laser and Sr vapour emission. After switching off the emission laser, an increase in the probe beam transmission is detected. In all panels, filled circles represent data while solid lines represent exponential fits to the data. A loading and decay time of $\approx$200 ms and $\approx$500 ms, respectively, are measured.

In order to demonstrate the applicability of our source to a cold atom experiment,

we trap the emitted Sr atoms in a MOT. While the data in the remainder of this

paper is based on measurements using the ^{88}Sr isotope, we are also able to load a

MOT using other Sr isotopes, in particular including ^{87}Sr, which is most commonly

used in Sr optical lattice clocks (Figure 6.5b).

Figure 6.5c shows a typical loading curve leading to $\sim 3 \times 10^6$ trapped ^{88}Sr atoms
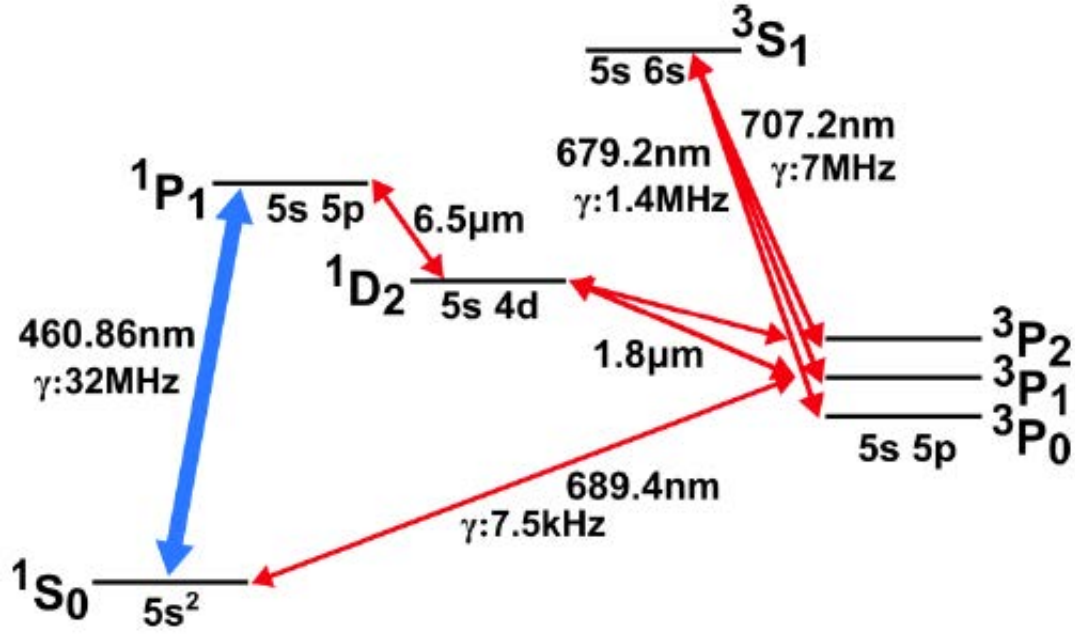
Figure 6.6: **Energy level diagram of Sr.** We show only the energy levels relevant to MOT operation. γ refers to the transition linewidth, and $^1S_0 - {^1P_1}$ is the main cooling transition. A small fraction of atoms can be lost to ^3P_j states via the $^1D_2$ state(see text).

(Figure 6.5b) without much optimisation. At the resulting density of 4×10^9 atoms per cm^3, collisions inside the MOT are insignificant [113], allowing a fit of the loading and decay curves in Figure 6.5c and 6.5d with exponential functions. The resulting 1/e loading and decay times are $\sim$200 ms and $\sim$500 ms, respectively. The difference is due to the rapid drop of background gas pressure when switching off the emission laser, leading to longer decay times. This is supported by the observation, that Sr fluorescence measurements show a fast drop to zero, when the emission laser is switched off (Figure 6.5e). The trapped atom number, and loading & decay rates can be optimised by adapting the geometry of the setup and changing laser power, focus and pulse duration. We have been able to trap $\sim 5 \times 10^5$ atoms for emission laser pulses of $\sim$200 ms, and one can anticipate achieving a higher number of trapped atoms for shorter duration of the emission laser by reducing the distance between the sample and the MOT centre.
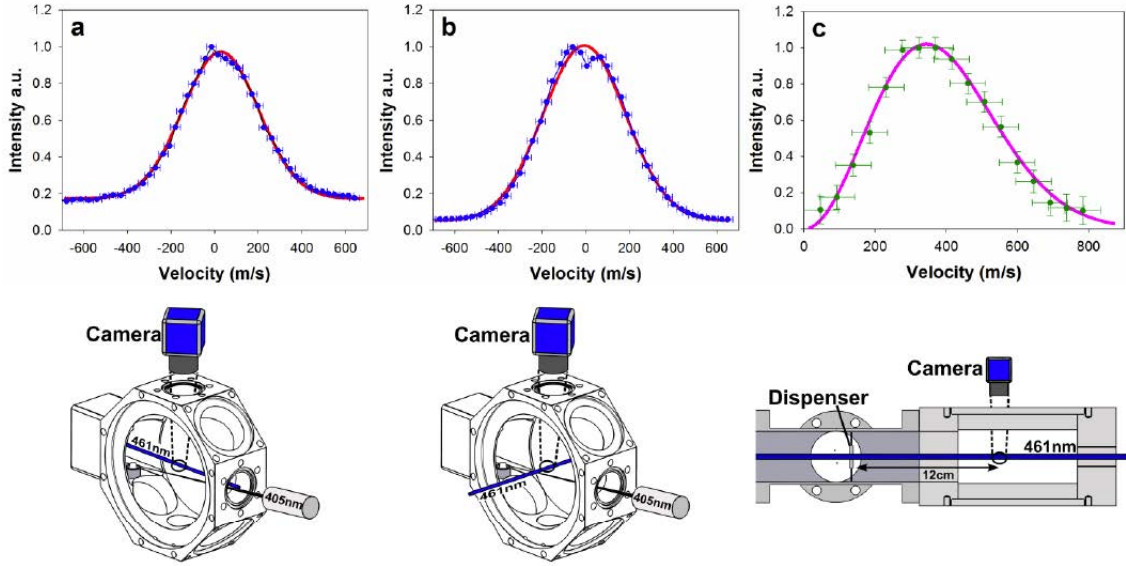
Figure 6.7: **Velocity distribution of the emitted atoms.** A probe beam at 461 nm was used to detect the fluorescence of the emitted atoms (y-axis). The velocity on the x-axis corresponds to the Doppler detuning of the probe beam. **(a)** Probe beam nearly antiparallel with the emission laser. **(b)** Retro-reflected probe beam orthogonal to the emission beam with a Lamb-Dip visible in the centre. **(a) & (b)** The filled circles represent the data while the solid lines represent Gaussian fits to the data. The data in both curves has been independently rescaled. **(c)** Thermal emission of Sr atoms.

Velocity distribution. In order to further understand the process, we have measured the velocity distribution of the emitted Sr atoms using Doppler sensitive spectroscopy (Figure 6.7). Independently rescaled fluorescence yields have been plotted as a function of velocity of the emitted atoms. Figure 6.7a shows the velocity distribution of atoms in relation to a probe beam counterpropagating with the emission laser. The nearly symmetric distribution can be fitted well with a Gaussian distribution centred on zero velocity, and a corresponding temperature of 319 K. This indicates that the atoms undergo several collisions and thermalize with the walls of the vacuum chamber. This is surprising, as the low room temperature vapour pressure of strontium would suggest that the atoms should stick to the wall. To confirm that atoms are able to reflect off the walls of the vacuum chamber, we performed the experiment illustrated in Figure 6.8. In this experiment, fluorescence was still

observed despite having no direct pathway for emitted Sr atoms to reach the path of the probe beam. This thermalization with the walls of the vacuum chamber is very useful for creating a thermal distribution accessible to laser trapping and cooling. This is consistent with evidence that the measured velocity distribution does not depend on emission laser power or wavelength.

A further consistency check is provided in Figure 6.7b, representing a measurement with a retroreflected probe beam perpendicular to the emission laser. This measurement shows a Lamb dip indicating the zero-velocity component and has the same width as the distribution in Figure 6.7a, indicating a fully thermalized vapour. Geometry, together with the source in the probe chamber, plays an important role in creating the observed thermalized background vapour. In contrast to the previous setup, a measurement of the emission velocity spectrum in a beam-like geometry in Figure 6.7c, using a commercially available dispenser (Alvatec Alvasource, Type S, Figure 2b in reference [12]), shows a very good fit with a Maxwell-Boltzmann distribution for 626 K.

6.2.4 Discussion

The presented method allows unprecedented control for generating atomic vapours for laser cooling and trapping applications. It does so by breaking chemical bonds in compounds, which have a negligible vapour pressure at ambient temperature. We find that the method is not restricted to strontium oxide, but also works with strontium hydroxide, strontium carbonate and bulk strontium. For all these samples we detect Sr vapours fluorescence in the vacuum chamber. The insensitivity of our measurements to the emission laser's wavelength, seem to suggest that the process could be thermal in nature. Finite element simulations suggest that this might be

107

possible if the powdery nature of the sample reduces the thermal conductivity by at least a factor of 100 as compared to bulk strontium oxide.

In any case, our method produces no significant heating and promises to overcome size, power and blackbody shift limitations of current Sr optical lattice systems. We anticipate this method will work with other species as well, furthering the ongoing efforts to realise quantum technologies that harness pristine quantum properties to deliver breakthroughs in a wide range of applications including quantum clock networks and deep space navigation, GNSS, VLBI, relativistic geodesy, financial markets and the exploration for minerals and oil [102–106, 114–116].

6.2.5 Methods

Sample preparation and science chamber. Sr vapours are generated from bulk strontium oxide near its surface. In order to generate strontium oxide, we use a solid piece of granular strontium (99% trace metals basis) which is exposed to air for 4 hours such that it can react with oxygen in the air to form strontium oxide. The prepared sample is mounted on a sample holder in the science chamber. The science chamber is a compact, titanium vacuum chamber with indium sealed viewports. The viewports are made of BK7 glass and are AR coated for all relevant wavelengths. We place the strontium oxide sample in solid form into the science chamber using a sample holder. The chamber is evacuated using a 20 L/s ion pump and a turbo-molecular pump. The chamber maintains an ultra high vacuum ($\sim 5 \times 10^{-10}$ mbar) environment.

Emission laser. We have mainly used a commercially available 405 nm diode laser (405 nm UV PHR-805T) with 120 mW as the maximum output power. The distance between the laser and the sample is 14 cm. We use a 4.5 mm aspheric lens to focus

the laser light 10 cm away from the sample. At the focal point, the $1/e^2$ laser beam diameter is 150 μm in the vertical and 200 μm in the horizontal. This allows for continuous emission of Sr. We have observed that at a tighter focus, one can emit large amounts of Sr. However, it lasts only for short durations, typically only a few seconds. At a shallower focus, on the other hand, we do not observe any emission. We use a separate laser beam at 461 nm in order to observe emission of Sr.

MOT and detection method. We use a six beam MOT, of which three beams are retro-reflected. Each beam is circularly polarised, 1 cm in diameter, 3 mW/cm^2 in intensity and approximately 56 MHz red detuned from the resonant transition $^1S_0$ – $^1P_1$ at 461 nm (Figure 6.6). Reflection and polarisation changes for the reflected beams are achieved, respectively, by focussing the beams onto mirrors and using achromatic quarter wave plates. To bring atoms in the long lived excited states $^3P_2$ and $^3P_0$ back to the ground state 1S0, we use standard repumping transitions $^3P_0$ – $^3S_1$ at 679 nm and $^3P_2$ – $^3S_1$ at 707 nm. For the MOT, we use a magnetic quadrupole field with a gradient of approximately 40 G/cm at the centre. The MOT centre is approximately 4 cm away from the sample. In order to detect the emitted Sr atoms, we use the broad $^1S_0$ – $^1P_1$ transition at 461 nm with 32 MHz linewidth. We use a probe beam of 1 mm diameter and 3 mW - 5 mW intensity. When Sr atoms are emitted, they interact with the probe beam, and the resulting fluorescence is detected by a CCD camera (pco.pixelfly usb, model PF-M-QE-PIV). We used a 1 ms exposure time for the fluorescence image of the MOT. In addition to the camera, we have used a photodiode for detecting the absorption of Sr atoms by a probe beam. During normal MOT operation, the probe beam is switched off. During loading, the emission laser is ON, while during the decay time, it is OFF.

Velocity distribution of emission. We use the fluorescence yield at $461nm$ to determine the velocity distribution present in the emission. From the Doppler effect,

we can estimate the velocity of atoms from the detuning of the probe laser using the following expression:

$$f_D = f_S \left(1 \pm \frac{v}{c}\right), \tag{6.1}$$

where f_D is the Doppler shifted frequency, f_S is the resonant frequency of the atomic transition, v is the velocity component of atoms along the probe beam direction and c is the velocity of light. In our Doppler spectroscopy, the velocity of atoms corresponds to the detuning of the probe laser from the resonance at $^1S_0 - {}^1P_1$. We scan the probe frequency by ± 2 GHz around the $^1S_0 - {}^1P_1$ transition at 461 nm, while monitoring the wavelength on a wavemeter (ADVANTEST Q8326, 10 MHz resolution). Our apparatus allows us to probe the emitted atoms from two orthogonal directions, one where the probe beam is almost antiparallel to the emission laser (Figure 6.5) and the other where the probe beam is orthogonal to the direction of the emission laser.
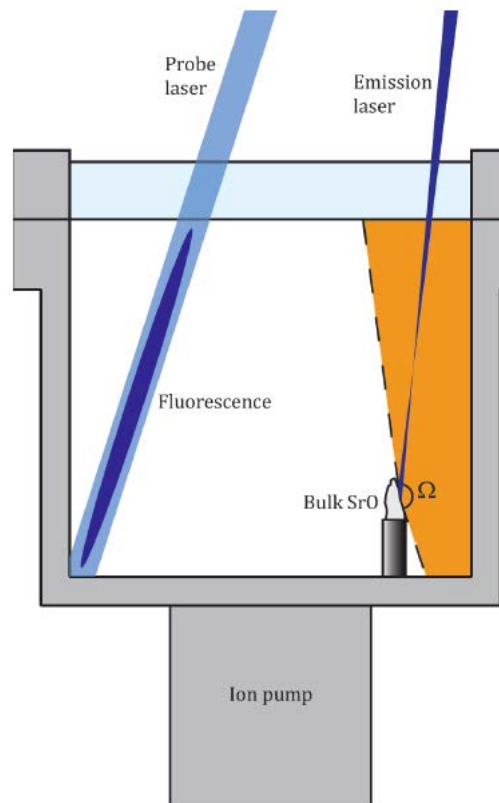
Figure 6.8: **Observation of fluorescence with no direct line of sight of sr vapour emission.** Experimental setup used to demonstrate that emitted Sr atoms collide with room temperature walls of a vacuum chamber without sticking. At the location where the emission laser hits the SrO sample, the Sr vapour will be emitted in a solid angle, Ω (the orange shaded region in the figure), that does not intersect any point with the beam path of the probe laser. When the emission laser was turned on, however, fluorescence could still be observed in the probe beam, indicating the presence of atomic vapour even after collisions with the chamber walls.

Chapter 7

Conclusion and Outlook

This thesis presents the ongoing development of a miniaturized strontium optical lattice clock. Great success has been achieved during the last four year. A 25 L blue MOT demonstrator has been built using a single-beam MOT configuration (Chapter 4), including a homemade 461 nm diode laser (Chapter 3) and essential electronics. In the demonstrator, a visible blue MOT has been realized with a power consumption below 50 W for the entire system. Using a high power homemade 461 nm laser (Chapter 5) and two repumping lasers, we were able to trap 5×10^6 ^{88}Sr atoms in a blue MOT with a temperature of 1-3 mK. In the absence of the 679 nm repumping laser, 1000 atoms have been loaded into a broadband red MOT.

For the first time, strontium oxide (Chapter 6) is used as an atom source with the outlook of eliminating the BBR shift on the clock transition frequency. With $\approx 4 \times 10^6$ ^{88}Sr and $\approx 1 \times 10^6$ ^{87}Sr atoms trapped in the blue MOT, strontium oxide provides an attractive solution for atom sources in strontium clocks.

After realizing a single frequency red MOT in the near future, the atoms will be loaded into an optical lattice. A high power (1.5 W), compact lattice laser at the magic wavelength of 813 nm has been designed in parallel within our laboratory. The 698 nm clock laser, which will be locked to a high finesse cavity, is being built by the National Physical Laboratory (NPL). Once the miniaturized clock is completed,

clock comparison measurements will be carried out at NPL, where the miniaturized clock can be compared to the frequency standards located at NPL.

By developing new technologies, we have scaled down the dimensions of the conventional strontium lattice clock system. During the course of the experiment, however, potential improvements to the system have been targeted.

Coating by strontium: In the single beam MOT chamber, the width of the experiment chamber is only 22.5 mm. Hot strontium emitted by the dispenser may stick to the room-temperature walls of the titanium chamber as well as the windows. After a long operation time, it remains an open question to determine if strontium may coat the prism mirrors, which may affect the polarization and power of the reflected cooling beams. At the point when the vacuum system was first brought to low pressure in November 2015, after one-year operation, the viewport which faces the dispenser directly was coated by strontium with observable coating. I did a transmission measurement on the viewports which covers the four prism mirrors. For brand-new viewports, the transmission of 461 nm laser is 96% for two viewports. The two viewports mounted on the vacuum setup had a transmission of 94%. An aging test using a 4-way cross with mirrors in the same configuration as the actual experiment chamber is planned.

Mirror fine adjustment: Since the mirrors are fixed inside the chamber, there is no freedom to adjust a single mirror to optimize the MOT. Due to manufacturing tolerances of the gaps where the mirrors are placed or the glueing process for the mirrors, the mounted mirrors may be displaced slightly from their designed geometry. One possible solution is to place the mirrors on an alignment plate before mounting them inside the vacuum chamber. The position of the mirrors could then be adjusted outside the vacuum environment.

Chamber pumping: With the getter-ion pump and borehole design of the cham-

ber, the pumping speed has been increased from earlier designs. However, the gauge in the ion pump controller may not accurately reflect the actual pressure in the MOT chamber since there is a relatively long separation distance and a getter pump between the chamber and the ion pump. A local measurement of the vacuum pressure is necessary, especially during clock evaluation. Using a getter pump with a DN16CF flange from SAES, we can move the pumping apparatus closer to the scientific chamber.

In addition to the issues discussed above, other aspects of the system may be optimized to improve the mobility of the apparatus, such as customized electronics and a computer control system. As the current system is an ongoing prototype towards a fully functional strontium lattice clock, more questions may be discovered and solved in future systems.

Traditionally, strontium has played an important role in cold atoms experiments because of its versatile level structure, with diode lasers available at accessible frequencies. For fundamental physics, strontium serves an important role in research on ultracold gases, cold molecules and Rydberg atoms. The most significant success in cold strontium experiments comes from the precision measurement of time. In laboratory environments, strontium optical lattice clocks have achieved both precision and accuracy at the 10^{-18} level. The result is two orders of magnitude better than the caesium fountain clocks which form the basis of the SI definition of second. As a result, strontium is one of the most promising candidates for the redefinition of the second.

The mobile strontium clock projects at the University of Birmingham have evolved through three experimental generations over the last 8 years. In the first transportable system, a 2D MOT for strontium was realized. The second generation, also known as the European Union Space Optical Clocks II project, now operates as

a fully functional strontium clock with a precision down to the 10^{-15} level. Although the third generation is still in progress, it has realized the first single beam MOT for strontium. These great developments pave the way for future mobile and space applications of strontium optical clocks.

Bibliography

[1] H. Katori, M. Takamoto, V. G. Pal'chikov, and V. D. Ovsiannikov. Ultrastable optical clock with neutral atoms in an engineered light shift trap. *Phys. Rev. Lett.*, 91(17):173005, 2003.

[2] R. Li, K. Gibble, and K. Szymaniec. Improved accuracy of the NPL-CsF2 primary frequency standard: evaluation of distributed cavity phase and microwave lensing frequency shifts. *Metrologia*, 48(5):283, 2011.

[3] T. Kurosu, Y. Fukuyama, Y. Koga, and K. Abe. Preliminary evaluation of the cs atomic fountain frequency standard at NMIJ/AIST. *IEEE Trans. Instrum. Meas.*, 53(2):466–471, 2004.

[4] B. J. Bloom, T. L. Nicholson, J. R. Williams, S. L. Campbell, M Bishof, X. Zhang, W. Zhang, S. L. Bromley, and J. Ye. An optical lattice clock with accuracy and stability at the 10^{-18} level. *Nature*, 506(7486):71–5, 2014.

[5] F. Riehle. Towards a redefinition of the second based on optical atomic clocks. *Comptes Rendus Phys.*, 16(5):506–515, 2015.

[6] N. Poli, R. E. Drullinger, G. Ferrari, and F. Sorrentino. Optical frequency standard with ultra-cold strontium atoms. In *Frequency and Time Forum*, pages 333–337, 2006.

[7] H. Katori. Frequency comparisons of sr, yb, and hg based optical lattice clocks and their applications. *Comptes Rendus Phys.*, 16(5):489–498, 2015.

[8] D. L. Mills. *Computer Network Time Synchronization: The Network Time Protocol on Earth and in Space, Second Edition.* CRC Press, 2010.

[9] C. W. Chou, D. B. Hume, T Rosenband, and D. J. Wineland. Optical clocks and relativity. *Science*, 329(5999):1630, 2010.

[10] S. Kolkowitz, I. Pikovski, N. Langellier, M. D. Lukin, R. L. Walsworth, and J. Ye. Gravitational wave detection with optical lattice atomic clocks. *Phys. Rev. D*, 94(12):124043, 2016.

[11] S. Origlia, S. Schiller, M. S. Pramod, L. Smith, Y. Singh, W. He, S. Viswam, D. Świerad, J. Hughes, K. Bongs, U. Sterr, C. Lisdat, S. Vogt, S. Bize, J. Lodewyck, R. Le Targat, D. Holleville, B. Venon, P. Gill, G. Barwood, I. R. Hill, Y. Ovchinnikov, A. Kulosa, W. Ertmer, E.-M. Rasel, J. Stuhler, and W. Kaenders. Development of a strontium optical lattice clock for the SOC mission on the iss. In *Proceedings of SPIE*, 2016.

[12] B. O. Kock. *Magneto-Optical Trapping of Strontium for use as a Mobile Frequency Reference.* PhD thesis, University of Birmingham, 2013.

[13] L. L. Smith. *A Transportable Strontium Optical Lattice Clock Towards Space.* PhD thesis, University of Birmingham, 2016.

[14] P. Zorabedian. Tunable external cavity semiconductor lasers. In *Tunable Laser Handbook*, pages 349–442. Academic Press, 1996.

[15] T. Middelmann, C. Lisdat, S. Falke, J. S. R. V. Winfred, F. Riehle, and U. Sterr. Tackling the blackbody shift in a strontium optical lattice clock. *IEEE Trans. Instrum. Meas.*, 60(7):2550–2557, 2011.

[16] X. Tian. Trapping four isotopes of strontium in a mot by using zeeman slowing. *Acta Opt. Sin.*, 30(3):898–902, 2010.

[17] X. Xu, T. H. Loftus, J. L. Hall, A. Gallagher, and J. Ye. Cooling and trapping of atomic strontium. *J. Opt. Soc. Am. B*, 20(5):968–976, 2003.

[18] M. Bennett, M. F. Schatz, H. Rockwood, and K. Wiesenfeld. Huygens's clocks. *Proc. R. Soc. Lond. A*, 458(2019):563–579, 2002.

[19] D. B Sullivan. Time and frequency measurement at nist: the first 100 years. In *Proceedings of the IEEE International Frequency Control Symposium and PDA Exhibition*, pages 4–17, 2001.

[20] M. Lombardi. The accuracy and stability of quartz watches. *Horological J.*, 150:57–59, 2008.

[21] H. Lyons. The atomic clock, an atomic standard of frequency and time. *N.B.S. Tech. News Bull.*, 33(17), 1949.

[22] L. Essen and J. V. L. Parry. An atomic standard of frequency and time interval: A cesium resonator. *Nature*, 176(176):280–282, 1955.

[23] SI brochure: The international system of units (SI). Technical report, BIPM, 2006.

[24] J. Dalibard and C. Cohentannoudji. Laser cooling below the doppler limit by polarization gradients: simple theoretical models. *J.Opt. Soc. Am. B*, 6(11):2023–2045, 1989.

[25] C. Salomon, J. Dalibard, W. D. Phillips, A. Clairon, and S. Guellati. Laser cooling of cesium atoms below 3 μK. *Europhys. Lett.*, 12(8):683–688, 1990.

[26] E. S. Ferre-Pikal and F. L. Walls. *Frequency Standards, Characterization.* John Wiley & Sons, Inc., 1999.

[27] D. M. Meekhof, S. R. Jefferts, M. Stepanovic, and T. E. Parker. Accuracy evaluation of a cesium fountain primary frequency standard at nist. *IEEE Trans. Instrum. Meas.*, 50(2):507–509, 2001.

[28] C. Cohen-Tannoudji. Laser cooling and trapping of neutral atoms: theory. *Phys. Rep.*, 219(3–6):153–164, 1992.

[29] Z. Zhang. Impact of rubidium clock aiding on gps augmented vehicular navigation. Master's thesis, University of Calgary, 1997.

[30] Daniel Kleppner, H. Mark Goldenberg, and Norman F. Ramsey. Theory of the hydrogen maser. *Phys. Rev.*, 126(2):603–615, 1962.

[31] B. H. Mcguyer. *Atomic physics with vapor-cell clocks.* PhD thesis, Princeton University, 2012.

[32] J. E. Bernard, L. Marmet, and A. A. Madej. A laser frequency lock referenced to a single trapped ion. *Opt. Commun.*, 150(1-6):170–174, 1998.

[33] J. Lodewyck, M. Zawada, L. Lorini, M. Gurov, and P. Lemonde. Observation and cancellation of a perturbing DC stark shift in strontium optical lattice clocks. *IEEE Trans. Ultrason., Ferroelect., Freq. Control*, 59(3):411–415, 2012.

[34] D. W. Allan. Statistics of atomic frequency standards. *Proc. IEEE*, 54(2):221–230, 1966.

[35] N. F. Ramsey. A molecular beam resonance method with separated oscillating fields. *Phys. Rev.*, 78(6):695–699, 1950.

[36] N. C. Wong. Optical-to-microwave frequency chain utilizing a two-laser-basedoptical parametric oscillator network. *Appl. Phys. B*, 61(2):143–149, 1995.

[37] J. Reichert, M. Niering, R. Holzwarth, M. Weitz, T. Udem, and T. Hänsch. Phase coherent vacuum-ultraviolet to radio frequency comparison with a mode-locked laser. *Phys. Rev. Lett.*, 84(15), 2000.

[38] T. Udem, J. Reichert, R. Holzwarth, and T. Hänsch. Absolute optical frequency measurement of the cesium D1 line with a mode-locked laser. *Phys. Rev. Lett.*, 82(18), 1999.

[39] D. J. Jones, S. A. Diddams, J. K. Ranka, A. Stentz, R. S. Windeler, J. L. Hall, and S. T. Cundiff. Carrier-envelope phase control of femtosecond mode-locked lasers and direct optical frequency synthesis. *Science*, 288(5466), 2000.

[40] S. A. Diddams, Th. Udem, J. C. Bergquist, E. A. Curtis, R. E. Drullinger, L. Hollberg, W. M. Itano, W. D. Lee, C. W. Oates, K. R. Vogel, et al. An optical clock based on a single trapped ^{199}Hg$^+$ ion. *Science*, 293(5531):825–828, 2001.

[41] A. D. Ludlow, M. M. Boyd, J. Ye, E. Peik, and P. O. Schmidt. Optical atomic clocks. *Rev. Mod. Phys.*, 87(2), 2014.

[42] A. D. Ludlow, X. Huang, M. Notcutt, T. Zanon-Willette, S. M. Foreman, M. M. Boyd, S. Blatt, and J. Ye. Compact, thermal-noise-limited optical cavity for diode laser stabilization at 1×10^{-15}. *Opt. Lett.*, 32(6), 2007.

[43] H. J. Metcalf and P. Van. Der Straten. Laser cooling and trapping of atoms. *J. Opt. Soc. Am. B*, 20(5):887–908, 2003.

[44] M. Takamoto, F. Hong, R. Higashi, and H. Katori. An optical lattice clock. *Nature*, 435(7040):321–324, 2005.

[45] T. Ido and H. Katori. Recoil-free spectroscopy of neutral sr atoms in the lame-dicke regime. *Phys. Rev. Lett.*, 91(5), 2003.

[46] R. Le. Targat, L. Lorini, Y Le. Coq, M. Zawada, J. Guena, M. Abgrall, M. Gurov, P. Rosenbusch, D. Rovera, B. Nagorny, et al. Experimental realization of an optical second with strontium lattice clocks. *Nat. Commun.*, 4:2109, 2013.

[47] B. D. Tapley, S. Bettadpur, J. C. Ries, Paul F. Thompson, and Michael M. Watkins. GRACE measurements of mass variability in the earth system. *Science*, 305(5683):503–505, 2004.

[48] N. Chiodo, N. Quintin, F. Stefani, F. Wiotte, E. Camisard, C. Chardonnet, G. Santarelli, A. Amyklein, P. Pottie, and O. Lopez. Cascaded optical fiber link using the internet network for remote clocks comparison. *Opt. Express*, 23(26):33927–33937, 2015.

[49] S. J. Schiller, A. Gorlitz, A. Nevsky, J. C. J. Koelemeij, A. Wicht, P. Gill, H. A. Klein, H. S. Margolis, G. Mileti, U. Sterr, et al. Optical clocks in space. *Nucl. Phys. B(Proc. Suppl.)*, 166:300–302, 2007.

[50] A. L. Migdall, J. V. Prodan, W. D. Phillips, T. H. Bergeman, and H. J. Metcalf. First observation of magnetically trapped neutral atoms. *Phys. Rev. Lett.*, 54(24):2596–2599, 1985.

[51] S. Chu, L. Hollberg, J. E. Bjorkholm, A. Cable, and A. Ashkin. Three-dimensional viscous confinement and cooling of atoms by resonance radiation pressure. *Phys. Rev. Lett.*, 55(1):48–51, 1985.

[52] A. Aspect, J. Dalibard, A. Heidmann, C. Salomon, and C. Cohen-Tannoudji. Cooling atoms with stimulated emission. *Phys. Rev. Lett.*, 57(14):1688–1691, 1986.

[53] D. J. Wineland, J. Dalibard, and C. Cohen-Tannoudji. Sisyphus cooling of a bound atom. *J. Opt. Soc. Am. B*, 9(1):32–42, 1992.

[54] K. Dieckmann, R. J. C. Spreeuw, M. Weidemüller, and J. T. M. Walraven. Two-dimensional magneto-optical trap as a source of slow atoms. *Phys. Rev. A*, 58(5):3891–3895, 1998.

[55] T. Yang, K. Pandey, M. S. Pramod, F. Leroux, C. C. Kwong, E. Hajiyev, Z. Y. Chia, B. Fang, and D. Wilkowski. A high flux source of cold strontium atoms. *Eur. Phys. J. D*, 69(10):226, 2015.

[56] W. D. Phillips and H. Metcalf. Laser deceleration of an atomic beam. *Phys. Rev. Lett.*, 48(9):596–599, 1982.

[57] Yuri B. O. A zeeman slower based on magnetic dipoles. *Opt. Commun.*, 276(2):261–267, 2007.

[58] J. E. Sansonetti and G. Nave. Wavelengths, transition probabilities, and energy levels for the spectrum of neutral strontium (SrI). *J. Phys. Chem. Ref. Data*, 39(3):033103, 2010.

[59] T. Hong, C. Cramer, W. Nagourney, and E. N. Fortson. Optical clocks based on ultranarrow three-photon resonances in alkaline earth atoms. *Phys. Rev. Lett.*, 94(5):050801, 2005.

[60] R. Santra, E. Arimondo, T. Ido, C. H. Greene, and J. Ye. High-accuracy optical clock via three-level coherence in neutral bosonic ^{88}Sr. *Phys. Rev. Lett.*, 94(17):173002, 2005.

[61] N. Poli, M. G. Tarallo, M. Schioppo, D. Sutyrin, N. Beverini, C. W. Oates, and G. M. Tino. Optical lattice clock on bosonic strontium atoms. In *CLEO/Europe - EQEC 2009 - European Conference on Lasers and Electro-Optics and the European Quantum Electronics Conference*, page 1, 2009.

[62] T. Akatsuka, M. Takamoto, and H. Katori. Optical lattice clocks with non-interacting bosons and fermions. *Nat. Phys.*, 4(12), 2008.

[63] Ch. Lisdat, J. S. R. Vellore Winfred, T. Middelmann, F. Riehle, and U. Sterr. Collisional losses, decoherence, and frequency shifts in optical lattice clocks with bosons. *Phys. Rev. Lett.*, 103(9):090801, 2009.

[64] A. P. Kulosa, D. Fim, K. H. Zipfel, S. Rühmann, S. Sauer, N. Jha, K. Gibble, W. Ertmer, E. M. Rasel, M. S. Safronova, U. I. Safronova, and S. G. Porsev. Towards a mg lattice clock: Observation of the $^{1}S_0-^{3}P_0$ transition and determination of the magic wavelength. *Phys. Rev. Lett.*, 115(24):240801, 2015.

[65] C.W. Oates, F. Bondu, R.W. Fox, and L. Hollberg. A diode-laser optical frequency standard based on laser-cooled ca atoms: Sub-kilohertz spectroscopy by optical shelving detection. *Eur. Phys. J. D*, 7(3):449–460, 1999.

[66] T. Kohno, M. Yasuda, K. Hosaka, H. Inaba, Y. Nakajima, and F. L. Hong. One-dimensional optical lattice clock with a fermionic ^{171}Yb isotope. *Appl. Phys. Express*, 2(7):072501, 2009.

[67] N. D. Lemke, A. D. Ludlow, Z. W. Barber, T. M. Fortier, S. A. Diddams, Y. Jiang, S. R. Jefferts, T. P. Heavner, T. E. Parker, and C. W. Oates. Spin-1/2 optical lattice clock. *Phys. Rev. Lett.*, 103(6), 2009.

[68] J. J. McFerran, L. Yi, S. Mejri, S. Di Manno, W. Zhang, J. Guéna, Y. Le Coq, and S. Bize. Erratum: Neutral atom frequency reference in the deep ultraviolet with fractional uncertainty = 5.7×10^{-15} [Phys. Rev. Lett. 108, 183004 (2012)]. *Phys. Rev. Lett.*, 115(21):219901, 2015.

[69] K. Yamanaka, N. Ohmae, I. Ushijima, M. Takamoto, and H. Katori. Frequency ratio of ^{199}Hg and ^{87}Sr optical lattice clocks beyond the SI limit. *Phys. Rev. Lett.*, 114(23):230801, 2015.

[70] A. D. Ludlow. *The Strontium Optical Lattice Clock: Optical Spectroscopy with Sub-Hertz Accuracy*. PhD thesis, University of Colorado, 2008.

[71] P. G. Mickelson, Y. N. Martinez de Escobar, P. Anzel, B. J. DeSalvo, S. B. Nagel, A. J. Traverso, M. Yan, and T. C. Killian. Repumping and spectroscopy of laser-cooled sr atoms using the $(5s5p)^3P_2-(5s4d)^3D_2$ transition. *J. Phys. B*, 42(23):235001, 2009.

[72] S. Stellmer, M. K. Tey, B. Huang, R. Grimm, and F. Schreck. Bose-einstein condensation of strontium. *Phys. Rev. Lett.*, 103(20):200401, 2009.

[73] N. Poli, M. Schioppo, S. Vogt, St. Falke, U. Sterr, Ch. Lisdat, and G. M. Tino. A transportable strontium optical lattice clock. *Appl. Phys. B*, 117(4):1107–1116, 2014.

[74] F. J. Kontur, I. Dajani, Y. L. Lu, and R. J. Knize. Frequency-doubling of a CW fiber laser using PPKTP, PPMgSLT, and PPMgLN. *Opt. Express*, 15(20):12882–12889, 2007.

[75] M. M. Boyd. *High Precision Spectroscopy of Strontium in an Optical Lattice: Towards a New Standard for Frequency and Time.* PhD thesis, University of Colorado, 2007.

[76] S. Yu and A. M. Weiner. Phase-matching temperature shifts in blue generation by frequency doubling of femtosecond pulses in KNbO3. *J. Opt. Soc. Am. B*, 16(8):1300–1304, 1999.

[77] T. van Zoest, N. Gaaloul, Y. Singh, H. Ahlers, W. Herr, S. T. Seidel, W. Ertmer, E. Rasel, M. Eckart, E. Kajari, S. Arnold, G. Nandi, W. P. Schleich, R. Walser, A. Vogel, K. Sengstock, K. Bongs, W. Lewoczko-Adamczyk, M. Schiemangk, T. Schuldt, A. Peters, T. Könemann, H. Müntinga, C. Lämmerzahl, H. Dittus, T. Steinmetz, T. W. Hänsch, and J. Reichel. Bose-einstein condensation in microgravity. *Science*, 328(5985):1540–1543, 2010.

[78] I. R. Hill, Y. B. Ovchinnikov, E. M. Bridge, E. A. Curtis, and P. Gill. Zeeman flowers for strontium based on permanent magnets. *J. Phys. B*, 47, 2014.

[79] K. Bongs, Y. Singh, L. Smith, W. He, O. Kock, D. Świerad, J. Hughes, S. Schiller, S. Alighanbari, S. Origlia, S. Vogt, U. Sterr, C. Lisdat, R. Le Targat, J. Lodewyck, D. Holleville, B. Venon, S. Bize, G. P. Barwood, P. Gill, I. R. Hill, Y. B. Ovchinnikov, N. Poli, G. M. Tino, J. Stuhler, and W. Kaenders. Development of a strontium optical lattice clock for the SOC mission on the iss. *Comptes Rendus Phys.*, 16(5):553–564, 2015.

[80] D. J. McCarron, S. A. King, and S. L. Cornish. Modulation transfer spectroscopy in atomic rubidium. *Meas. Sci. Technol.*, 19(10), 2008.

[81] M. H. Anderson, J. R. Ensher, M. R. Matthews, C. E. Wieman, and E. A. Cornell. Observation of bose-einstein condensation in a dilute atomic vapor. *Science*, 269(5221):198–201, 1995.

[82] W. Ketterle, K. B. Davis, M. A. Joffe, A. Martin, and D. E. Pritchard. High densities of cold atoms in a dark spontaneous-force optical trap. *Phys. Rev. Lett.*, 70(15):2253–2256, 1993.

[83] K. E. Gibble, S. Kasapi, and S. Chu. Improved magneto-optic trapping in a vapor cell. *Opt. Lett.*, 17(7):526–528, 1992.

[84] K. I. Lee, J. A. Kim, H. R. Noh, and W. Jhe. Single-beam atom trap in a pyramidal and conical hollow mirror. *Opt. Lett.*, 21(15):1177–1179, 1996.

[85] C. C. Nshii, M. Vangeleyn, J. P. Cotter, P. F. Griffin, E. A. Hinds, C. N. Ironside, P. See, A. G. Sinclair, E. Riis, and A. S. Arnold. A surface-patterned chip as a strong source of ultracold atoms for quantum technologies. *Nat. Nanotechnol.*, 8(5):321–324, 2013.

[86] B. M. Xu, X. Chen, J. Wang, and M. S. Zhan. Realization of a single-beam mini magneto-optical trap: A candidate for compact CPT cold atom-clocks. *Opt. Commun.*, 281(23):5819–5823, 2008.

[87] J.J. Arlt, O. Maragó, S. Webster, S. Hopkins, and C.J. Foot. A pyramidal magneto-optical trap as a source of slow atoms. *Opt. Commun.*, 157(1-6):303–309, 1998.

[88] L. B. Loeb. *The Kinetic Theory of Gases.* Dover Publications, 2004.

[89] G. C. Bjorklund, M. D. Levenson, W. Lenth, and C. Ortiz. Frequency modulation (FM) spectroscopy. *Appl. Phys. B*, 32(3):145–152, 1983.

[90] http://www.csimn.com/CSI_pages/PIDforDummies.html. Pid for dummies.

[91] J. Millen. *A cold strontium Rydberg gas.* PhD thesis, Durham University, 2011.

[92] R. W. P. Drever, J. L. Hall, F. V. Kowalski, J. Hough, G. M. Ford, A. J. Munley, and H. Ward. Laser phase and frequency stabilization using an optical resonator. *Appl. Phys. B*, 31(2):97–105, 1983.

[93] H. J. Metcalf and P. van der Straten. *Laser Cooling and Trapping.* Springer, 1999.

[94] H. Hagman, P. Sjölund, S. J. H. Petra, M. Nylén, A. Kastberg, H. Ellmann, and J. Jersblad. Assessment of a time-of-flight detection technique for measuring small velocities of cold atoms. *J. Appl. Phys.*, 105(083109), 2009.

[95] D. Świerad. Thesis in preparation. Private communication, 2016.

[96] T. Middelmann, S. Falke, C. Lisdat, and U. Sterr. High accuracy correction of blackbody radiation shift in an optical lattice clock. *Phys. Rev. Lett.*, 109(26):263004, 2012.

[97] L. Torralbo-Campo, G. D. Bruce, G. Smirne, and D. Cassettari. Light-induced atomic desorption in a compact system for ultracold atoms. *Sci. Rep.*, 5:14729, 2015.

[98] N. Hinkley, J. A. Sherman, N. B. Phillips, M. Schioppo, N. D. Lemke, K. Beloy, M. Pizzocaro, C. W. Oates, and A. D. Ludlow. An atomic clock with 10^{-18} instability. *Science*, 341(6151):1215–1218, 2013.

[99] T. L. Nicholson, S. L. Campbell, R. B. Hutson, G. E. Marti, B. J. Bloom, R. L. McNally, W. Zhang, M. D. Barrett, M. S. Safronova, G. F. Strouse, W. L. Tew, and J. Ye. Systematic evaluation of an atomic clock at 2×10^{-18} total uncertainty. *Nat. Commun.*, 6:6896, 2015.

[100] S. G. Porsev and A. Derevianko. Multipolar theory of blackbody radiation shift of atomic energy levels and its implications for optical lattice clocks. *Phys. Rev. A*, 74(2):020502, 2006.

[101] S. R. Jefferts, T. P. Heavner, T. E. Parker, J. H. Shirley, E. A. Donley, N. Ashby, F. Levi, D. Calonico, and G. A. Costanzo. High-accuracy measurement of the blackbody radiation frequency shift of the ground-state hyperfine transition in ^{133}Cs. *Phys. Rev. Lett.*, 112(5):050801, 2014.

[102] S. Schiller, A. Görlitz, A. Nevsky, S. Alighanbari, S. Vasilyev, C. Abou-Jaoudeh, G. Mura, T. Franzen, U. Sterr, S. Falke, C. Lisdat, E. Rasel, A. Kulosa, S. Bize, J. Lodewyck, G. M. Tino, N. Poli, M. Schioppo, K. Bongs, Y. Singh, P. Gill, G. Barwood, Y. Ovchinnikov, J. Stuhler, W. Kaenders, C. Braxmaier, R. Holzwarth, A. Donati, S. Lecomte, D. Calonico, and F. Levi. The space optical clocks project: Development of high-performance transportable and breadboard optical clocks and advanced subsystems. In *2012 European Frequency and Time Forum*, pages 412–418, 2012.

[103] Ph. Laurent, M. Abgrall, Ch. Jentsch, P. Lemonde, G. Santarelli, A. Clairon, I. Maksimovic, S. Bize, Ch. Salomon, D. Blonde, J.F. Vega, O. Grosjean, F. Picard, M. Saccoccio, M. Chaubet, N. Ladiette, L. Guillet, I. Zenone, Ch. Delaroche, and Ch. Sirmain. Design of the cold atom PHARAO space clock and initial test results. *Appl. Phys. B*, 84(4):683–690, 2006.

[104] P. Delva and J. Lodewyck. Atomic clocks: new prospects in metrology and geodesy. *Preprint at http://arxiv.org/abs/1308.6766*, 2014.

[105] D. Kleppner. Time too good to be true. *Physics Today*, 59(10), 2006.

[106] P. Komar, E. M. Kessler, M. Bishof, L. Jiang, A. S. Sorensen, J. Ye, and M. D. Lukin. A quantum network of clocks. *Nat. Phys.*, 10(8):582–587, 2014.

[107] M. Meucci, E. Mariotti, P. Bicchi, C. Marinelli, and L. Moi. Light-induced atom desorption. *Europhys. Lett.*, 25(9):639, 1994.

[108] W. Hansel, P. Hommelhoff, T. W. Hansch, and J. Reichel. Bose-einstein condensation on a microelectronic chip. *Nature*, 413(6855):498–501, 2001.

[109] B. P. Anderson and M. A. Kasevich. Loading a vapor-cell magneto-optic trap using light-induced atom desorption. *Phys. Rev. A*, 63(2):023404, 2001.

[110] S. W. Du, M. B. Squires, Y. Imai, L. Czaia, R. A. Saravanan, V. Bright, J. Reichel, T. W. Hänsch, and D. Z. Anderson. Atom-chip bose-einstein condensation in a portable vacuum cell. *Phys. Rev. A*, 70(5):053606, 2004.

[111] S. Ghosh, A. R. Bhagwat, C. K. Renshaw, S. Goh, A. L. Gaeta, and B. J. Kirby. Low-light-level optical interactions with rubidium vapor in a photonic band-gap fiber. *Phys. Rev. Lett.*, 97(2):023603, 2006.

[112] C. Klempt, T. van Zoest, T. Henninger, O. Topic, E. Rasel, W. Ertmer, and J. Arlt. Ultraviolet light-induced atom desorption for large rubidium and potassium magneto-optical traps. *Phys. Rev. A*, 73(1):013410, 2006.

[113] T. P. Dinneen, K. R. Vogel, E. Arimondo, J. L. Hall, and A. Gallagher. Cold collisions of $Sr^* - Sr$ in a magneto-optical trap. *Phys. Rev. A*, 59(2):1216–1222, 1999.

[114] R. M. Godun, P. B. R. Nisbet-Jones, J. M. Jones, S. A. King, L. A. M. Johnson, H. S. Margolis, K. Szymaniec, S. N. Lea, K. Bongs, and P. Gill. Frequency ratio of two optical clock transitions in $^{171}Yb^+$ and constraints on the time variation of fundamental constants. *Phys. Rev. Lett.*, 113(21):210801, 2014.

[115] N. Huntemann, B. Lipphardt, Chr. Tamm, V. Gerginov, S. Weyers, and E. Peik. Improved limit on a temporal variation of m_p/m_e from comparisons of Yb^+ and Cs atomic clocks. *Phys. Rev. Lett.*, 113(21):210802, 2014.

[116] M. S. Safronova. Time trials for fundamental constants. *Physics*, 7(117), 2014.